UNIVERSITY OF CALIFORNIA,
IRVINE

Improving High Frequency Oscillations as a Biomarker for Epilepsy

DISSERTATION

submitted in partial satisfaction of the requirements
for the degree of

DOCTOR OF PHILOSOPHY

in Biomedical Engineering

by

Kavyakantha Remakanthakurup Sindhu

Dissertation Committee:
Associate Professor Beth Lopour, Chair
Professor Zoran Nenadic
Assistant Professor Megan Peters

2023

DEDICATION

To my parents, for giving me wings

TABLE OF CONTENTS

LIST OF FIGURES

LIST OF TABLES

ACKNOWLEDGEMENTS

I would like to express the deepest appreciation to my advisor Dr. Beth Lopour for her incredible mentorship, unwavering support, and constant motivation throughout my PhD, without which this work would not have been possible. I would also like to thank my committee members Dr. Zoran Nenadic and Dr. Megan Peters for their valuable suggestions and feedback.

I would also like to thank our clinical collaborator Dr. Daniel Shrey for his diligence in curating data for our lab, and for his valuable clinical expertise at different points in this work. A big thank you, also, to Dr. Hernando Ombao for providing his expertise in the statistical analyses done in this work. I would like to thank the current and former members of the Lopouratory for their support, encouragement, and friendship.

Chapter 2 of this dissertation is a reprint of the material as it appears in Remakanthakurup Sindhu et al. 2020, used with permission from John Wiley & Sons, Inc. Figure 1.1 is also sourced from the same publication. The co-authors listed in this publication are Dr. Richard Staba and Dr. Beth Lopour. Chapter 3 is a reprint of the material as it appears in Remakanthakurup Sindhu et al., used with permission from IOP Publishing Ltd. The co-authors listed in this publication are Dr. Duy Ngo, Dr. Hernando Ombao, Dr. Joffre Olaya, Dr. Daniel Shrey and Dr. Beth Lopour.

I have been fortunate to have had the unending support of family and friends over the past five years, across continents and through a global pandemic. I want to express my deepest gratitude for their love and loyalty, which fueled me throughout my PhD and beyond.

Lastly, I would like to thank the Science and Engineering Research Board of India (SERB) for awarding me the Overseas Doctoral fellowship, which funded a part of my PhD studies at UC Irvine.

VITA

KAVYAKANTHA REMAKANTHAKURUP SINDHU

Education

2023 Ph.D. in Biomedical Engineering
University of California, Irvine

2021 M.S. in Biomedical Engineering
University of California, Irvine

2018 B.Tech. & M.Tech. in Electrical Engineering
Indian Institute of Technology, Madras

Publications

1. **Remakanthakurup Sindhu, K.**, Ngo, D., Ombao, H., Olaya, J. E., Shrey, D. W., & Lopour, B. A. A novel method for dynamically altering the surface area of intracranial EEG electrodes. J Neural Eng. 2023
2. Milà, B. R., **Remakanthakurup Sindhu, K.**, Mytinger JR, Shrey DW, Lopour BA. EEG biomarkers for the diagnosis and treatment of infantile spasms. Frontiers in Neurology 2022
3. **Remakanthakurup Sindhu, K.**, Staba, R, Lopour, BA. Trends in the use of automated algorithms for the detection of high-frequency oscillations associated with human epilepsy. Epilepsia 2020

ABSTRACT OF THE DISSERTATION

Improving High Frequency Oscillations as a biomarker for Epilepsy

By

Kavyakantha Remakanthakurup Sindhu

Doctor of Philosophy in Biomedical Engineering

University of California, Irvine, 2023

Associate Professor Beth Lopour, Chair

Epilepsy is one of the most common neurological disorders, with over five million people being diagnosed every year. Roughly one third of patients with epilepsy have poorly controlled seizures, despite treatment with one or more medications. In such cases, surgical resection of the seizure-generating tissue is an alternative and effective treatment. Post-surgical seizure freedom depends on the accurate localization of the epileptogenic zone (EZ), but there are currently no clinically validated biomarkers of this region. High frequency oscillations (HFOs), which are oscillatory events in the EEG, have been shown to have potential as a prognostic biomarker of surgical outcome in patients with epilepsy. However, some confounding factors limit their efficacy at the individual patient level. For example, within a single subject, electrodes of different sizes are often used, but there is currently no way to account for this difference when measuring HFO properties. Another

barrier is the presence of physiological HFOs (events generated as a part of healthy brain function) which confound estimates of rate of occurrence of pathological HFOs. Therefore, we aimed to address these limitations.

First, we developed and validated a novel method to dynamically change the size of an electrode after implantation in the human brain and determined the impact of electrode size on intracranial EEG (iEEG) characteristics. We then used this method to compare morphological features of HFOs across three electrode sizes. We found that the rate and amplitude of HFOs decreased significantly as electrode size increased. These results suggest that HFO rates from electrodes of different surface areas cannot be compared directly when used as a tool for surgical planning. Second, we detected physiological HFOs in the scalp EEG of 15 healthy infants using a combination of automated and visual methods and characterized their features across different sleep stages and anatomical regions. We found that rapid eye movement (REM) stage of sleep exhibited the highest density of HFOs compared to other stages. The results of this study will serve as baseline values of physiological HFOs to improve the identification of pathological HFOs associated with epilepsy. Together, these methods contribute to the use of HFOs as an efficient clinical biomarker for achieving improved post-surgery freedom in patients with epilepsy.

CHAPTER 1

INTRODUCTION

1.1 Seizures and epilepsy

Epilepsy is one of the most common neurological disorders, affecting more than 65 million people worldwide (3). It is hallmarked by recurrent spontaneous *seizures*, defined as abnormal synchronized neuronal activity in the brain that causes transient clinical signs or symptoms (4). Epilepsy can have various causes and can affect different parts of the brain. In some patients, the cause may be a genetic mutation or inheriting a gene that is predisposed to developing epilepsy. Other potential causes include brain injuries, stroke, structural abnormalities like brain tumors, infections such as meningitis or encephalitis, developmental disorders, and certain metabolic or neurodegenerative conditions (5). Epileptic seizures manifest in diverse ways, depending on the part of the brain affected and the intensity of the abnormal electrical activity. Common symptoms include sudden and involuntary movements, altered consciousness or awareness, sensory disturbances, muscle rigidity, and loss of control over bodily functions (4). Uncontrolled seizures can cause many adverse effects on the quality of life of patients, including shortened lifespan,

increased risk of excessive bodily injury, neuropsychological and psychiatric impairment, and social disability (6).

Seizures are divided into three categories based on onset location: generalized, focal, and unknown onset (7). Focal seizures are the most common type of seizures and are localized to a specific region in one side of the brain at onset. In generalized seizures, both hemispheres are activated at onset, as evidenced by both the patient's behavior and the electrical activity in their brain, as measured by electroencephalography (EEG) (7). Seizures are classified as unknown onset when there is not enough information to ascertain the location of seizure onset, but maybe classified as focal or generalized when more information becomes available (7). Focal seizures are further classified into aware or impaired awareness seizures, based on the level of awareness during seizure. Sometimes, seizures can begin as a focal seizure and spread to more regions, thereby becoming generalized. The type of seizure plays a large role in determining the symptoms, intensity, and treatment methods in a patient with epilepsy.

1.2 Diagnosis and Treatment

Accurate diagnosis of the specific type of seizure and epilepsy syndrome is an important first step in the treatment of epilepsy. This is done through the clinical evaluation of symptoms, physical and neurological exams, and assessment of medical

history, followed by brain imaging via modalities such as EEG, magnetic resonance imaging (MRI), and computed tomography (CT) (8).

Once the diagnosis is complete, the course of treatment is determined by various factors such as semiology, brain imaging results, subject age, family history etc. (9). The first step in the treatment of most epilepsies is antiseizure medication and diet. Antiseizure medication (ASM) is a preventative form of treatment, and it usually works by decreasing excitability or increasing inhibition of neurons. For example, this can be achieved by modulating voltage-dependent sodium or calcium channels or enhancing $GABA_A$ (γ-aminobutyric acid, type A) activity (10).

While a majority of patients show significant reduction in seizures through these steps, about 30% of patients do not respond well (9). Such patients with pharmacoresistant epilepsies may be evaluated for surgical resection or disconnection. If surgery is deemed to be not possible or is ineffective in a patient, other methods such as vagal nerve stimulation, responsive neural stimulation, ketogenic diet and/or combinations of anti-epileptic drugs are used to control seizures. These modes of treatment often aim at reducing the intensity and frequency of seizures, as they do not generally bring about complete seizure freedom.

1.2.1 Surgical Intervention

Surgical treatment has been shown to be effective and safe for patients with drug resistant focal epilepsy, where seizures that are localized to a brain location that can be safely removed with minimal risk of physiological or cognitive dysfunction (11). For example, about two thirds of patients with temporal lobe epilepsy, which is the most common cause of medically intractable seizures, experience seizure freedom after surgery (12, 13). On the other hand, if seizures are localized to the eloquent cortex, governing the patient's motor or language function, surgical treatment is not viable.

For patients considering surgery, a pre-surgical evaluation is done to localize the seizures. The first step involves a baseline neurological examination using non-invasive imaging modalities, like scalp EEG and MRI (14). In some patients, these tests may not yield converging information about seizure localization and the risk of postoperative deficits. In such cases, more advanced modalities like positron emission tomography (PET), single photon emission computed tomography (SPECT) or invasive methods like intracranial EEG (please see section 1.2.2) may be deemed necessary. A patient is considered a good candidate for surgical treatment if the seizure focus is accurately localized using these presurgical evaluation methods.

1.2.2 Intracranial EEG in the assessment of epilepsy surgery

Intracranial EEG (iEEG) is a commonly used tool for surgical planning in patients with medically refractory epilepsy when non-invasive imaging results are inadequate to guide surgical resection. iEEG data is recorded using electrodes directly implanted into brain tissue including subdural grid and strip electrodes, and penetrating depth electrodes. The nature of iEEG electrodes chosen for a particular patient, including type, number, size, material, inter-electrode spacing etc., is based on clinical considerations such as the findings of previous non-invasive imaging studies and epilepsy etiology (15). These factors also determine the selection of electrode sites and duration for which they remain implanted (16).

Compared to non-invasive imaging modalities like scalp EEG, iEEG provides advantages in terms of both spatial and temporal resolutions. It is possible to record a wide range of spatial scales using iEEG electrodes, ranging from single-neuron activity to neural activity in the millimeter range. High sampling rate iEEG acquisition can reliably record electrophysiological phenomena in the sub millisecond range (16). iEEG electrodes can detect potentials from deep brain structures like the amygdala, hippocampus and cingulate cortex (17). iEEG also offers a better signal-to-noise ratio (SNR) and is less prone to artifacts induced by electrode movement, muscle activity and volume conduction (16-18). Because of these, iEEG can provide invaluable information for presurgical

evaluation including accurate localization or lateralization of seizure patterns and cortical mapping of eloquent areas.

Due to their invasive nature, iEEG electrodes pose significant risk of complications including epidural hematoma, subdural and intracerebral hemorrhages, cerebral infarction, infections, transient neurological deficit, status epilepticus, cerebral oedema and CSF leak (19). While a majority of these are transitory, permanent and serious complications can arise in about one percent of the subjects (17, 19). Other major limitations of iEEG include the sparse and incomplete sampling of the brain, and the lack of standardization in electrode insertion and placement (20).

1.3 Clinical Biomarkers

The outcome of epilepsy surgery is largely dependent on the accurate localization of the patient's unique epileptogenic zone (EZ), defined as the smallest region of brain tissue that is to be removed for complete seizure freedom in the patient (21). However, the EZ is a theoretical entity, and there are currently no imaging techniques that can delineate it directly. Therefore, the identification of the region to be resected is a challenging task. Because the abnormal electrical activity that occurs in the brain during seizures can be directly measured using EEG and iEEG, considerable research has been done to identify electrophysiological biomarkers of surgical outcome. Two of the most

frequently used biomarkers in clinical practice are the seizure onset zone (SOZ) and interictal epileptiform discharges (IEDs).

1.3.1 Seizure Onset Zone

The SOZ is defined as the region or regions of the brain in which the seizure activity starts. It is most commonly delineated using scalp or iEEG recordings but can also be determined using techniques like SPECT and magnetoencephalography (MEG) (21). The removal of the SOZ is the current gold standard in epilepsy surgery since it is believed to be a good approximation for the EZ. However, there are several drawbacks associated with using the SOZ as a proxy for the EZ. Firstly, the extent of the EZ often extends beyond the SOZ. In such cases, removal of the SOZ will not result in complete seizure freedom (21). Second, scalp EEG electrodes lack the spatial resolution to precisely localize the SOZ for surgery and can potentially identify erroneous areas or much larger regions than necessary. iEEG is one way to address this problem, as it provides the necessary spatial sensitivity; however, the invasive iEEG electrodes are placed only in a small portion of the brain and may not sample the full extent of the SOZ or may miss it entirely. Third, there is no precise definition of "seizure onset" and it is subjectively determined. Seizure onset varies widely across the many etiologies and brain regions in which it can occur and can often be overlooked. Additionally, there is also no standard time window marking the duration of seizure onset, making differentiation of regions of onset and later

spread difficult. Lastly, determining the SOZ requires that at least a few stereotypical seizures are captured directly using EEG and sometimes iEEG as well. Therefore, in some cases, this necessitates several weeks of EEG monitoring, although there are instances where seizures remain undetected despite the extended duration.

1.3.2 Interictal epileptiform discharges

IEDs are brief paroxysmal events less than 250ms long that can be observed using both scalp EEG and iEEG in periods between seizures (22). The category of IEDs includes various waveforms like spikes, polyspikes, and sharp waves. It has been shown that IEDs have diagnostic value in epilepsy (23), with EEGs of patients with epilepsy being 90% more likely to show IEDs (24). Some features of these events, like rates of occurrence and high-frequency activity preceding spikes, have been shown to be predictive of surgical outcome (25). However, there are two major limitations associated with the use of IEDs as tools for surgical planning in epilepsy. First, they have low specificity because patients can be seizure free even if regions exhibiting IEDs are not resected (26). Second, they do not consistently correspond to seizure activity; for example, they show no reduction after treatment with anti-seizure medication (23).

Due to the limitations of the currently available biomarkers mentioned above, accurately predicting the post-surgical outcome in patients with medically intractable epilepsy is still a challenge. Indeed, only about 60% of patients that undergo epilepsy

surgery achieve long term post-surgical seizure freedom. Hence, there is a need for more accurate electrophysiological biomarkers for localizing seizures and aiding surgical planning by predicting outcome based on the planned resection area. High frequency oscillations are a new biomarker that has been shown to have promise in predicting surgical outcome while overcoming some of the limitations of current clinical biomarkers (27).

1.4 High Frequency Oscillations

1.4.1 High Frequency Oscillations as a biomarker for epilepsy

The term high frequency oscillations (HFOs) refers to brief rhythmic electrical activity in the brain that occurs at frequencies much higher than the standard clinical range (1-30Hz). More specifically, they are transient electrographic events consisting of multiple sinusoid-like waves in the 80 to 500Hz frequency range that clearly stand out from the background (Figure 1.1)(28). They are classified into types based on frequency: ripples (80-250Hz) and fast-ripples (250-500Hz). More recently, very high frequency oscillations in the 800-2000Hz range have also been shown to have potential for seizure localization (29).

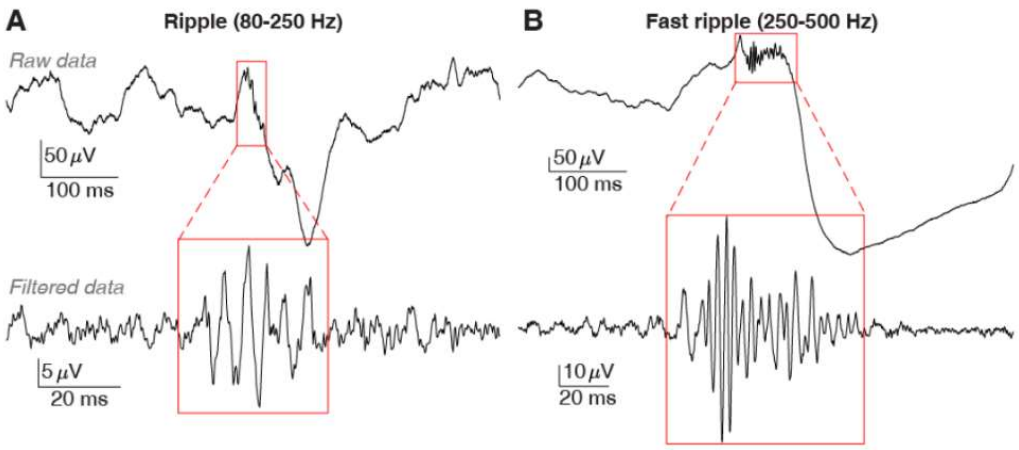

Figure 1.1: HFO examples (red boxes). (A) Ripples consist of oscillations in the 80-250 Hz frequency band, and (B) fast ripples are oscillations in the 250-500 Hz frequency band. The events are barely visible in the broadband data (top), but they clearly stand out from the background when a band-specific filter is applied (bottom).

Some of the first HFOs to be studied were seen in the hippocampus of rodents with experimentally-induced epilepsy and in humans with temporal lobe epilepsy (30). They have been subsequently observed throughout the human brain, including the neocortex and subcortical structures like the thalamus and basal ganglia, primarily using iEEG electrodes. A few recent studies have also observed HFOs in human scalp EEG (31-33). Although the exact mechanisms are unknown, several neuronal processes have been investigated as factors contributing to the generation of HFOs, including action potentials during weakly-synchronized firing of pyramidal cells (34) or inhibitory synaptic potentials occurring rhythmically in the perisomatic region of pyramidal cells (35).

The rates of occurrence of interictal HFOs, their amplitude, and other features have been shown to be higher in the SOZ than outside it (36-42). Studies have also shown

that removal of HFO-generating brain regions is positively correlated with good surgical outcome (43-45). Thus, these events are a potentially useful tool for surgical planning. Please see Chapter 2 for details on HFO detection and applications in seizure localization. HFOs provide several advantages over other clinical biomarkers including (i) they are highly localized and hence can provide better spatial resolution for localizing seizures than larger events such as IEDs (ii) they can be recorded interictally (in between seizures), and studies have shown that localization using HFOs can be done with as little as 10 minutes of iEEG data.

In addition to their prognostic value in epilepsy surgeries, HFOs also have potential applications in assessment of severity of epilepsy and monitoring effects of antiseizure medications (28). Additionally, they have opened new avenues for the study of mechanisms of seizure generation and epileptogenesis (46).

1.4.2 Limitations

Although HFOs have shown great promise as a biomarker, some limitations preclude their adoption into clinical practice. First, some recent studies have shown that HFOs do not work equally well in all subjects (47, 48). Of particular interest is Jacobs et. al. 2018, a large multicenter study that showed that HFOs were predictive of surgical outcome at a group level, but they were accurate for individual subjects in only about 50% of the cases (47).

A major limitation in the use of HFOs is the lack of a precise physiological definition (28). Current studies of HFOs detect events based on empirically derived features, which introduces bias. Also, different studies use different thresholds for these features leading to a lack of standardization across HFO studies. Another limitation is the wide range of spatial scales at which HFOs are recorded, ranging from .003mm^2 to 20mm^2 (49, 50). It is unknown if the HFOs recorded at these different spatial scales represent the same phenomenon and have equivalent clinical relevance. Moreover, there has been conflicting evidence regarding the impact of electrode size on HFO characteristics(37, 51). This, coupled with the huge variability in electrode sizes used for HFO recordings make accurate interpretation of measurements difficult.

A third limitation is the presence of physiological HFOs in EEG recordings; these are HFOs generated as a part of healthy brain function and not caused by underlying disease. Physiological HFOs have been shown to be associated with cognitive processes during memory consolidation, visual processing, and motor activity (52). These events overlap significantly in their morphological features with pathological HFOs caused by epileptic activity, and therefore cannot be reliably distinguished from one another (39, 53). This introduces a confounding factor in seizure localization using HFOs since it requires the measurement and analysis of exclusively pathological events.

1.5 Scope of this work

Through this work, we aimed to improve HFOs as a biomarker for epilepsy by addressing some of the limitations discussed in Section 1.4.2. We focus on two specific gaps in research: (i) the variability in HFO characteristics caused by electrode size and (ii) the characterization of physiological HFOs in healthy subjects.

In the second chapter we review literature on algorithms for the automatic detection of HFOs and summarize the standard steps for data pre-processing, as well as post-processing strategies for rejection of false positive detections (1). We also review evidence for the relationship between automatically detected HFOs and surgical outcome. Based on the literature, we provide practical recommendations and propose standards for the selection, implementation, and validation of automated HFO-detection algorithms.

In chapter 3, we introduce a novel method to record from electrodes of different sizes in the exact same location by changing the size of iEEG electrodes after implantation in the human brain (2). We developed the method based on a circuit model of the electrode-brain interface and tested it using an *in-vitro* experiment. We then report the results of an *in-vivo* implementation in three human subjects with refractory epilepsy. We record iEEG data from three different electrode sizes and compare the amplitudes, power spectra, inter-channel correlations, and SNR of epileptic spikes. We found that iEEG

amplitude and power decreased as electrode size increased, while inter-channel correlation did not change significantly with electrode size. The SNR of epileptic spikes was generally highest in the smallest electrodes, but 39% of spikes had maximal SNR in the larger electrodes. This is the first study to compare these EEG features across different electrode sizes and it sets the groundwork for multi-scale analysis of neurological phenomena recorded from a single location in the brain.

In the fourth chapter, we use the method developed in chapter 3 to detect HFOs in eight human subjects using three different electrode sizes. In each patient, the site from which data are recorded remained consistent across the small, medium, and large electrodes. We calculate the average rate, amplitude, duration, and peak frequency of the detected HFOs and compare them across electrode sizes. We found that the rate and amplitude of HFOs decrease significantly as electrode size increases. These results suggest that HFO rates from electrodes of different surface areas cannot be compared directly when used as a tool for surgical planning. This has significant implications for individual patients implanted with electrodes of multiple sizes, as well as comparisons of HFO rates made across patients and studies.

In the final chapter, we characterize physiological HFOs in healthy infants using noninvasive scalp EEG. We detect 11718 HFOs in 185 hours of data, an order of magnitude more than previous studies. We use a combination of automated detection,

automated artifact rejection, and visual validation to robustly identify the HFOs. We then characterize the spatiotemporal characteristics of the HFOs according to sleep stage, anatomical location, and age of subject. We report that HFO densities had a non-uniform spatial distribution, with the highest values occurring in the frontal, temporal and pre-frontal regions. We also found that rapid eye movement (REM) stage of sleep exhibited the highest density of HFOs compared to other stages. The results of this study will serve as baseline values of physiological ripples to improve the identification of pathological ripples associated with epilepsy and also deepen our understanding of the relationship between ripple occurrence and cognitive processes in various stages of sleep.

Together, these methods contribute to the use of HFOs as an efficient clinical biomarker for achieving improved post-surgery freedom in patients with epilepsy. The method we developed for multiscale recording of iEEG data provides a critical understanding of the impact of electrode geometry on signal characteristics. Moreover, it can enable dynamic selection of optimal electrode sizes for detection of neurological events like seizures, HFOs, and interictal spikes in clinical settings, as well as recordings used by neural prostheses or brain computer interfaces.

CHAPTER 2

ALGORITHMS FOR AUTOMATIC DETECTION OF HIGH FREQUENCY OSCILLATIONS

2.1 Introduction

Epilepsy is one of the most common neurological disorders, affecting more than 65 million people worldwide (3). Roughly one third of patients with epilepsy have poorly controlled seizures despite optimal treatment with medication (54). In such cases, surgical resection of the epileptogenic zone (EZ) is an alternative and effective treatment (55, 56). Post-surgical seizure freedom depends on the accurate localization of the EZ, but there are currently no validated biomarkers of the EZ (57, 58). The present gold standard for epilepsy surgery is removal of the seizure onset zone (SOZ), defined as the brain area where seizure activity is first seen. However, the SOZ is difficult to localize and doesn't delineate the full extent of the EZ. Thus, in addition to the SOZ, other electrophysiological as well as non-EEG biomarkers are needed to help localize the EZ.

High frequency oscillations (HFOs) have been studied extensively in the past two decades as a potential biomarker of the EZ (59). HFOs are transient electrographic events consisting of multiple sinusoid-like waves in the 80 to 500Hz frequency range that clearly stand out from the background (Figure 1) (28). To analyze HFOs, high sampling rate

data must be collected, which requires the use of a specialized amplifier (60). HFOs can be measured with both intracranial EEG and scalp EEG (28), although frequent artifacts (signals of non-neural origin) and the low power associated with high frequency activity, especially in scalp recordings, make accurate detection a challenge (60). After the data are recorded, interictal HFOs are detected in the signal from each channel using visual or automatic detection, and the rates (number per minute per channel) are calculated. Numerous studies show that the HFO rate is higher inside than outside the SOZ (36-42), and there is good evidence that removal of brain regions exhibiting a high rate of HFOs correlates with good surgical outcome (43, 45, 61). These data suggest that regions containing channels with high HFO rates are potential surgical targets.

However, the precise cellular mechanism by which HFOs are generated remains unknown, which has prevented establishment of a consensus on the features (e.g., amplitude, duration, frequency, and number of cycles) used to describe an HFO. Therefore, current studies rely on an empirical definition derived from visual observation (62, 63). Different research groups choose different definitions, e.g., a criterion of three or more oscillations vs. four or more oscillations in each HFO. Moreover, physiological HFOs in the ripple band, such as those occurring in the hippocampus (52), have features that overlap with those of pathological HFOs (53, 64, 65). This makes both visual and automatic detection problematic.

For HFO detection, the earliest studies relied on visual methods, using one or more experienced reviewers (30, 66). However, this is a time-consuming process, especially when analyzing more than a few minutes of data. Also, the inter-reviewer reliability is often inadequate (67-69). This suggests the need for fast and accurate automatic detection algorithms. There are many published automatic detection algorithms, but almost no recommendations on when one algorithm should be chosen over the others and how to select parameters for implementation. Directly comparing different algorithms is non-trivial because it is rare for multiple algorithms to be applied to the same dataset, and the performance of each algorithm depends on the choice of parameters. Here we provide a comprehensive review of current automated algorithms. First, we compare and contrast the methods, then we identify trends in the use of automated detection in clinical studies for SOZ/EZ localization. Lastly, we suggest standards for the development and implementation of automated detectors.

2.2 Automated detection of HFOs

2.2.1 Data acquisition and preprocessing

Intracranial EEG (iEEG) data for clinical HFO research is commonly recorded using standard macroelectrode contacts on grid and strip electrocorticogram (ECoG) electrodes, depth electrodes, and stereotactic EEG (SEEG). These electrodes have surface

areas ranging from roughly 1 to 10mm^2 (70). The data are typically re-referenced offline to a bipolar montage, and visual review is used to reject channels containing significant artifacts (71, 72). For HFO analysis, the acquired iEEG data is bandpass filtered to restrict the range of frequencies, predominantly using finite impulse response filters with forward and reverse filtering to minimize phase distortion (73). Based on early results, research has primarily focused on two frequency bands: the ripple band (80-250Hz) and the fast ripple band (250-500Hz) (66). Whitening, or spectral equalization, can be done to compensate for the fact that EEG power decreases as frequency increases (69, 74, 75). Data for HFO analysis are normally acquired at 2000 Hz or more using specialized amplifiers. However, some studies have used standard clinical sampling rates to study oscillations in the gamma band, venturing away from the conventional definition of HFOs (69, 76).

HFOs occur with the highest probability during non-rapid eye movement (NREM) sleep (40), and muscle artifacts are less frequent during these periods; hence, NREM is most commonly used for detection of HFOs. In studies where scalp EEG is unavailable, NREM sleep is identified via increased power in low frequency bands (77, 78) or additional EOG and EMG electrodes (45, 47). However, some studies do not sleep stage because scalp EEG is not a standard procedure for long-term intracranial monitoring (79). HFOs

are typically detected in short epochs of data, ranging from 1 to 10 mins, but recent evidence suggests that longer epochs may be necessary (80).

Although HFOs have been identified in both ictal and interictal EEG, HFO studies predominantly use interictal data, taken a few hours before and after seizures. The use of interictal data negates the need to wait for rare and unpredictable seizures, and it reduces the amount of high sampling rate data that must be recorded and stored. Moreover, data from Zijlmans et al. suggested that HFOs occur in the same brain regions during ictal and interictal periods (81). Residual anesthesia and anti-seizure medications can suppress HFO activity (27, 82) so data is typically collected on or after the second night of recording.

2.2.2 Automated algorithms for initial event detection

A critical step in the detection of HFOs is separating them from the background activity. For this initial detection step, existing algorithms use energy-based metrics (Table 1). Among the many energy measures that exist, the most commonly used are root-mean-square (RMS) amplitude (71, 72, 79, 83-86), power (87, 88), line length (37, 69, 87, 89), and Hilbert transform envelope (90, 91). Other methods include a median filter (92) and amplitude of the local peaks in the filtered data (78, 93). A multi-channel detection method based on RMS and line length was also proposed to account for simultaneous measurement of multiple adjacent electrodes and eliminate the need for

manual channel selection (94). Several of the energy-based metrics (RMS, power, line length, and median filter) are calculated for short windows of filtered data with or without overlap, which adds an additional parameter. The others (Hilbert envelope, amplitude of local peaks) can be calculated without windowing the data.

After calculating the energy, events that exceed a pre-determined threshold for a minimum duration are identified as potential HFOs. The threshold is typically a number of standard deviations above the mean value, or a non-parametric threshold based on the cumulative distribution function, e.g., events with an energy above the 99^{th} percentile. The threshold can be set for the entire duration of the data or for short epochs of data, which accounts for local modulations in the energy of the background activity. These detectors may further require a minimum number of oscillatory cycles for events to qualify as HFOs. Events that are separated by less than a minimum time period are often concatenated to form one single event. The parameters can be adjusted to change the sensitivity of the detector, but a highly sensitive detector may be preferred if it is paired with post-processing steps to reject false positives (see Section 2.3). While there are exceptions, the events detected by these methods will have significant overlap because the different energy metrics are highly correlated (Figure 1). Energy-based methods are easy to relate to visual detection and have a low barrier to implementation, but accurate performance is highly dependent on optimization of the detection parameters.

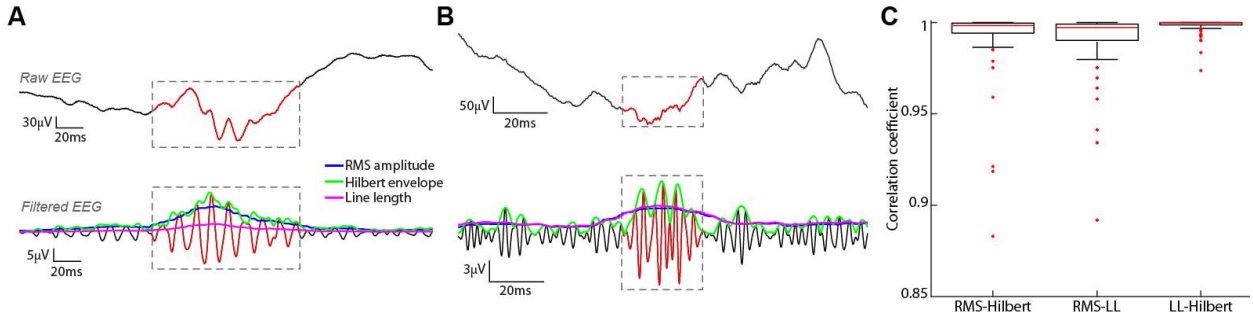

Figure 2.1: Energy measures used for HFO detection are highly correlated. Measurements of RMS amplitude (blue), Hilbert envelope (green), and line length (pink) are shown for (A) a representative ripple, recorded from the left anterior cingulate and (B) a representative fast ripple, recorded from the right anterior hippocampus. Depth electrode recordings are from an 18-year-old male. Line Length has been multiplied by a factor of five to aid visual comparison to the other measures. (C) The correlation between all three energy measures is high. Correlation coefficients were calculated between pairs of energy measures for 100 randomly selected data segments containing HFOs after bandpass filtering between 80-500 Hz.

2.2.3 Post processing and rejection of false positives

Filtering of a sharp transient in the EEG will produce a burst of high frequency activity, which may be falsely detected as an HFO (73). Signals of non-neural origin, such as muscle activity and harmonics of electrical line noise, can also cause false positive detections (95). For this reason, many algorithms include steps for rejection of false positives after the initial detection (Table 1). While this increases the specificity of the detector, it also introduces additional parameters that must be optimized. Visual rejection is commonly used, especially coupled with low sensitivity detectors. Automated methods

have also been developed, as visual marking is not feasible when the number of detected events is high. These include techniques based on the time domain signal, the time-frequency decomposition, and machine learning:

2.2.3.1 Time domain techniques

Detected events may be rejected if the duration exceeds a threshold (92), indicating possible contributions of muscle activity. Special methods for detecting fast DC-shifts in the raw data and artifacts in the common average (indicating that the event is too spatially widespread to be an HFO) have been proposed (79). Restricting the number of zero crossings in the raw data has also been used as a means of rejecting false HFOs (92).

2.2.3.2 Time-Frequency decomposition

Time-frequency (TF) analysis allows visualization of a signal's power spectrum as a function of time. In a TF plot, true HFOs are thought to be represented by an island of increased power at high frequencies, with the high power occurring within a distinct band (Figure 3A,B), while sharp, artifactual transients exhibit high power across all frequencies (Figure 3C)(73). Moreover, an HFO superimposed on a spike may have a power spectrum peaking at both low and high frequencies (Figure 3D)(73, 96). Application of a bandpass filter to the data, which is commonly the first step of HFO detection, is like taking a smaller horizontal slice of the TF plot. When this is done, all the examples in Figure 3 (including the artifact) will produce HFO-like events. Thus, examination of

the TF plot can be used to distinguish real HFOs from false positive detections, which is often not possible by looking at the bandpass filtered data. However, the TF decomposition is computationally intensive, so these methods are not used for initial detection. Rather, they are applied after an energy-based detector with high sensitivity.

Common methods to calculate the time-frequency decomposition include the Stockwell transform (97, 98), Morse wavelet (96), short-time Fourier Transform (88, 92), discrete wavelet transform (88), Gabor wavelet (99, 100), and Morlet wavelet (90, 101-106). TF analysis has been used for visual confirmation of automatically detected HFOs (96, 103, 104), and this process has also been successfully automated (88, 90-92, 98, 106). These automated methods commonly apply a threshold to the ratio between a predetermined high frequency power and low frequency power (88, 91). TF decomposition is also used for analysis of HFO features, which can shed light on their morphology (99-102).

Table 1.1: Automatic Detection Algorithms

Abbreviations – RMS: root-mean-square, T-F: time-frequency, T: Threshold, L: Window Length, D: Minimum duration, P: Minimum number of peaks, S: Minimum separation between distinct events, LF: Low frequency, HF: High frequency, LT: Low Threshold, HT: High Threshold, Nw: Number of wavelets, Ni: Number of iterations, GA-MP: Gabor atom – Matching Pursuit. Validation methods include (1) Visual detection, consisting of direct comparison of automatically and visually identified HFOs, (2) Visual review, in which experts visually review automatically identified events, and (3) Comparison to SOZ to test whether or not high HFO rates are specific to the SOZ.

Paper	Type of Electrodes (Referencing)	Frequency range	Energy Measure (Parameters)	Artifact Rejection (Parameters)	Validation
Staba 2002	Depth and micro electrodes (not reported)	100-500Hz	RMS amplitude (Tx2, L, D, P, S)	None	Visual review
Zelmann 2010	Depth-electrodes (not reported)	80-450Hz	RMS amplitude (T, D, S), informed by wavelet entropy baseline detection (T)	None	Visual detection for HFOs and baseline (two reviewers)
Blanco 2011	ECoG and Depth electrodes with micro-wires (not reported)	100-500Hz	RMS amplitude (Tx2, L, D, P, S)	Events discarded if similar to local background estimated by a GMM; remaining events were clustered, artifact cluster was rejected	Comparison to SOZ
Chaibi 2013	Depth electrodes	80-500Hz	RMS amplitude after Hilbert	None	Visual detection

	(not reported)		Huang transform (T, L, P)		(two reviewers)
Gliske 2016	Depth electrodes (common average)	100-500Hz	RMS Amplitude (T, L, D, P, S)	Fast transients, DC shifts (L, Tx2, D); Artifact in common average (Tx2, L, D, P, S)	Visual review (three reviewers)
Wu 2018	Depth electrodes (not reported)	80-500Hz	RMS Amplitude (T, L, D, P)	Clustering algorithm using 4 features	Comparison to SOZ
Liu 2018	ECoG and depth electrodes (bipolar)	80-500Hz	RMS amplitude (Tx2, L, D, P, S)	Event considered artifact if the number of zero crossings was greater than 10 (T); clustering using 3 features to isolate HFOs from other events	None
Gardner 2007	ECoG and depth electrodes (not reported)	30-100Hz	Short term line length (T, L)	None	Visual detection and visual review

Dumpelmann 2012	ECoG and depth electrodes (not reported)	80-344Hz	Mean of squared amplitude, short term line length, instantaneous frequency (T, D, S)	None	Visual detection (two reviewers)
Birot 2013	Depth electrodes (not reported)	250-600Hz	Square of filtered signal tapered by Hanning window (T, L)	Two methods to test ratio of power between HF and LF bands (D, LF, T)	Visual detection (one reviewer)
Crepon 2010	ECoG and depth electrodes (bipolar)	180-400Hz	Hilbert Envelope (T)	Peak in Morlet wavelet T-F decomposition	None
Burnos 2014	ECoG and depth electrodes (bipolar)	80-500Hz	Hilbert Envelope (T, D, P, S)	Ratio of power between HF and LF bands (T, LF, HF)	Comparison to SOZ
Liu 2015	iEEG (not reported)	80-500Hz	Median operator threshold based on the median of the standard deviation of filtered data (T, D)	Min/max duration; raw data crosses zero >10 times; K-means clustering based on 3 features (N, T, D)	Comparison to SOZ

Charupanit 2017	Depth electrodes (not reported)	80-250Hz	Iterative procedure to estimate background amplitude and set threshold (T)	None	Visual detection (two reviewers)
Wu 2017	ECoG (not reported)	80-250Hz, 250-600Hz	Two methods: (1) Signal power reconstructed by complex Morlet wavelet and Shannon entropy (T, D, Nw); (2) RMS amplitude deconstructed by the adaptive GA-MP algorithm (T, D, Ni)	None	Comparison to SOZ
Ren 2018	ECoG and depth-electrodes (bipolar)	80-200, 200-500Hz	Distribution of ranges in filtered data (local max-min for adjacent peaks) to estimate background and select threshold	None	Visual detection (three reviewers)

			(LT, HT, P)		
Cimbalnik 2018	Depth and Micro electrodes (not reported)	44-120Hz, 73-197Hz, 120-326Hz, 197-537Hz	Dot product of amplitude and frequency dominance (T, S)	Detection must exceed threshold for 5 features (Tx5)	Visual review (3 reviewers)

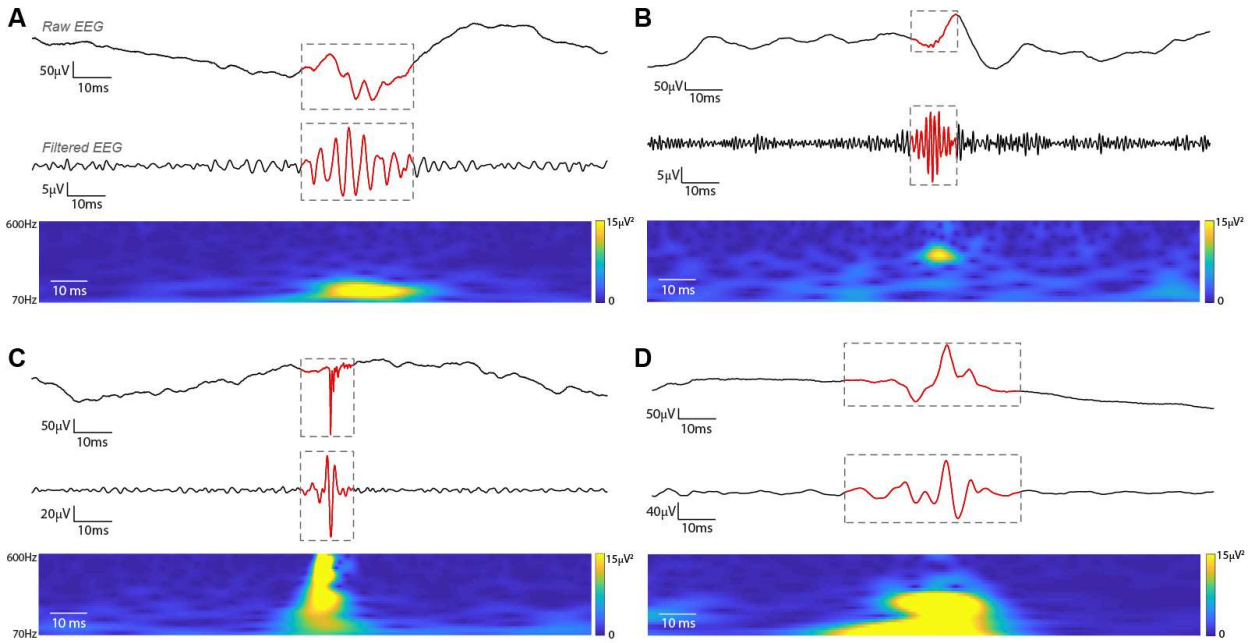

Figure 2.2: Time-frequency analysis can be used to distinguish between HFOs and sharp transients. Representative examples are shown for (A) ripple, recorded from supplementary motor area, (B) fast ripple, recorded from left anterior cingulate, (C) an artifact consisting of a narrow, high amplitude spike, recorded from the right posterior hippocampus and (D) an epileptiform discharge with an embedded ripple, recorded from left anterior hippocampus. Depth electrode recordings are from an 18-year-old male. In

each subfigure, the top trace is the broadband iEEG signal, the middle trace is the 80-500 Hz filtered signal, and the bottom shows the time-frequency decomposition based on Morse wavelets. The events have similar morphology in the bandpass filtered data, but the time-frequency decompositions are unique.

2.2.3.3 Machine learning techniques

Generally, machine learning methods involve extracting features of detected HFOs from a training set of data (generally a certain percentage of the data set) and using those features for classification. Initial detection is commonly done using a high sensitivity detector, such as the RMS detector (108-110). There are two subcategories of machine learning. The first is *supervised machine learning* techniques that use labelled data, e.g., visually marked HFOs and background segments, to train the algorithm; the optimized parameters are then used on the testing dataset. These techniques have been used to separate true HFOs from false HFOs (87), classify HFOs as ictal or non-ictal (108), and distinguish between resected and non-resected tissue (39). Methods include neural networks (87), logistic regression and K-nearest neighbors (108), and support vector machines (39, 108). In contrast, the second subcategory is *unsupervised machine learning* techniques that do not require visually marked data to train the algorithms. The algorithms cluster the initial detections based on their similarity to one another, either using features or the event itself. The optimal number of clusters can be chosen using various techniques (42, 71, 109, 110). Based on the characteristics of their members,

clusters can then be empirically interpreted as containing ripples, fast ripples, or false HFOs due to artifacts or sharp transients, thus improving detector specificity (71, 109, 110) or aiding classification of SOZ and non-SOZ channels (42). All of these studies used Gaussian mixture models, sometimes in combination with other clustering algorithms.

2.2.4 Testing and validation of automated algorithms

After choosing methods for initial detection and rejection of false positives, the performance of automated algorithm can be tested using an independent dataset. This procedure can be done using event-level validation techniques, clinical validation techniques, or a combination of both.

Event-level validation techniques can be used to verify the characteristics of detected events relative to visual detection or inspection:

(1) *Comparison to visual detection.* The most frequently used test for automated algorithms is to compare the automatically detected HFOs with those visually marked by two or more reviewers. This enables the calculation of detector sensitivity and specificity, and the goal is to achieve high overlap between automatic and visual detection, with the visually marked events treated as the ground truth. However, this procedure is time and labor intensive, and subject to the investigator bias inherent in visual detection (67, 68).

(2) *Verification via visual review.* An alternative, when the dataset is very large, is to visually examine a random sample of the detected events, e.g., 2000 out of 1.5 million

events (79) or three out of 11 patients (87). It is then possible to estimate the percentage of automatically detected events that resemble true HFOs or are false positives due to the filtering of artifacts or sharp transients. Here, the goal is to ensure that the number of automatic false positive detections is sufficiently low, and this procedure is less time intensive than comparison to visual detection. However, this again assumes that visual detection is the ground truth, despite its drawbacks. It is also not possible to know if the detector missed events (false negatives) or whether the detections are a representative sample of true HFOs.

Clinical validation techniques can be used to verify that the events detected by the automated algorithm are a biomarker of epilepsy:

(1) *Comparison to SOZ.* Detectors can be validated by identifying the channels with high ripple and/or fast ripple rates and comparing them with the clinically determined SOZ. This strategy is aimed at measuring the utility of automatically detected HFOs as an interictal biomarker of the SOZ. If the detection algorithm has been previously tested using visual detection or visual review, this serves as further validation of both the algorithm and the value of visually marked HFOs. If the algorithm has not undergone prior testing, there is no guarantee that the automatically detected events would have been visually marked. In this case, if significant differences between SOZ and non-SOZ

channels is demonstrated, basic characteristics of the detected events (duration, frequency, amplitude, etc.) should be analyzed.

(2) *Comparison to surgical outcome.* Lastly, a detector can be validated by comparing its output, e.g., the HFO rate for each electrode, to the resected volume and seizure outcome after surgery. In these studies, it is common to analyze the R or FR "resection ratio," which denotes the percentage of brain regions exhibiting high HFO rates that were resected. In theory, patients with high resection ratios should have good surgical outcome. Here, the goal is to validate HFOs as a biomarker of the EZ. This form of validation has more clinical utility than comparison to the SOZ, as surgical removal of the SOZ does not always result in seizure freedom. However, there are significant limitations to interpreting outcome. Tissue beyond the HFO-generating regions is often resected, which limits interpretation of seizure free outcomes, and if the seizures persist, this may be because some HFO-generating regions were not sampled. These studies also generally require more subjects, with integration of imaging and electrophysiological data and collection of long-term follow-up data. As with comparison to the SOZ, the interpretation of automatically detected events will depend on whether the detector was previously tested using visual detection or review.

2.2.5 Parameter optimization

The automated methods in Table 1 involve the use of multiple inter-dependent parameters for initial detection and rejection of false positive detections. Changing these parameters can greatly affect the output of the detector (111). Therefore, optimizing detector parameters is an important step in the implementation of an automatic detector. In order to achieve sufficient sensitivity and specificity, the parameters for initial event detection (Section 2.2) and rejection of false positive detections (Section 2.3) must be adjusted for each data set (111), for each subject (47), or for each channel of iEEG (93). In that sense, these detectors are not fully automated.

To determine the optimum parameters, the steps described in this section are applied to a randomly selected subset of data (39, 83) or patients (87, 91), sweeping through parameter values. The remaining, usually larger, subset is used for testing the detector performance. A hold-one-out method can also be used to select data for optimization and testing, especially when limited data are available (79). Events automatically detected in the training dataset are visually inspected, or they are compared against visually marked events, the visually determined SOZ, or clinical outcome (see Section 2.4). The parameter set that gives the best results is then applied to the testing dataset to measure detector performance. Alternatively, it has been suggested that varying the detection parameters over a small range can be used to test the robustness of

SOZ localization; if a channel has a high HFO rate for multiple sets of parameters, this suggests that the HFOs are easily separated from the background and increases confidence in classifying the channel as SOZ (89).

It is important to note that the parameters used for automatic detection are inter-dependent. For example, if the energy threshold is decreased, the duration of the detected events will increase. Naturally, optimization becomes increasingly difficult when there are many inter-dependent parameters. Therefore, it can be advantageous to use a detector that was designed to minimize the number of parameters, e.g., Charupanit et al (93).

2.3 Comparison of automated detectors

Automated detectors are often validated on novel data sets, which are recorded at different centers with electrodes of different sizes, and detection can be implemented with varying parameters and frequency ranges. Therefore, directly comparing performance metrics of different detectors is challenging. Detectors can only be accurately compared when they are tested on the same dataset and the parameters for each detector are optimized for that dataset. Overall, we identified eight studies that compared their new detector to existing detectors on the same data set.

In particular, two studies compared detectors after implementing independent optimization procedures for the parameters of each detector. First, Zelmann, Mari (111)

compared the MNI detector to the line length (LL)(69) and RMS detectors (72) on the same dataset used to optimize parameters for the MNI detector. In addition to using the parameters from the original papers for detection, the authors also optimized the parameters using a subset of the data and compared performance using the optimum values. When the original parameter values were used, the detectors performed very poorly relative to the performance stated in the original papers, but significant improvement was seen when using the optimized parameters. This emphasizes the importance of parameter optimization for detector performance. With optimum parameters, the MNI detector fared marginally better than the other two. However, the LL detector was originally made for a frequency range of 0.1 to 100Hz, while it was tested here for 100-500Hz. Second, Charupanit and Lopour (93) compared their detector to the RMS detector using the same dataset. The two threshold selection methods described in the paper (iterative and non-iterative) and the RMS detector performed comparably when optimization was done for all channels. The iterative method performed significantly better in a rigorous cross-validation test, where optimization was done on a subset of channels and testing was done across the remaining channels.

Gardner, Worrell (69) compared their LL detector against the RMS detector, modifying it to suit the clinical dataset. The LL detector performed significantly better, but the parameters of the RMS detector were not optimized, and it was not originally

designed for use in the 0.1 to 100Hz frequency range. Cimbalnik, Hewitt (84) compared their CS algorithm to the RMS and LL detector in a dataset including human, rodent, and canine recordings. They reported superior detection accuracy and temporal localization using their algorithm. Burnos, Hilfiker (91) also compared their detector to the RMS and LL detector; in two patients, the detectors performed equally, while in the other four patients their detector did considerably better. Dumpelmann, Jacobs (87) compared theirs to the LL detector, and ROC analysis showed that theirs was superior. Ren, Yan (78) compared their detector to the MNI, RMS, LL and Hilbert detectors. For both ripples and FRs their algorithm had significantly higher sensitivity and specificity. Similarly, Wu, Wan (71) found that their proposed detector performed better than five existing detectors. However, in all of these comparisons, the existing detectors generally performed worse than they did in the original publication. This may be due to three important limitations. First, the detector parameters were not always optimized prior to applying them to the new dataset. Second, detectors were sometimes tested on datasets or in frequency ranges that were entirely different from the ones they were designed for. Third, if visual marking from one center is used to create the gold standard for comparison, there may be unconscious bias toward the detector from that center, as those doing the manual marking may have knowledge of how that detector works.

2.4 Relationship between automatically detected HFOs and surgical outcome

Fifteen studies published between 2011 and 2019 used automatic detectors to relate the presence of HFOs to surgical outcome (Table 2). All studies were retrospective, except Jacobs et al (47). Most studies used interictal HFOs recorded during slow wave sleep, although one study used ictal recordings (112) and two studies used intraoperative recordings (98, 113).

In seven of the studies, previously validated algorithms were used to detect HFOs. Eight studies employed novel, unpublished automatic detectors, rather than using one of the externally validated algorithms in Table 1. In each case, the algorithm parameters were optimized for the study's data set; this would ideally be done using a separate training dataset, but this information was not always provided. These novel detectors were typically combinations or variations of standard techniques, including RMS amplitude (44), Hilbert envelope (43), T-F analysis (114), or machine learning methods (39, 115, 116). In addition to the studies in Table 2, a considerable number of recent papers used visual markings to identify HFOs for analysis in post-surgical outcome. While this may suggest concern about the robustness of automated detection, multiple studies have reported that visual and automated detection produce similar results (47, 98, 117).

Despite the wide variability in detection methods, results using automated algorithms have been relatively consistent. Two studies reported that complete resection of brain regions exhibiting high HFO rates correlated to good outcome, without separating them into ripple and fast ripple bands (39, 118). Higher ripple resection ratios were frequently associated with improved surgical outcome (43, 61, 98, 119, 120), and all of the studies that reported significant results for ripples also reported significance for fast ripples. However, two studies reported a significant link between HFO resection and surgical outcome only in the FR band (61, 114). Generally, FRs were found to be a better indicator of surgical outcome (43, 61, 98, 114, 119), although one study reported the opposite result (44), and analyses of some larger datasets have not shown FR to be more specific than R (47, 79, 80, 109). Other studies reported that that concurrent HFO and low frequency oscillations were a better marker than either alone (115), and that a machine learning technique could be used to automatically rank and classify channels inside and outside the SOZ based on HFO rate (116). The significance of HFOs as a predictor of outcome compared to spikes is not clear, as two studies reported conflicting results on this (92, 121).

On the other hand, we found two studies reporting that removal of HFOs was not significantly correlated to surgical outcome (47, 113) The results of a meta-analysis (117) indicated that while nearly all studies found that increased R/FR resection increased

seizure freedom post-surgery, this relationship was significant in only half of the studies. Moreover, the only prospective multicenter study in Table 2 reported non-significant results at a center level, where iEEG measurements used different recording techniques, even though there was correlation between high HFO region resection and surgical outcome at a group level (47). The results did not improve with visual detection. This may have been due to the analysis techniques used, the presence of physiological HFOs, under-sampling of the brain when recording iEEG, differences in types of epilepsy, or differences between chronic recording and intraoperative monitoring. It is also possible that HFOs are not specific to the EZ in all patients.

Table 2.2: Papers that relate HFOs and clinical outcome using automatic detection

Abbreviations – FCD: focal cortical dysplasia, EMD: empirical mode decomposition, LFO: low frequency oscillation, FR: fast ripple, NA: not applicable (not tested), R: ripple, SVM: support vector machine

Reference	Data	No. of patients	Frequency Range	Detector	Removal significantly correlated to improved surgical outcome?		
					R	FR	Comparison
Akiyama 2011	ECoG and depth electrodes (bi-polar)	28	R: 80-200Hz FR: 200-300Hz	New detector based on Hilbert transform + threshold	Yes	Yes	FR>R
	Other result: SOZ not correlated with seizure outcome.						

Cho 2014	ECoG; some depth electrodes on suspected lesions (common electrode, Pz)	15	R: 60-200Hz FR: 200-500Hz	New detector based on Crepon 2010 and Staba 2002; false positive detection using power and amplitude relative to background	Yes	Yes	R>FR
van klink 2014	ECoG (bipolar)	14	R: 80-250Hz FR: 250-500Hz	Zelmann 2010; parameters were optimized on training data; spikes were visually identified	No	Yes	FR>R
Dian 2015	ECoG (bipolar)	6	LFO: <80 Hz HFO: 80-400Hz	New detector based on EMD & feature extraction for LFO & HFO; SVM to classify channels; used separate training and testing datasets	NA	NA	NA
	Other result: HFO+LFO more consistent than LFO or HFO alone; analyzed 3 subjects						
Sun 2015	ECoG (not reported)	4	R: 80-250Hz FR: 250-500Hz	New detector; Advanced source analysis software	Yes	Yes	FR>R

Fedele 2016	Intraoperative ECoG (bipolar)	54	R: 80-250Hz FR: 250-500Hz	New detector; events exceeded threshold based on Stockwell entropy for a min time, confirmed using HF peak in Stockwell transform; multichannel analysis to reject events occurring broadly	Yes	Yes	FR>R
	Other result: In post-resection intraoperative ECoG, FRs have 100% PPV and Ripples have 100% NPV						
Fedele 2017	ECoG, data acquired with custom device and low noise amplifier (bipolar)	9	FR: 250-500 Hz	New detector; HFO detection & artifact rejection using Fedele 2016, with T-F analysis as in Burnos 2014	NA	Yes	NA
Fedele 2017	ECoG and depth electrodes (bipolar)	20	R: 80-250Hz FR: 250-500Hz	Burnos 2016, with baseline detected separately for FR and R	Yes	Yes	R more sensitive; FR more specific
	Other result: FRs co-occurring with ripples predict seizure outcome better than each individually (100% specificity)						

van 't Klooster et al 2017	Intraoperative ECoG (bipolar)	54	R: 80-250Hz FR: 250-500Hz	Zelmann 2010 optimized for ECoG bipolar data; artifacts visually detected	No	No	NA
	Other result: Presence of FRs in the post-resection ECoG, given incomplete removal of FRs based on pre-resection ECoG, indicated worse outcome. None for ripples.						
Liu 2017	ECoG (not reported)	1	80-500Hz	Liu 2016	NA	NA	NA
	Other result: HFOs provided more localized SOZ than spiking activity.						
Jacobs 2018	3 centers; chronic depth electrodes at two centers, intra-operative ECoG at one (not reported)	52	R: 80-250Hz FR: 250-500Hz	Zelmann 2010; 3 patients were used for training detector at each center	No	No	NA
	Other result: At an individual level, no reliable prediction could be made about outcome using HFOs						
Cuello-Oderiz 2018	SEEG; patients with FCD (bipolar)	21	R: 80-250Hz FR: > 250Hz	von Ellenrieder 2016; parameters optimized using first one minute of data	Yes	Yes	Same specificity, but FRs had lower false

							positive rate
Cimbalnik 2018	ECoG and depth electrodes (not reported)	90	65-600Hz	New detector; physiological and pathological HFOs detected separately. Multiple feature cascade detector, trained and validated on separate data sets	NA	NA	NA
	Other result: Failure to resect high HFO rate regions associated with poor outcome.						
Sumsky 2019	ECoG and depth electrodes (common average)	14	>80Hz	New detector; Gliske 2016 plus SVM classifier based on HFO rate to identify SOZ channels	NA	NA	NA
	Other result: The method predicted the resected volume only in cases with good post-surgical outcome						

2.5 Discussion and Recommendations

There are a wide range of challenges associated with HFO detection, the most prominent one being the lack of a strict physiological definition of an HFO. This precludes the development of a universally applicable detector. For every new project, researchers must choose a detector, optimize the parameters, and validate its performance. Drawing from the current literature reviewed here, we propose some general guidelines for this process, which are detailed below and summarized in Table 3.

Which detection algorithm should be used? Because the energy-based metrics for the detectors in Table 1 are correlated (Figure 2), the results of their initial detection will be comparable when optimal parameters are used. Evidence for this has come from studies comparing different detectors on the same data set (Section 3), which showed that once the detector parameters were properly optimized, the performance of the detectors was generally comparable. However, the results of the initial detection will include false positives due to artifacts and sharp transients. Therefore, implementation of false positive rejection methods may have a larger effect on the HFO rate than initial detection. In particular, methods based on the time-frequency decomposition are likely to be the most stringent. However, post-processing steps come at the cost of increasing the complexity of optimization, as more parameters are needed. Overall, the consistency of results using a

wide range of detection methods suggests that choice of detection scheme is not critical; it is fine to use a simple technique, preferably one that has already been validated, as long as parameters are optimized for the dataset. In the future, more work is needed to understand the unique underlying physiology of HFOs, in order to guide development of more specific detectors.

How should detector parameters be optimized? All automated algorithms include parameters, such as a window size for the energy calculation and thresholds for amplitude, duration, and number of peaks. Some studies implement published detectors with fixed parameters. However, several studies have shown that proper selection of these parameters is a critical step in the detection of HFOs, and there are currently no recommendations for how this should be done. The parameters are often dependent on one another, and most studies have focused on optimization of the energy threshold relative to the background. However, all parameters should be varied over the widest possible range, and the best performance can be chosen using the Youden index of (sensitivity + specificity – 1) (106, 126). Then the selected values of all parameters should be reported along with the results. The optimal set of parameters is likely to be patient specific. For this reason, optimizing using small samples from each patient (e.g. use the first five minutes of data from each patient to select the parameters, then apply those parameters to the rest of the subject's data) may produce better results than optimizing based on a subset of patients

(e.g. use all data from three subjects to select the parameters, then apply those parameters to the rest of the subjects). There is even some evidence to suggest that the parameter selection should be channel-specific (93). It has also been suggested that a normalization pre-processing step to reduce the variance between data from different sources can provide more consistent detection results (84). In the future, more work is needed to understand the robustness of HFO detection to changes in the parameters and recording setup and to develop automated patient-specific optimization techniques simple enough to be used in a clinical setting.

How should a new detector be tested and validated? After parameter optimization, the detector can be tested and validated via comparison to visually detected events, visual review of automatically detected events, comparison to the SOZ, and comparison to surgical outcome. The approach should be chosen based on the specific goal of the study. Ultimately, validating an algorithm against the resected volume and surgical outcome is the clinical gold standard (127), but if consistency with visually detected HFOs is desired, the output of the algorithm should first be tested against visual marking or visual review. For all methods, the validation should be done on an independent dataset that was not used for parameter optimization. In order to robustly validate an algorithm, the detectors and parameters should be consistently applied across studies. We found many examples of detectors validated on one type of data (or in one frequency band) being used without

optimization in a different setting, and it is not uncommon for a study to use a variation of an existing detector without repeating the validation. This has led to a myriad of different detectors, making comparisons between studies almost impossible. In the future, comparing new detection methods directly to a well-understood benchmark algorithm using the same dataset can help alleviate this problem, and authors should make the code for the new algorithm freely available. If the two algorithms perform comparably, use of the previously published algorithm is preferable. Similarly, when comparing HFO detection to the SOZ or surgical outcome, using multiple detection algorithms and varying detection parameters can help verify that the results are robust to these changes.

How much data should be used for detection? While initial HFO studies used only a few minutes of data per patient, due to the laborious nature of visual HFO marking, the use of automated algorithms enables and warrants analysis of larger datasets. Anti-seizure medications and the occurrence of seizures will affect HFO rates, so it is important to perform HFO detection on multiple, independent segments of data. It is currently standard practice to use interictal data collected during slow wave sleep. Short segments of data can be clipped periodically overnight, at least one hour away from any seizure, collected from multiple nights if possible.(114, 128) When reporting the results, an analysis of the variability of the measurements over time can be included. In the future, more work

is needed to understand the stability of SOZ localization as a function of the dataset length, and characteristics of HFOs recorded during wakefulness should be explored.

How can a threshold for the HFO rate be chosen? After detection and the calculation of HFO rate for each channel, a threshold must be chosen above which the HFO rate is deemed pathological. For a given patient, the goal of this process is to identify any subset of channels with anomalously high rates. In theory, brain regions with HFO rates exceeding this threshold are potential surgical targets. This is not a trivial task, as the overall HFO rates and differences between epileptogenic and non-epileptogenic regions are patient-specific. Large clinical studies have shown that the variability of HFO rates between patients is too variable to establish a universal threshold for HFO levels (41, 129), and there is no guarantee that the channel with the highest HFO rate is abnormal (109). Differences in rate can also occur due to the presence of physiological oscillations, different electrode types (37) (but see also (50)), and different types of epilepsy. Several automated methods have been proposed. One commonly used method is to assume that HFO rates exceeding a pre-determined rate (usually empirically determined) are pathological (98). Others include Kernel Density Estimation (79), Kittler's method (43), Tukey's upper fence (104), and the half maximum method (91). In the future, additional development of patient-specific optimization techniques is needed. Because the determination of a threshold for HFO rate is directly tied to the HFO detection technique

and its specificity, the methods for accomplishing these two tasks will need to evolve together.

Are there alternatives to the discrete measurement of HFO rate? Although the literature on HFOs is dominated by discrete detection of HFO events and the use of rate as a biomarker for the SOZ, several alternatives have been proposed. Some studies have suggested measures that can be applied to the entire high frequency signal, rather than detecting discrete events. For example, it was reported that the skew in the distribution of power values was higher in the SOZ compared to non-SOZ for three frequency bands (5-80Hz, 80-250Hz, 250-500Hz)(130). Other studies have measured cross-frequency coupling of high frequency amplitude with the low frequency phase (delta and theta bands), generally quantified by the modulation index (MI). A recent study in 76 patients showed significantly higher MI z-score in the SOZ compared to regions outside the SOZ (131). Further, a multi-variate logistic regression analysis found that the model predicted outcome better in 123 patients when MI was included as a variable. Guirgis et al. used eigenvalue decomposition of MI values to delineate a "region of interest" and found that when this region was spared during surgery, patients were less likely to be seizure free (132). Weiss et al. found that coupling between high gamma (80–150 Hz) amplitude and slow wave (1-25Hz) phase was higher in the "ictal core" (territories that were fully recruited to the seizure) compared to the periphery (133), which could potentially aid in

more precise localization of cortical regions for epilepsy surgery. Lastly, Ibrahim et al. found that coupling between high frequency amplitude and theta and alpha phase was significantly elevated in the SOZ compared to non-epileptic regions (134). It should be noted that these studies used ictal data, which is more challenging to collect and analyze than interictal data.

Zweiphenning et al. calculated network connectivity by applying short-time direct directed transfer function for different frequency bands (135). They found that, in patients with good surgical outcome, the total strength and the net strength of outgoing propagations in the gamma and ripple bands was higher in electrodes covering the resected tissue than in the electrodes covering tissue that was not resected. An earlier study done by the same group found local enhanced connectivity of channels showing epileptiform events in the FR-band functional network (136). They hypothesized that these hubs might cover the HFO-generating networks and their resection might lead to better outcome. González Otárula et al. found that interictal HFOs are organized in networks and, indicate that the resection of the source channels may be necessary for seizure freedom (137). However, they found that in their dataset, the resection of these channels did not prove to be more advantageous over resecting channels with highest HFO rates.

Many of the studies described above do not detect conventional discrete HFOs, but instead look at all high frequency activity. Thus, these methods address a fundamental

limitation with using HFOs: the lack of an objective definition of an HFO. Also, measuring characteristics of continuous activity may require less computation time than detecting discrete HFOs. Lastly, because these approaches do not tend to define the semiology of the events they intend to detect, they typically require fewer parameters, thus making patient specific parameter optimization easier. Further research into these methods is needed to assess the efficacy of continuous HFA as a biomarker of the SOZ.

Other HFO characteristics, including amplitude, duration and peak frequency are potential alternatives to rate as a marker of the SOZ. Malinowska et al. found that in addition to HFO rates, HFO amplitudes and frequencies significantly differ between SOZ and non-SOZ in ictal, non-ictal and pre ictal periods (138). Pail et al. found that both ripple and fast ripple durations were shorter in the SOZ than outside it, and the relative HFO amplitudes were also higher in the SOZ (65). Charupanit et al. identified anomalous high frequency activity that stood out from the background and found that while their rates were similar in and outside the SOZ, there was a significant difference in their amplitudes between the two regions (75).

Overall, the results using automated HFO detection for determination of the SOZ and comparison to surgical outcome are promising, and these techniques are gradually becoming accepted as robust and reliable. They make it possible to analyze large amounts of data very quickly. Standardized practices for the implementation and optimization of

detectors will facilitate comparisons across multiple studies and identification of generalizable trends, which will lead to more rapid advancements in the clinical use of HFOs.

CHAPTER 3

A NOVEL METHOD FOR DYNAMICALLY ALTERING THE SURFACE AREA OF INTRACRANIAL EEG ELECTRODES

3.1 Introduction

Intracranial electroencephalography (iEEG) is an invasive technique that measures electrical activity of the brain. It is used for the diagnosis, monitoring, and treatment of neurological diseases, such as epilepsy (139) and Parkinson's disease (140). It has also been critical to the development of devices such as neural prostheses (141) and brain computer interfaces (BCIs)(142). iEEG measurement is done using subdural grids or strips of electrodes placed on the surface of the cerebral cortex or depth electrodes inserted into brain tissue. The signals measured by iEEG electrodes reflect the aggregate electrical activity of the cortical neurons in the immediate vicinity (16). The voltage measured by an electrode is thought to reflect the average potential distribution under its uninsulated contact area (143-145). The signals recorded by a subdural grid depend on a number of factors, including the impedance, geometry, and spacing of the electrodes (16).

Because the number of neurons whose electrical activity contribute to the iEEG signal is proportional to the electrode contact area, electrode size is an important factor

in measurements. A multitude of electrodes of different geometries are used for intracranial EEG measurement. Penetrating microwires with diameters as low as 12 μm have been used for *in vivo* single unit recordings (146, 147). Micro-electrocorticography (μECoG) electrodes, which have potential uses in both BCI and clinical applications, have diameters in the range of 10 μm to several hundreds of micrometers (147, 148). Standard clinical macroelectrodes for iEEG have exposed diameters that range from 0.86 mm to 3 mm (20). Therefore, it is critical to understand the precise relationship between electrode size and iEEG measurement to better interpret and compare the results of studies with different methodologies.

In silico studies of the effect of electrode size on iEEG signal characteristics present conflicting pictures. Nelson and Pouget (149) developed a physical model that predicted electrodes with larger surface area would have higher correlation between them. Their model also suggested that, as the voltage profile underneath the electrode becomes more inhomogeneous (as it would with increasing surface area), electrodes with different contact areas are more likely to measure different average values. Ollikainen, Vauhkonen (143) simulated rectangular electrodes with surface areas that varied from 1.5 cm^2 to 5 cm^2, measuring electrical potential from a single source. They showed that smaller electrodes had more sensitivity to localized voltage differences than larger electrodes. This is consistent with the idea that each electrode measures the average potential of the

underlying tissue; therefore, using larger electrodes results in loss of spatial information. Furthermore, these simulations showed that the current distribution on the surface of the electrode is non-uniform and concentrated at the boundaries, with the distribution becoming more complex when larger electrodes are used. Moffitt and McIntyre (150) developed a model demonstrating that smaller contacts exhibited higher signal amplitude when neurons were close to the electrode. Contrary to this, the model developed by Suihko, Eskola (151) suggested that changing the electrode size will cause only small changes in the sensitivity distribution and is therefore not a key factor in iEEG measurements. The model of Lempka et. al (152) also suggested that the size of the recording micro-electrode does not have much effect on signal amplitude, while impedance does.

A number of studies using penetrating microelectrodes have analyzed neuronal action potentials and the effect of electrode size on their measurement (153-156). Anderson et al. posited that, in the context of action potentials, as the size of the electrode increases, the "listening sphere" increases, but the signal-to-noise ratio (SNR) decreases (154). However, a study by Ward et al. in an animal model found no significant difference in the action potential SNRs for implanted micro-electrode arrays (MEAs) of different surface areas (155). The results of such studies can be confounded by differences in the

electrode coating and other techniques to lower the electrode impedance, independent of the electrode diameter.

In contrast, there are few *in vivo* studies analyzing the effect of electrode size on general iEEG characteristics, such as amplitude or waveform morphology (157, 158). In applications like BCI and neuro-prosthetic devices, the ability to accurately classify neural signals associated with different cognitive tasks is of utmost importance. Studies in this field have shown that smaller electrode size and higher grid density (e.g., 100μm diameter and 1mm pitch) enable the recording of signals from smaller spatial scales, making them more suitable for these applications (158-160). In human studies of epilepsy, various electrode sizes have been used to measure high frequency oscillations (HFOs), a candidate biomarker for epileptogenic brain tissue. HFOs are highly localized, transient iEEG events characterized by high-amplitude 80-500 Hz oscillations. Using human intracranial EEG, Chatillon et al (51) analyzed HFOs recorded with electrodes of different sizes (ranging from 0.02 to 0.09 mm^2) and found that the difference in recordings was not clinically relevant. On the other hand, Worrell et al. reported that smaller electrodes recorded more HFOs than larger electrodes (diameter of 40μm, as opposed to 2.3mm), particularly in the 250-500 Hz frequency range (37). Another study by Boran et al. found that intraoperative HFO measurement is aided by the use of an electrode grid with smaller electrodes and higher density (exposed diameter of 2.3 mm and inter-electrode distance

of 5 mm), compared to a standard ECoG grid with 5 mm diameter and 10 mm spacing (161). It has also been shown that discharges resembling interictal epileptiform activity, but confined to much smaller spatial scales, can be seen using micro-electrodes but not standard-size electrodes (162, 163). Knowledge of the relationship between electrode size and iEEG biomarker features would inform epilepsy surgery and invasive monitoring, with the potential to improve patient outcomes.

Therefore, the goal of this study was to directly measure the impact of electrode surface area on iEEG signal characteristics in the human brain. Previous work in humans has relied on simultaneous iEEG recordings using electrodes of different sizes, with each electrode implanted in a different location. In those cases, it is not clear if the resulting differences are due to electrode size or regional differences in brain activity. An alternative methodology is to record sequential iEEG measurements using electrodes of multiple sizes, placed over the exact same region of neural tissue. However, because implantation of intracranial electrodes is an invasive procedure with inherent risk to the patient, this presents logistical and ethical challenges. Here, we present a solution to this problem: a method to alter the size of an intracranial recording electrode after implantation. This enables multiscale measurements from a single region of the brain, allowing for a more direct comparison of iEEG signals recorded using electrodes of different sizes. We also examine how electrode size affects basic iEEG properties, such as power spectrum and

amplitude, and we explore the effect on the morphology of interictal epileptiform discharges (also called epileptic "spikes"), which is a common electrographic event in epilepsy patients.

3.2 Theoretical basis for altering electrode size via electrical shorting

Our method to alter the surface area of an implanted grid electrode involves electrically connecting adjacent electrodes together (via physical shorting) to generate a range of effective surface areas. For each individual electrode, the recorded signal reflects the average voltage across the uninsulated surface; therefore, connecting two adjacent electrodes will report the average of the two individual electrodes, equivalent to doubling the electrode surface area (144, 145). In this way, we can alter electrode size while recording data from the exact same region of neural tissue within the framework of standard clinical care.

To provide a theoretical basis for this approach, we used a widely accepted electrical circuit model of the metal electrode (Figure 1A) (164, 165). In Figure 1B, two cortical surface electrodes (with impedances Z_{e1}, Z_{e2}) are each connected to an amplifier (with impedances Z_{a1}, Z_{a2}). The electrodes sense independent voltage sources in the neural

tissue (V_{s1}, V_{s2}), which interact through the impedance of the brain tissue (Z_{b1}, Z_{b2}) and a shunt impedance between the two brain regions (Z_{12}).

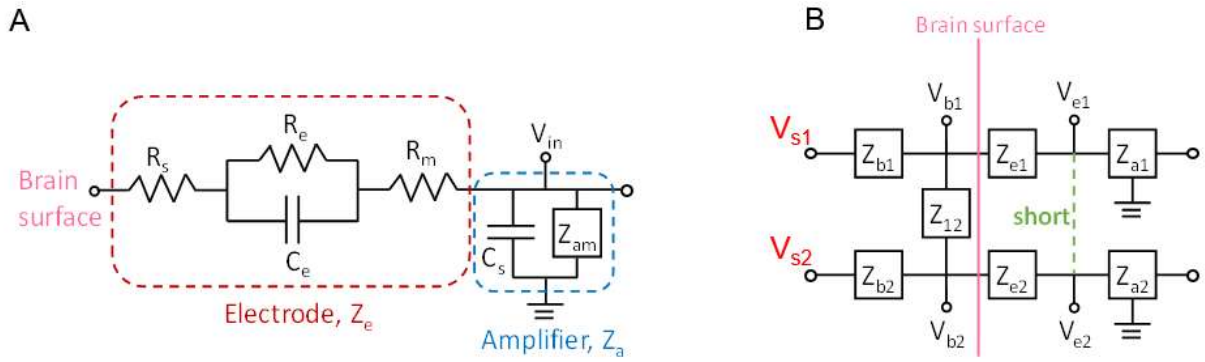

Figure 3.1: (A) Circuit model of a single electrode (red box) connected to an ideal amplifier (blue box). (B) Circuit model of two electrodes (Ze1, Ze2) on the surface of the brain that can be shorted together (green dashed line) to simulate an electrode with twice the surface area.

In the case with no shorting, each electrode measures the voltage in the underlying tissue, $V_{e1} \approx V_{b1}$ and $V_{e2} \approx V_{b2}$, assuming the input impedance of the amplifier is large. When the two electrodes are shorted, they measure a common voltage V_e given by the equation:

$$V_e = \frac{Z_{e2}}{Z_{e1} + Z_{e2}} V_{b1} + \frac{Z_{e1}}{Z_{e1} + Z_{e2}} V_{b2}$$

The full derivation of this equation can be found in the Appendix. If we assume the electrode impedances Z_{e1} and Z_{e2} to be equal, we find that the voltage measured at the surface is $V_e = \frac{V_{b1}+V_{b2}}{2}$

This result suggests that, when two electrodes are shorted together, the voltage measured by the amplifiers is a linear combination of the voltages sensed by each individual electrode (V_{b1} and V_{b2}). Because signals measured by iEEG electrodes are thought to reflect the average neural activity underneath them, this averaged activity should be equivalent to that sensed by a larger electrode covering the same cortical area as the two smaller electrodes. Here, we perform an experiment to directly test that hypothesis. If the hypothesis is true, physically shorting two adjacent electrodes can increase the effective surface area, thus providing a means to investigate the same region of neural tissue with electrodes of different sizes.

3.3 Methods

3.3.1 *In vitro* validation experiment

We performed an *in vitro* experiment to test the prediction from the circuit model that the signal recorded when electrodes are shorted together is equal to the average of the individual electrode signals (Section 2). A disc of agar gel was used as the substrate because it has been shown to mimic both the structural and electrical properties of brain tissue (166). The gel was mixed with water and NaCl to achieve a conductivity of ~0.5 S/m, to approximately match that of brain tissue (167). For this experiment, we used three different types of electrode grids: (1) "Small" electrodes (8x8 grid, 1.17mm exposed

diameter, 3mm inter-electrode spacing, Ad-Tech FG64C-MP03X-000), (2) "Medium" electrodes (4x4grid, 1.66mm exposed diameter, 6mm inter-electrode spacing, FG16C-SP06X-ORD – custom made), and (3) "Large" electrodes (4x4 grid, 2.34mm exposed diameter, 6mm inter-electrode spacing, FG16C-SP06X-000). Note that the areas of the medium and large electrodes correspond to double and quadruple the area of the small electrodes, respectively. Each grid of intracranial electrodes was placed in the center of an agar gel disc (Figure 2A). Bipolar electrical stimulation was applied to the gel substrate using a 2-by-10 electrode strip, and a second 2-by-10 strip was placed on the opposite side for use as an electrical reference. The stimulus was a sine wave of 350µV amplitude, with frequencies ranging from 10-70Hz. The sinusoidally oscillating dipole created an electric field in the gel substrate that was sensed by the experimental grid of electrodes (Figure 2B). Thirty seconds of data were recorded from these three grid types using Biopac EEG 100C amplifiers and were sampled at 500Hz, keeping the location of each grid on the substrate fixed relative to the stimulation electrodes.

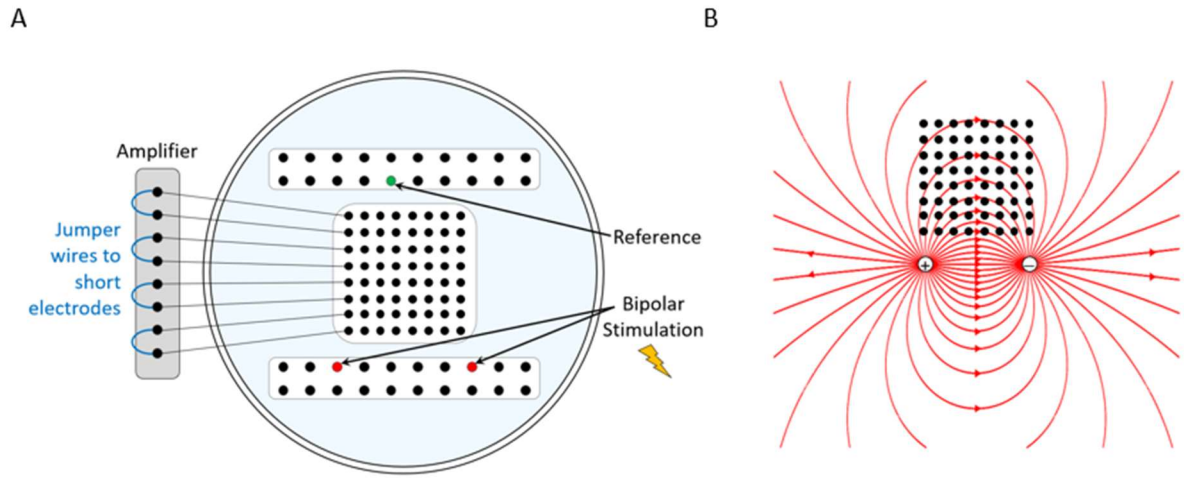

Figure 3.2: (A) Schematic of the agar gel disc with the 8x8 grid of electrodes, the 2x10 strip containing the reference electrode, and the 2x10 strip used for stimulation. An example is shown in which four pairs of electrodes are shorted at the amplifier using jumper wires. (B) The grid of intracranial electrodes (black dots) and the electric field lines of the dipole being sensed by the grid (red lines).

After collecting data from every individual electrode on each grid during the first set of recordings, we reconfigured the recording setup for the small electrode grid by using jumper wires to electrically short specific sets of electrodes together (Figure 2A). First, adjacent pairs of electrodes were shorted together to form the "pair" configuration (n=32 pair electrodes), and then 2-by-2 groups of four electrodes were shorted together to form the "quad" configuration (n=16 quad electrodes). The in vivo experiment in Section 3.2 uses the same configurations (Figure 3A). The bipolar stimulation described earlier was applied individually to each configuration, and the resulting electric field was measured at each pair and quad electrode.

Then, to verify that shorting adjacent electrodes mimics an electrode with larger surface area, we compared the signals obtained from the medium electrodes to the signals from the "pair" recordings, and we compared the large electrode recordings to the "quad" recordings. For each comparison, the electrodes being compared to one another had equivalent effective surface areas; if our hypothesis is correct, their recorded signals should also be equivalent. Further, we compared each of these sets of signals (medium vs. pair, large vs. quad) to the waveforms produced by mathematical averaging of the corresponding small electrode recordings. For example, we averaged pairs of signals from the small electrode recording and compared those to the physically shorted "pair" electrode signals. We did an analogous comparison for the "quad" signals. If the model in Section 2 is valid, mathematical averaging, physical shorting, and the equivalent larger electrodes should all produce the same signal. We used a rank-based non-parametric approach (Wilcoxon rank sum test) to test the differences in RMS amplitude for the signals obtained from the various electrode configurations.

3.3.2 *In vivo* experiment

3.3.2.1 Human data collection

The *in vivo* portion of this study was approved by the Institutional Review Board of the Children's Hospital of Orange County (CHOC). Informed consent was obtained prior to involvement in the study. Three human subjects with medically intractable

epilepsy were each implanted with a high-density 8x8 subdural grid of intracerebral EEG electrodes (Ad-Tech FG64C-MP03X-000) in the clinically determined SOZ as part of phase 2 pre-surgical invasive monitoring. Patient information is given in Table 1. Each electrode had an exposed surface area of 1.08mm^2 and electrode spacing was 3mm center-to-center (this is the same grid used for the *in vitro* experiment in Section 3.1, so we will similarly refer to these as the "small" electrodes). The effective surface area was changed by electrically shorting adjacent electrodes in groups of two and four, thereby mimicking larger surface areas of 2.16mm^2 ("pair" electrodes) and 4.32mm^2 ("quad" electrodes), respectively (Figure 3A). This was done by connecting jumper wires to the paired electrodes at the jack box outside the patient's body (Figure 3B). The jack box combines the individual electrode wires into an integrated cable before connecting to the amplifier. A quick-release connector enabled rapid reconfiguration of the electrode shorting, minimizing disruption to the patient's recording. The jack box and jumper wires were placed in a Faraday cage to minimize electrical interference.

Table 3.1: Patient Information. Age is indicated in years, and all subjects had focal epilepsy. The column for time post-implant indicates when the iEEG recordings were done, with Day 1 defined as the day of implantation. Abbreviations: male (M), female (F), high-density (HD).

Patient	Age at Phase 2	Sex	Etiology	Outcome	Implanted Electrodes	Time post-implant

1	15.4	F	Left frontal focal cortical dysplasia	Seizure-free	Subdural grids: Two 2x4, one 4x8 and one HD 8x8	Day 2, evening
2	11.9	M	Unknown; two seizure foci (right frontal and right temporal)	Seizure-free	Subdural grids: One 8x8, one HD 8x8, one 2x4, two 1x6, one 4x5, one 1x4 Depth electrode: one 1x8	Day 2, evening
3	19	M	Left frontal traumatic brain injury	Seizure-free	Subdural grids: One HD 8x8, one 4x8, two 2x4, and one 2x8	Day 2, evening

We collected 20-minute iEEG recordings for each of three different electrode surface areas (small, pair quad) from a grid in a static brain location while the subjects were sleeping. The sampling rate was 5kHz, and the data were referenced to the common average of the 8x8 grid. The iEEG data were high pass filtered using a zero phase FIR filter at 1Hz and notch filtered at 60Hz, 120Hz, and 180Hz to remove electrical line noise before analysis. All analysis was done using custom code in MATLAB 2018b.

Similar to the *in vitro* study, we compared the results to the theoretical circuit model by generating "simulated pair" electrode signals (consisting of the mathematical average of adjacent pairs of small electrodes) and "simulated quad" electrodes (the mathematical average of four adjacent small electrodes). The averaging of signals was

done on the raw iEEG data and the data were then re-referenced and filtered as described above. We compared the pair and quad electrode recordings to their associated simulated signals.

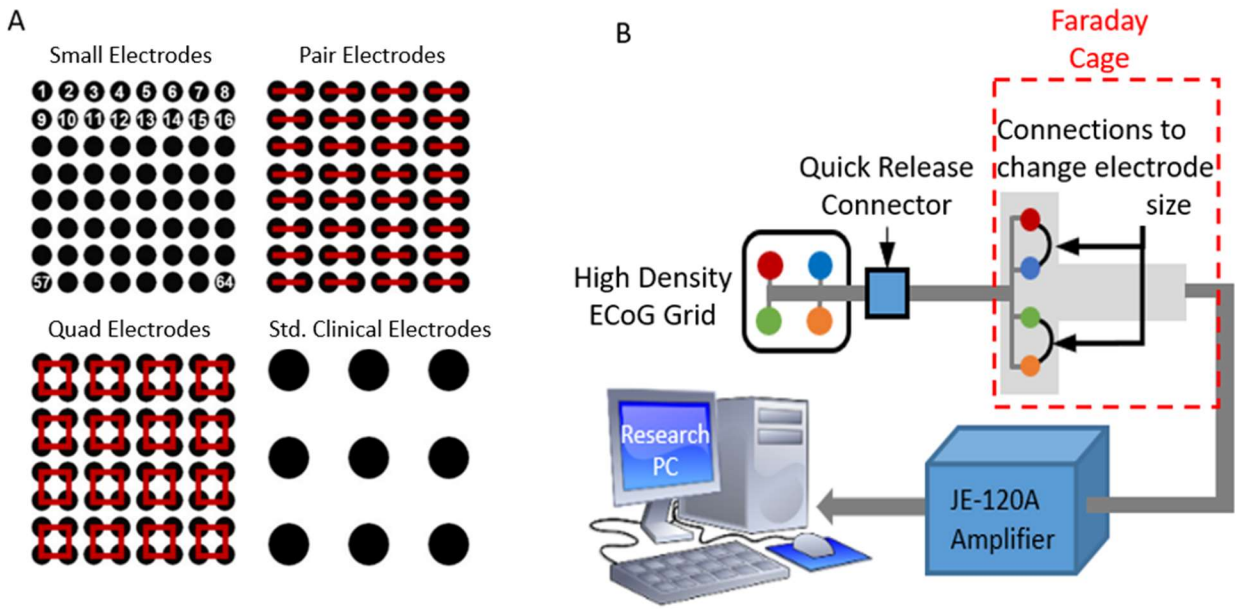

Figure 3.3: (A) Schematic that shows the shorting technique to create pair and quad surface areas, as well as a scale drawing of a standard grid size, for comparison. (B) Experimental setup, showing an example in which a small 2x2 grid (red, blue, green, and orange electrodes) are shorted together in pairs (red-blue and green-orange) using jumper wires.

3.3.2.2 Data analysis

Correlation: To analyze how correlation between EEG signals changes with electrode size, we made two comparisons of correlation values: (1) We compared small and pair electrodes with a vertical inter-electrode distance of 3mm (e.g., correlation between electrodes 1 and 9 compared to the correlation between paired electrodes 1-2 and

9-10), and (2) We compared pair and quad electrodes with a horizontal inter-electrode distance of 6mm (e.g., correlation between electrodes 1-2 and 3-4 compared to the correlation between quad electrodes 1-2-9-10 and 3-4-11-12). The restriction on inter-electrode distance ensured that the comparison of correlation values was done between electrode pairs that had equivalent spacing. For each subject, five one-minute segments of data spaced at least two minutes apart were used for this analysis. The data were band pass filtered into three frequency bands using a zero phase FIR filter: low frequency (1-30Hz), gamma-1 (30-60Hz), and gamma-2 (60-100Hz). In each frequency band, correlation values were calculated in five-second windows for pairs of channels and the correlation values were averaged over all time windows and electrode pairs for a given frequency band and electrode size. For each subject, the samples of size-specific mean correlation values were compared across electrode sizes using a Wilcoxon rank sum test. To assess the baseline distribution of correlation values (under the null hypothesis of zero correlation), correlation between channels was calculated using surrogate data. The surrogate data $x_s(t)$ was obtained by applying a random circular time shift to the original data $x(t)$ as follows:

$$x_s(t) = \begin{cases} x(t + t_r), & t < N - t_r \\ x(t - N + t_r), & t \geq N - t_r \end{cases}$$

Where t_r is a random time point ranging from 1 to N-1.

Amplitude: For each subject, the iEEG data from each of the three electrode configurations was bandpass filtered in the frequency range of 1-100Hz. The bandpass filtered EEG was then divided into 100 segments of five seconds each. For each 5-second segment, the root-mean-square (RMS) value of the amplitude was calculated and then averaged across all time segments. These samples of RMS amplitude values were compared across electrode sizes using a Wilcoxon rank sum test.

Power Spectrum: For every subject, power spectral density from 1-100 Hz was estimated for each of the 100 epochs of five seconds, for each electrode configuration. The following statistical analysis was done independently for each subject. To enable paired comparisons of the power spectra, the signals were grouped based on the quad electrode configuration. For example, small electrodes 1, 2, 9, and 10 were compared to two paired electrodes (1 shorted to 2, and 9 shorted to 10) and one quad electrode (1, 2, 9, and 10 shorted together) (see Figure 3). For each set of four small electrodes, the power spectra were estimated by using the Fourier periodogram which is the data-analogue of the spectrum defined on the fundamental frequencies. Since periodograms are quite noisy, they need to be smoothed in order to obtain a mean-squared consistent estimator (168). In some applications, it is more convenient to use log periodograms (rather than periodograms) because their variance is approximately constant across frequencies. Here, log periodograms were calculated and smoothed across frequencies using a moving average

filter with a span of 5 data points (0.5 Hz). For each set of two pair electrodes, the two log periodograms were averaged and smoothed using a span of 10 data points (1 Hz). For the quad electrodes, the log periodograms were used without averaging and were smoothed using a span of 20 data points (2Hz).

Thus, for each configuration, a set of 1600 log periodograms was obtained (16 signals x 100 epochs). To explore structures, patterns, and features in the sample of periodograms' curves, we followed Ngo et al. (2015) and constructed a functional box plot (FBP) (169), a generalization of the classical pointwise boxplot. For each curve, a modified band depth (MBD) value is computed (170). This indicates whether or not a curve is covered by many pairs of curves in the data. Based on the ranks of MBD values, the FBP provides descriptive statistics, such as the functional median curve, which has the highest MBD value.

Depth-based Permutation Test for the Power Spectrum: Let F, G and L be the distribution of log periodogram populations from three different settings (small, pair and quad electrodes) with $n_1 = n_2 = n_3 = 1600$. We propose a depth-based permutation test for our null hypothesis that the three populations of curves come from the same distribution, i.e., there is no difference in the distributions of the small, pair, and quad electrodes. Let $\{x_1, \dots, x_{n_1}\}$, $\{y_1, \dots, y_{n_2}\}$, and $\{z_1, \dots, z_{n_3}\}$ denote the three samples' curves from distributions F, G and L, respectively.

Suppose that $R(x_1), \ldots, R(x_{n_1})$ are the corresponding ranks of $\{x_1, \ldots, x_{n_1}\}$, measured by comparison to the combined three samples of size $n_1 + n_2 + n_3$. The test statistic is defined as $T = \sum_{i=1}^{n_1} rank[R(x_i)]$, which is the sum of the MBD ranks in distribution F. Under the null hypothesis, T is the sum of n_1 numbers that are evenly distributed between 1 and $n_1 + n_2 + n_3$. If the alternative hypothesis is true, the sample x_i will be more outlying than the other samples, which implies that the depth values will be smaller, with correspondingly smaller ranks. Thus, a small value of T provides strong evidence to reject the null hypothesis. Since it is a challenging task to obtain the distribution of T under the null hypothesis in a case of three samples, we then carry out a permutation test to compute the p-values, which is as follows:

1. Permute electrode configuration labels (small, pair and quad) among the samples in the combined set $\{x_1, \ldots, x_{n_1}\}$ U $\{y_1, \ldots, y_{n_2}\}$ U $\{z_1, \ldots, z_{n_3}\}$ and denote the resulting samples of the jth permutation to be $\{x'_{j1}, \ldots, x'_{jn_1}\}$, $\{y'_{j1}, \ldots, y'_{jn_2}\}$, and $\{z'_{j1}, \ldots, z'_{jn_3}\}$ for $j = 1, \ldots, J$.
2. For each permutation, we compute the test statistic $T'_j = \sum_{i=1}^{n_1} rank\left[R(x'_{ji})\right]$
3. The p-value is approximated by $\sum_{j=1}^{J} I\left[T'_j > T_{obs}\right]/J$ where T_{obs} is the observed value of T based on the original combined samples $\{x_1, \ldots, x_{n_1}\}$ U $\{y_1, \ldots, y_{n_2}\}$ U $\{z_1, \ldots, z_{n_3}\}$, and I is the indicator function.

Because the different electrode configurations were recorded at different times, we also tested whether the power spectra were stable over time. For each configuration, we compared the power spectra in the first five minutes of the recording to those in the last five minutes, using five equally spaced 25-second intervals for each case. Depth based permutation testing was done as described above on the two sets of five curves in each scheme.

3.3.2.3 Analysis of Interictal Spikes

We also wanted to characterize the impact of electrode size on the morphology of transient electrographic events. Because the study subjects had refractory epilepsy, we focused on interictal epileptiform discharges, i.e., interictal spikes. For this analysis, 20-minute segments of data were used, each one clipped from the long-term recording while the patient was sleeping, between midnight and 12:30am. Interictal spikes were manually marked in the iEEG data in the small electrode configuration for each subject under the supervision of a board-certified epilepsy specialist (DS). We then simulated each spike in the pair and quad electrode configurations by mathematically averaging the corresponding small electrode data. We defined the SNR of each spike as the signal to background amplitude ratio. The amplitude of the spike was measured as the difference between the minimum and maximum voltages recorded over the duration of the spike. To calculate the background amplitude, a one-second interval around the spike, not containing the

spike, was considered. The signal in this window was rectified, and the average of the rectified signal was defined as the baseline amplitude. The SNRs were compared across the three electrode configurations and each spike was classified into one of three types: type S, in which a small electrode had the highest SNR, type P, in which a pair electrode had the highest SNR, and type Q, in which a quad electrode had the highest SNR. The spatial spread, defined as the combined area of the electrodes in which the SNR of the signal exceeded 1.5 during the time of the spike, was also calculated for each spike.

3.4 Results

3.4.1 In Vitro Study: Physical shorting of electrodes mimics larger electrode sizes

The *in vitro* experimental results are shown in Figure 4. For the small, medium, and large, as well as the pair and quad electrodes, the measured signal maintained the original sinusoidal shape and frequency of stimulation for all stimuli. The RMS amplitudes varied according to the electric field created by the bipolar stimulation (Figure 4). For all electrode configurations, the highest amplitude was observed at the boundary of the grid, and the amplitude decreased for the inner electrodes. Amplitude also decreased as the vertical distance from the stimulating electrodes increased. These results are consistent with the electric field lines in Figure 2B. We found that the amplitudes were highest for

the smallest electrodes and decreased with an increase in electrode size, and this effect was also seen in the shorted electrodes.

The RMS amplitudes of the signals from the pair and medium electrodes were not statistically different from one other (Wilcoxon rank sum test, p-value>0.5, Figures 4B &4 D). This was also true in the case of quad and large electrodes (Figures 4C & 4E). These results indicate that shorting electrodes together mimics larger surface areas, consistent with our hypothesis. The lack of an exact correspondence between the amplitude values for different electrode configurations can be attributed to the limitations of the experimental setting, including slight variations in the positioning of the electrode grids and the fact that the adjacent shorted electrodes are not contiguous. For each electrode configuration, we changed the stimulation frequency from 10 to 70 Hz and found no difference in RMS values.

For both pair and quad recordings, the RMS values from the mathematically averaged signals were not significantly different from the corresponding RMS values obtained by physically shorting the electrodes (Fig 4F compared to Figure 4B, and Figure 4G compared to Figure 4C; Wilcoxon rank sum test, p-value>0.5).

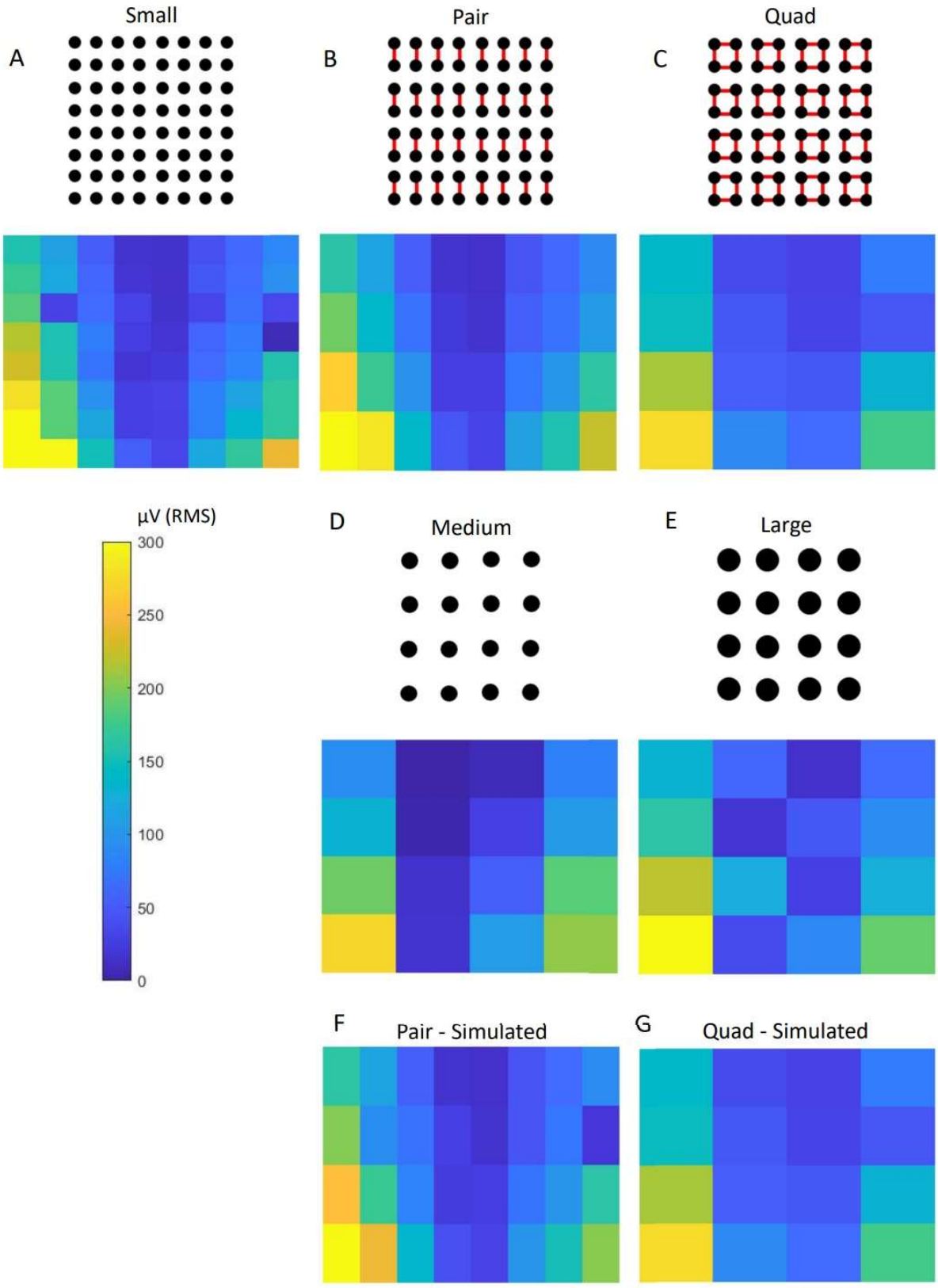
A
Small
B
Pair
C
Quad
µV (RMS)
300
250
200
150
100
50
0
D
Medium
E
Large
F
Pair - Simulated
G
Quad - Simulated

Figure 3.4: RMS amplitude values measured using (A) small electrodes, (B) pair electrodes via physical shorting, (C) quad electrodes via physical shorting, (D) medium electrodes, in which each electrode has a surface area equivalent to a pair electrode, and (E) large electrodes, in which each electrode has a surface area equivalent to a quad electrode. RMS amplitude values measured using (F) simulated pair and (G) simulated quad electrodes, which were obtained by mathematically averaging data from small electrodes. For each electrode, the RMS amplitude was calculated using the entire 30-second recording.

3.4.2 In Vivo Study

Data were collected from three human subjects (1 female, 2 male) aged 15.4, 11.9, and 19 years. Board-certified epilepsy specialists verified that the use of the high-density subdural grid did not impede their ability to clinically interpret the iEEG signals or identify the electrodes where seizure activity first began. In one subject, functional mapping was also successfully performed using the high-density subdural grid (171).

3.4.2.1 EEG Correlation does not depend on electrode size

In the human iEEG recordings, we calculated the correlation between EEG signals from electrodes at a fixed distance. We found no statistically significant differences in correlation when comparing small and pair electrodes or pair and quad electrodes, in any frequency band or subject (Figure 5 and Supplementary Figures 1&2). However, we did note a trend of increasing correlation with increasing electrode size. The correlation values in all three frequency bands in all three subjects were significantly higher than the baseline correlation values calculated using the time shifted surrogate data (range: -0.02 to 0.01).

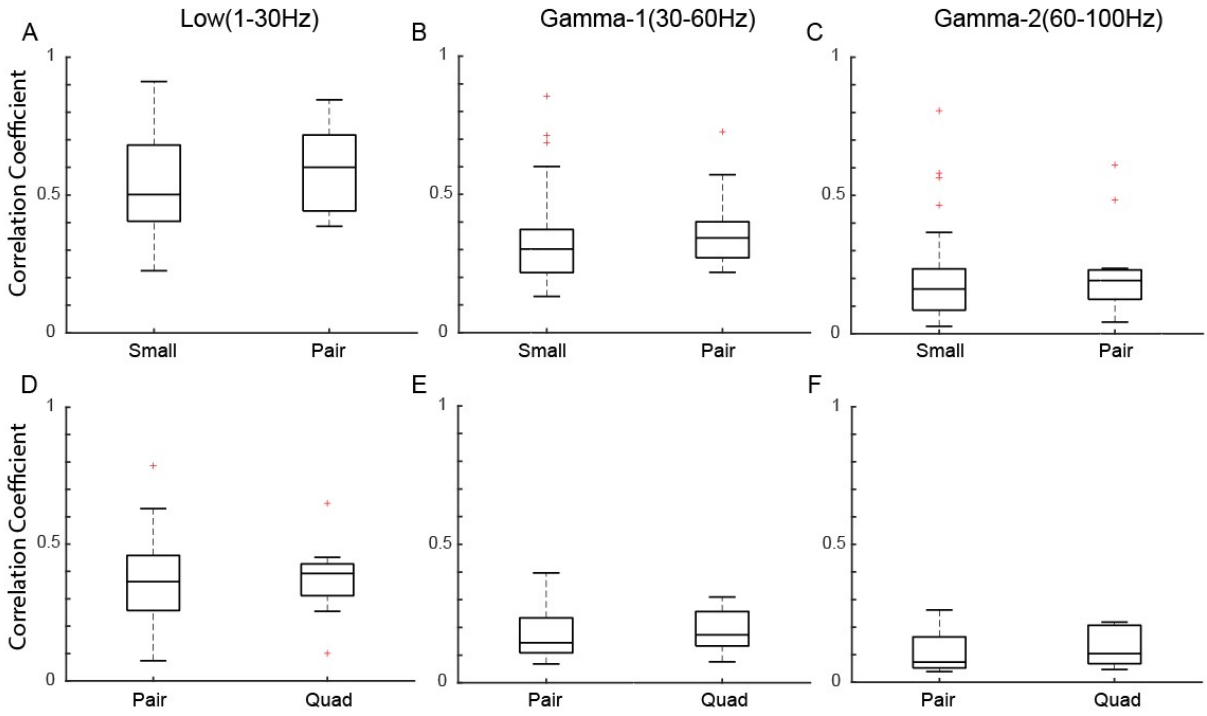

Figure 3.5: (A-C) Boxplots of EEG correlation values for electrodes at a fixed distance for small and pair electrode sizes (n=32 for small and n= 16 for pair). (D-F) Boxplots of EEG correlation values for electrodes at a fixed distance for pair and quad electrode sizes (n=16 for pair and n= 8 for quad). The box plots are generated from data points corresponding to the average correlation across all five-second time windows for the electrode pairs from one subject. Results are shown for the low (left), Gamma-1 (middle), and Gamma-2 frequency bands (right). Data are shown for a single representative subject; data for the other two subjects can be found in Supplementary Figures 1 and 2.

3.4.2.2 EEG amplitude and power decrease with increasing electrode size

The iEEG RMS amplitude was highest for the small electrodes, and it decreased as electrode size increased (Figure 6A). The pair and quad electrode sizes were created via physical shorting of small electrodes. The differences were statistically significant for all three electrode sizes across all three subjects.

The power spectra for the three electrode sizes overlapped in the low frequencies, based on the 50% central regions of the curves, but they were distinguishable for higher frequencies (Figure 6B). Overall, the median periodogram curves were higher for small electrodes, which indicates that the iEEG power is higher for small electrodes compared to larger ones. Among the 48 sets of channels analyzed (16 from each subject), 39 showed a significant difference in the power spectra between the three different electrode sizes using the depth-based permutation test ($p<0.05$).

Note that there is significant spatial variation of the iEEG amplitude across the subdural grid (Figure 6C), possibly related to differences between tissue inside and outside the seizure onset zone. In all three subjects, the clinical team localized the seizure onset to an electrode on the high-density subdural grid. However, for each patient, the spatial distribution of amplitudes was consistent across electrode sizes, with amplitude generally decreasing as electrode size increased. As in the *in vitro* experiment, the amplitude in the

larger electrodes appeared to be consistent with the average of the corresponding small electrodes (Figure 6C).

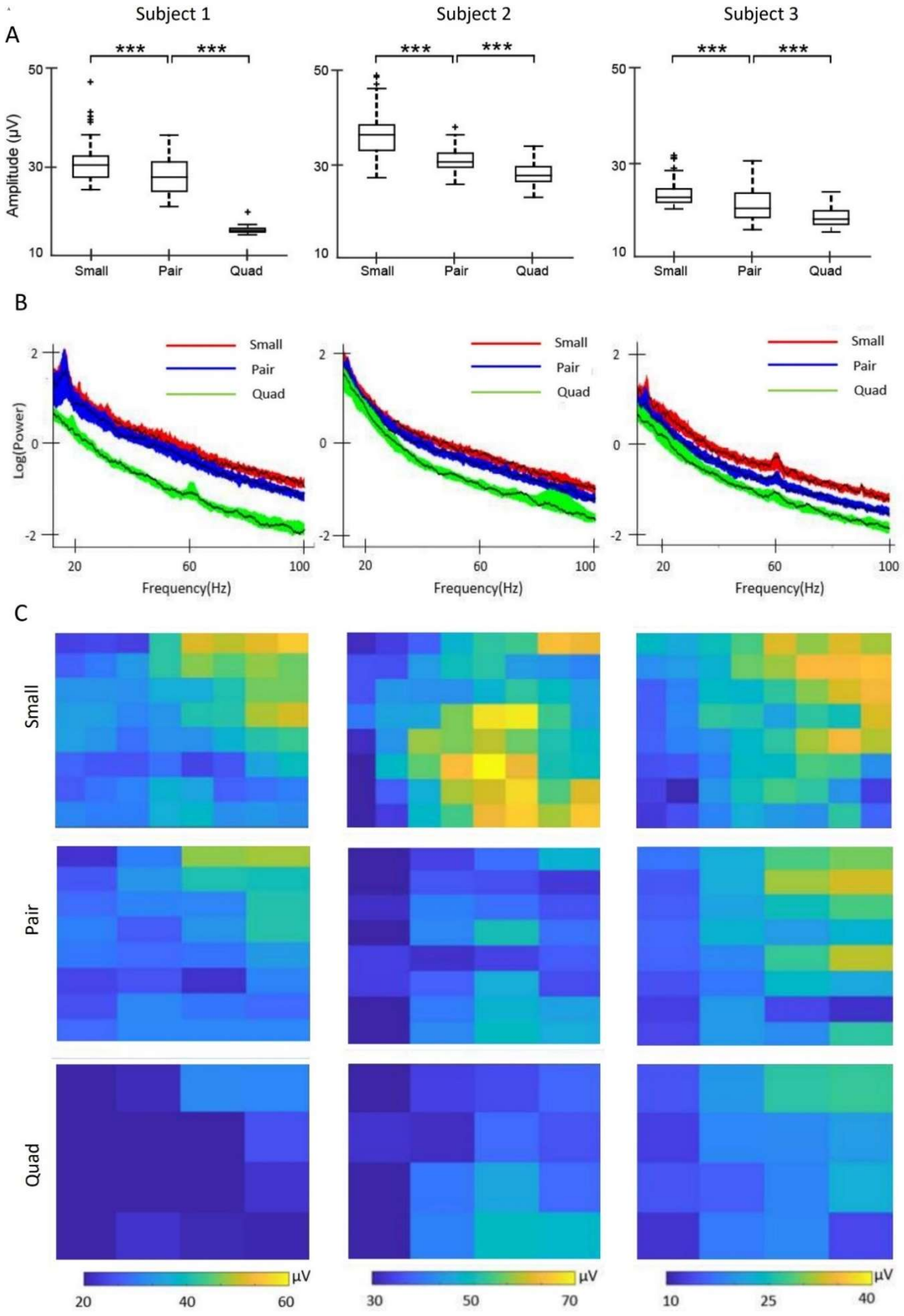
A
Subject 1
Subject 2
Subject 3
***
***
Amplitude (μV)
50
30
10
Small
Pair
Quad
B
Small
Pair
Quad
Log(Power)
2
0
-2
20
60
100
Frequency(Hz)
C
Small
Pair
Quad
μV
20
40
60
30
50
70
10
25
40

*Figure 3.6: (A) Box plots of iEEG RMS amplitude in the 1-100 Hz frequency band measured using electrodes of three different sizes in the three subjects. Data from each subject are shown in a single column, across all subfigures. (B) Functional median curves for the power spectra in all three subjects. The black lines show the median curves, and the colored areas denote the 50% central region. (C) Heat maps of average RMS amplitude values for all electrodes in each subject measured using small, pair, and quad electrodes (physically shorted) in the 1-100Hz band. For example, the results for the small electrodes show values in an 8x8 grid, with each colored square representing one electrode. For each electrode, the RMS amplitude was calculated for 5-second intervals and then those values were averaged. Each column of subfigures corresponds to the results for one subject and the subfigures in each row correspond to small, pair and quad electrodes. *indicates p-values< 0.05, ** indicates p<0.01, *** indicates p<0.001. All p-values are corrected for multiple comparisons using the Bonferroni method.*

3.4.2.3 Interictal spike morphology depends on the size and location of the neural generator, relative to electrode size

To quantify the impact of electrode size on interictal spike morphology, we measured the spike SNR as a function of electrode size. We were unable to do direct event-wise comparisons using the physically shorted electrodes because the data for each electrode size were recorded at different times. Therefore, we used simulated spikes to estimate the change in SNR as electrode size varied. We first marked a total of 500 spikes, using the data from the small electrodes from all three subjects. For each spike, we then calculated simulated spikes in pair and quad electrodes, via mathematical averaging of the associated small electrode iEEG.

Two examples of simulated spikes demonstrate why the smallest electrodes are not always associated with the highest SNR. In the first case (Figure 7A), the spike is clearly localized to a single electrode. Therefore, averaging reduces the SNR of the spike, and the biggest SNR is observed in the smallest electrode. In the second case (Figure 7B), the spike is more widespread, and averaging increases the amplitude relative to the background. Consequently, the largest SNR is observed for the pair electrode.

Across all visually-marked spikes, 61% had the highest SNR in the small electrodes, 29% had the highest SNR in the simulated pair electrodes, and 10% had the highest SNR in the simulated quad electrodes (Figure 7C). When measuring with small electrodes, the spikes were seen in a larger number of channels, but the cortical surface area of the spikes remained approximately constant across electrode sizes (Figure 7D, $p>0.1$).

Anecdotally, when visually comparing the interictal spikes from the three electrode sizes, obtained via physical shorting and recorded at independent time points, we found examples that were consistent with these results. Figure 7E shows an example of prominent spikes recorded by small electrodes that exhibited lower amplitude when the same brain location was later recorded with physically-shorted pair electrodes, analogous to the simulation results in Figure 7A. A second example shows a case where the spikes had low amplitude when recorded with small electrodes, but they became more visually

prominent when the same brain region was later recorded with physically-shorted pair electrodes (Figure 7F), analogous to the simulated data in Figure 7B.

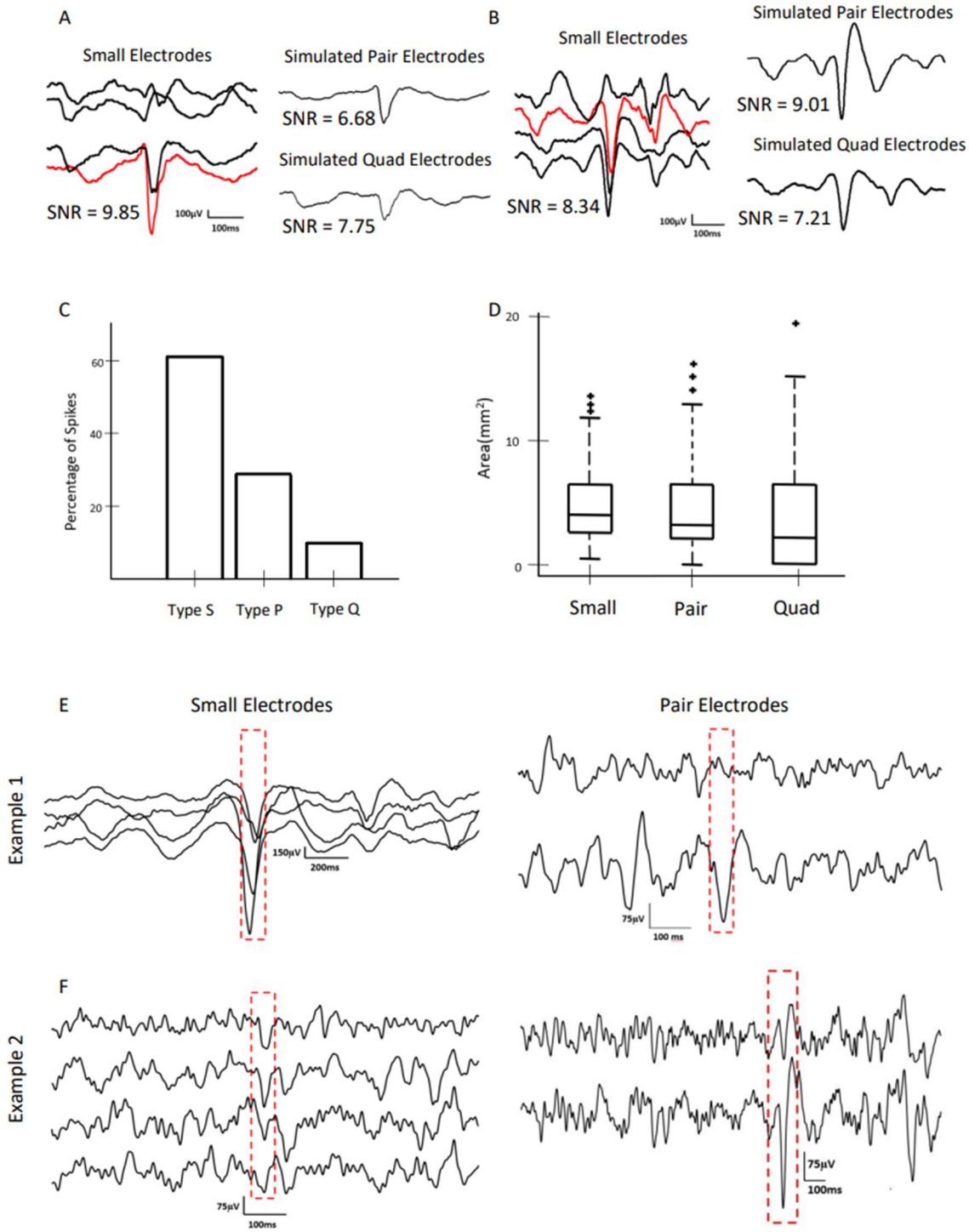

Figure 3.7: (A) Simulation results showing an example of a type S interictal spike, in which the SNR is high for a small electrode and lower for a pair electrode simulated via mathematical averaging. (B) Simulation results showing an example of a Type P spike, in which the SNR for simulated pair electrodes is higher than for small electrodes. (C) Bar graph showing the percentages of Type S, Type P, and Type Q spikes for all three subjects. Data for pair and quad electrodes were obtained via mathematical averaging of small electrodes. (D) Spatial spread of spikes for different electrode sizes across all three subjects. Data for pair and quad electrodes were obtained via mathematical averaging of small electrodes. (E) Example of interictal spikes captured via physical shorting of electrodes, in which a high SNR spike is visible in the small electrodes (left) and a low SNR spike is seen when the same brain region is later recorded using pair electrodes (right). (F) A second example of an interictal spike captured via physical shorting of electrodes. Here, a spike with low SNR is visible in the small electrodes (left); when physical shorting was later used to record from pair electrodes, larger SNR spikes were noted in the same set of channels (right).

3.5 Discussion

Through this study, we have introduced a method for dynamic selection of the size of iEEG electrodes after implantation in the human brain. We first presented an electrical circuit model, then performed an *in vitro* validation of that model, showing that there were no significant differences between physically shorted electrodes and larger electrodes with equivalent surface areas. The signals from physically shorted electrodes were also consistent with simulated signals obtained by mathematically averaging the signals from the small electrodes. In human subjects, we found that increasing electrode size leads to lower iEEG power and amplitude, but no difference in correlation between channel pairs.

The morphology of interictal spikes was also impacted by electrode size and depended on the size and location of the neural generator relative to the electrodes.

The development of this novel recording technique is significant because it will enable direct tests of the impact of electrode size on transient electrographic events, such as epileptiform discharges and HFOs, as well as seizure localization and functional mapping. This may impact the design and manufacture of FDA-approved intracranial electrodes for human use, as well as clinical procedures for patient evaluation. Moreover, our data suggest that mathematical averaging of iEEG electrodes is consistent with physical shorting of the same electrodes; if this hypothesis is further validated, such studies could be done using a single high-density grid and simple mathematical averaging, which would greatly increase the flexibility and applicability of this technique.

Our results shed light on hypotheses put forward in previous literature. In an *in vivo* study of rat somatosensory cortex, the amplitudes of sensory evoked potentials (SEPs) recorded using small electrodes were higher than those recorded using larger electrodes (172). Our results in Figure 6 show the same trend. In our simulations of interictal spikes, we estimated that a majority of spikes would have the highest SNR when recorded with small electrodes, but approximately 40% of spikes had higher SNR values when simulated in pair and quad recordings, using mathematical averaging. Anderson et al. (2010) posited that using larger electrodes for recording action potentials of neurons

decreases the SNR. Assuming that the spatial extent of the action potential is small relative to the electrode size, this is consistent with our observations of interictal spikes (Figure 7)(154). While single neuron spikes occur on a much smaller spatial scale than interictal epileptiform discharges, the two cases share conceptual similarities. Lastly, in a study that measured correlation using both micro-ECoG and standard ECoG electrodes, the larger electrodes exhibited higher correlation (158). Wang et al. also reported higher degrees of dependence between larger electrodes (157). Although our results show a trend of an increase in correlation with electrode size (Figure 5), this difference was not found to be significant for the sizes compared. This could be because our analysis was done at a fixed inter-electrode distance, while the inter-electrode distance varied with electrode size in the prior studies.

There are some limitations to this study. The electrodes in the ECoG grids had a center-to-center distance of 3mm, so the adjacent shorted electrodes were not contiguous. That is, there was some area of tissue between shorted electrodes that was not in contact with them, which is a deviation from the assumption of a single, continuous electrode. Using tripolar concentric ring electrodes (173) or decreasing the interelectrode distance in the grid would help alleviate this limitation. However, because this study was done on human subjects, we were limited to the use of FDA approved electrodes. Another limitation was that the recordings from electrodes of different sizes were done sequentially

and, therefore, were obtained at different times. We repeated these measurements to verify that our findings remained robust and were stable over time. In particular, we found no significant difference in the value of the power spectrum when comparing data spaced 10 minutes apart, for any electrode size. Additionally, the data in this study were obtained from patients with epilepsy, and this disease is known to alter various features of the iEEG data. Because our aim was to study the effects of electrode size on iEEG, irrespective of the origin of the activity, we believe this did not significantly impact our results. Moreover, all comparisons were made using data recorded from the same region of brain tissue; therefore, the presence or absence of epileptogenic activity should impact all conditions equally.

Future work in this field may benefit from the use of modeling techniques like Finite Element Modeling (FEM). FEM based methods have been used to numerically solve the EEG forward problem accurately, that is, to determine the voltages at the surface of the brain given the location of deep sources. This is done by incorporating complex geometries and electrical properties of the brain into the model (174). FEM could be applied to our study to exactly simulate electrodes of different sizes having similar geometries and spacing between them. This could address the inconsistency between our simple mathematical averaging approach and the non-contiguous area of the larger electrodes in this study. Thus, an FEM-based approach could provide a more accurate

mathematical model of the measured electrical activity, as a function of electrode geometry and spacing, given a set of neural sources.

This study is the first to present a method to record intracranial EEG from a static section of neural tissue using electrodes of different effective sizes. This technique provides an avenue for multi-scale analysis of neurological phenomena recorded from a single location in the brain. The methods used here could also enable dynamic selection of optimal electrode sizes for detection of neurological events like seizures, HFOs, and interictal spikes, as well as recordings used by neural prostheses or BCIs. This is especially relevant in a clinical setting where the precise locations of these events are unknown prior to surgery and are highly variable across patients. Clinicians rely on visual analysis of the iEEG, and electrographic events that are barely visible in data from a particular electrode size could be more accurately studied when measured with a larger or smaller electrode. In applications like neural prostheses and BCI where the quality of the signals is paramount, our methods can be used to maximize SNR while requiring only a

CHAPTER 4

RATE AND AMPLITUDE OF HIGH FREQUENCY OSCILLATIONS ARE INVERSELY CORRELATED TO SURFACE AREA OF SUBDURAL ELECTRODES

4.1 Introduction

High-frequency oscillations (HFOs) are transient bursts of electrophysiological activity with peak frequencies greater than 80 Hz, associated with both normal physiological processes and epilepsy (175). They have been studied extensively in the past two decades as prognostic biomarkers of surgical outcome in patients with with epilepsy (59). The first HFOs detected in human intracranial EEG (iEEG) were recorded at very small spatial scales, using microwires with diameters in the 40 micron range (30, 66). HFOs were subsequently detected in recordings from much larger clinical depth electrodes, approximately $1mm^2$ in area (176). Today, they are recorded using electrodes with contact areas that range from $0.003mm^2$ to $20mm^2$, with a myriad of different geometries (49, 50). There is also increasing evidence that this high-frequency electrophysiological activity is measurable using non-invasive scalp EEG electrodes (177). However, all such events are singularly referred to as "HFOs," regardless of the spatial scale at which they are measured. It is unknown if the events detected at different spatial scales represent the same neural phenomenon or have equivalent clinical relevance (28).

This variability in the size of recording electrodes used for HFO detection is a potential confounding factor in current studies. It has been shown that HFOs occur more frequently in the seizure onset zone (SOZ) (91, 109) and are a promising tool for surgical planning, as the removal of HFO-generating brain regions is associated with positive long-term outcomes (28, 43, 47, 114). However, despite strong associations at the group level, HFOs have not been shown to be reliable predictors of outcome for individual patients (47, 114). One reason for this discrepancy could be because results from a wide range of electrode contact areas have been equated with one another, often within the same patient or research study. If electrode size impacts the measurement of HFOs, e.g., if large electrodes over- or underestimate the HFO rate, it could significantly impact the study results.

A small number of studies have examined the effect of electrode size on HFO measurement, and they have offered conflicting results. Worrell et. al reported that microwires (40μm diameter) recorded more fast ripples (250-500Hz) than macro-electrodes (2.3 mm diameter)(37). Another study found a similar trend, with HD-ECoG electrodes of 2.3mm diameter recording more fast ripples than larger ECoG electrodes of 5mm diameter(161). However, Chatillon et. al. reported no such difference in the detectability of fast ripples between electrodes with diameters of 0.2mm and 0.8mm(50). For ripples (80-250Hz), small differences in rate (number per minute) were reported for sizes ranging

from 0.02 to 0.09 mm^2, but were deemed to be not clinically relevant (50, 51). In a study using 2.3mm and 5mm diameter intra-operative ECoG, it was suggested that fast ripple rates delineated the SOZ more accurately when electrodes with smaller contact areas and inter-electrode distances were used (161). Two studies reported differences in the average peak frequency of ripples for different electrode sizes. Worrell et. al. 2008 reported that the average peak frequencies were higher for microelectrodes than standard clinical depth electrodes (37). Blanco et. al. 2011 found no such frequency difference for subdural grids, but reported the same difference for depth electrodes when compared to microelectrodes (109). Modur et. al. 2011 reported no difference in characteristics of HFOs recorded using subdural electrodes (1.1mm in diameter) compared to depth electrodes (2.3mm in diameter) (178).

However, in these studies, the electrodes of different sizes were adjacent to one another, in spatially distinct brain regions, or in different subjects altogether; therefore, the comparisons were not between electrodes in the same region of neural tissue in the same patient. Because characteristics of HFOs vary significantly between subjects and brain regions (28, 90), any variations found by these studies cannot be solely attributed to the difference in electrode size. Further, no current methods enable separation of the effects of electrode size, regional variation, and differences in epileptiform activity. This impedes a direct comparison of HFO characteristics between different electrode sizes.

To address this, we measured HFOs using three different sizes of subdural iEEG electrodes implanted in the human brain. Unlike previous studies, we recorded from the exact same region of brain tissue using all three electrode sizes; this was accomplished using a technique developed by our group (2). We then directly compared the HFO characteristics of rate, amplitude, duration and peak frequency when measured with electrodes of different effective surface areas. We also calculated the rate of HFOs per unit area of electrode to account for the fact that larger electrodes measure from a larger portion of cortical tissue. Recording iEEG from the same tissue location for all electrode sizes is paramount to calculating this metric, and this is the first study to do so.

4.2 Methods

4.2.1 Patients and Data

This study was approved by the Institutional Review Board of the Children's Hospital of Orange County. We recruited eight pediatric subjects with medically intractable epilepsy and focal seizures that were undergoing pre-surgical invasive monitoring. Each subject had a high-density (HD) 8x8 subdural grid of intracranial EEG electrodes (Ad-Tech FG64C-MP03X-000) implanted, in addition to any other standard intracranial electrodes deemed necessary by the clinical team. However, in this study, we analyzed only the data from the HD grid. In five subjects, the HD grid was in the clinically

determined SOZ. Electrodes in the HD grid had a surface area of 1.08mm^2 and inter-electrode distance of 3mm. This is approximately one fourth of the size of standard subdural grids which typically have 4 mm^2 electrode surface areas and 10 mm spacing.

Table 4.1: Patient Information. Age is indicated in years, and all subjects had focal epilepsy. The column for time post-implant indicates when the iEEG recordings were done, with Day 1 defined as the day of implantation. Abbreviations: male (M), female (F), high-density (HD).

Pt. No.	Age at Phase 2	Sex	Etiology	Outcome	Implanted Electrodes	Time post implant	SOZ in HD grid	Total duration of iEEG analyzed
1	15.4	F	Left frontal focal cortical dysplasia	Seizure-free	Subdural grids: Two 2x4, one 4x8, and one HD 8x8	Day 2, evening	39, 47,55, 56, 62, 64	59 mins
2	11.9	M	Unknown; two seizure foci (right frontal and right temporal)	Seizure-free	Subdural grids: One 8x8, one HD 8x8, one 2x4, two 1x6, one 4x5, one 1x4 Depth electrode: one 1x8	Day 2, evening	2, 10,18, 25, 26, 33, 34	53 mins

3	19	M	Left frontal traumatic brain injury	Seizure-free	Subdural grids: One HD 8x8, one 4x8, two 2x4, and one 2x8	Day 2, evening	27,28, 36,37, 43,44	60 mins
4	16.7	F	Perinatal stroke	Seizure-free	Subdural grids: One 8x8, one HD 8x8, two 4x8, one 2x6, one 1x6 and two 1x4	Day 3, evening	Not in HD grid	60 mins
5	6.8	F	Occult structural lesion	Seizure-free	Subdural grids: One 8x8, one HD 8x8, two 4x8 and two 2x6	Day 3, evening	No seizures captured	60 mins
6	1	M	Large right frontal cortical dysplasia	Seizure-free	Subdural grids: One 8x8, one HD 8x8, two 1x6 and one 1x4	Day 3, evening	1- 64	60 mins
7	7.6	M	Large right posterior cortical malformation	Seizure-free	Subdural grids: One 8x8, one HD 8x8, one 2x6, one 2x5, two 1x6 and one 1x4	Day 3, evening	27-30, 34-38, 43-47, 51-55, 58-62	60 mins
8	15.6	F	Traumatic left fronto-temporal parietal	Seizure-free	Subdural grids: One 8x8, one HD 8x8, one 2x4,	Day 3, evening	Not in HD grid	60 mins

	hemorrhag e	two 1x6, and one 1x4

After implantation, we modified the recording setup for the HD grid electrodes to create electrodes with three different surface areas as described in (2). Briefly, this was done by electrically shorting adjacent electrodes in groups of two or four using jumper wires at the junction with the amplifier, outside the head (Figure 1). The shorting effectively averages the electrical activity of the tissue under the electrodes (143, 145), as would be reported by a larger electrode in the same location, thus mimicking larger surface areas of 2.16mm^2 and 4.32mm^2. We recorded approximately 20 minutes of iEEG for each of the three different electrode surface areas (which we will refer to as "small", "pair" and "quad" electrodes) while the subjects were sleeping. Whenever possible, the experiment was conducted in the evening on the day after implantation (Table 1), and the data were recorded at least two hours away from seizures. Note that the effective surface area of a "quad" electrode is roughly comparable to that of a standard clinical macro-electrode.

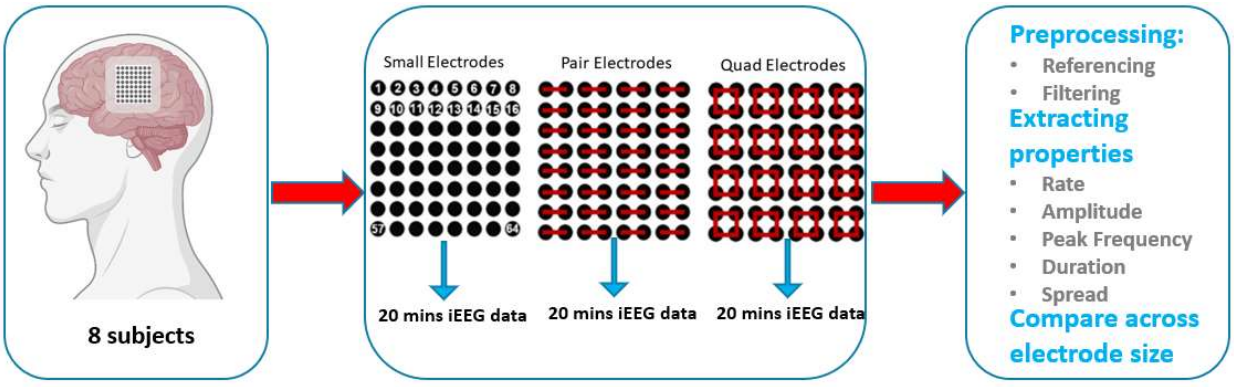

Figure 4.1: Increasing surface area via shorting of electrodes

4.2.2 Preprocessing and HFO detection

The recorded iEEG data were re-referenced to the common average of the HD grid. These data were then bandpass filtered in the ripple (R, 80-250Hz) and fast ripple (FR, 250-500Hz) frequency bands and notch filtered at the odd harmonics of 60Hz to remove line noise. Then, the data were divided into one-minute segments for automatic HFO detection using a previously validated algorithm based on the RMS amplitude of the filtered signal (72). In short, the RMS amplitude of the iEEG was calculated in 3 ms sliding windows, and segments in which the RMS amplitude exceeded a threshold for a minimum duration of 6ms were marked as events of interest. Events with at least six peaks crossing a second threshold were defined to be HFOs. Both detection thresholds in the algorithm were set to three standard deviations above the mean of the rectified, filtered signal. False positive detections were rejected using the methods outlined in Gliske et. al. 2016 for removing artifacts present in the common average reference and those caused by fast transients or DC shifts (79).

4.2.3 Calculation of HFO properties

The average rate of HFOs (number per minute) was calculated for each channel in the ripple and fast ripple bands separately. In each subject, we thus obtained 64, 32 and

16 values of HFO rates for the small, pair, and quad electrode configurations, respectively. These HFO rates were then compared within each subject using a Wilcoxon rank sum test, separately for frequency band (R and FR). Then, because each electrode size measured from a different amount of tissue, we did a second comparison where we normalized HFO rate for electrode size by calculating the global rate per unit area of tissue. The global rate was defined as the total number of unique events over the entire grid (counting any overlapping events only once), divided by the total duration of data in minutes. The the global rate per area was defined as the ratio of the global rate to the summed area of all 64 electrodes. This metric was used to compare the three electrode sizes across all subjects using the Wilcoxon rank sum test.

We also assessed the impact of electrode size on three other HFO characteristics: amplitude, duration, and peak frequency. The amplitude of each HFO was estimated as the average value of the upper Hilbert envelope of the signal over the duration of the event. The peak frequency of an HFO was defined as the frequency for which the magnitude of the Fourier transform of the whitened signal (74) was maximal. The Wilcoxon rank sum test was used to test the dependence of HFO amplitude, duration, and peak frequency on electrode size.

Finally, we measured the spatial extent of each HFO using the "spread" (S), defined as the number of electrodes in which an HFO was simultaneously observed. HFOs

that were only detected in one electrode and did not overlap in time with a detected HFO in any other electrode had S = 1, while events that were observed in more than one electrode had S ≥ 2. We calculated the spread for single, pair, and quad electrodes and compared their distributions in the ripple and fast ripple bands.

4.2.4 Simulating larger electrodes

The basis for the electrical shorting technique is the theory that each electrode reports an average of the electrical activity of the underlying tissue. If true, this implies that measurements of the pair and quad electrodes can be simulated by mathematically averaging measurements from the small electrodes. To compare such post-hoc averaging of data to recordings obtained via physical shorting of electrodes, we mathematically calculated "simulated" signals for the pair and quad electrodes. To do this, we averaged the re-referenced iEEG data from the small electrodes across the channels that formed each corresponding pair or quad electrode. HFOs were then detected in the simulated pair and quad signals, and the HFO rates and morphological features were computed using the same techniques as above.

4.3 Results

4.3.1 HFO rate decreased with an increase in electrode size in all subjects

Figure 2 shows heatmaps of fast ripple rates for all eight subjects across all three electrode sizes. In general, the warmest colors, denoting the highest rates, are seen in the small electrodes. For some subjects, regions of high rate can be easily localized using any electrode size (e.g., Figures 2C and 2E). In others, they can only be delineated using the smaller electrodes (e.g., Figure 2 D). The average rates of FRs were significantly higher ($p<0.05$) in the pair electrodes compared to quad electrodes in six subjects (Figure 2). In five subjects, the average FR rate in the small electrodes was also significantly higher ($p<0.05$) than pair electrodes. In the ripple band, the average HFO rate was significantly higher in small electrodes compared to pair electrodes in all subjects ($p<0.05$) and in pair electrodes compared to quad electrodes ($p<0.05$) in seven subjects.

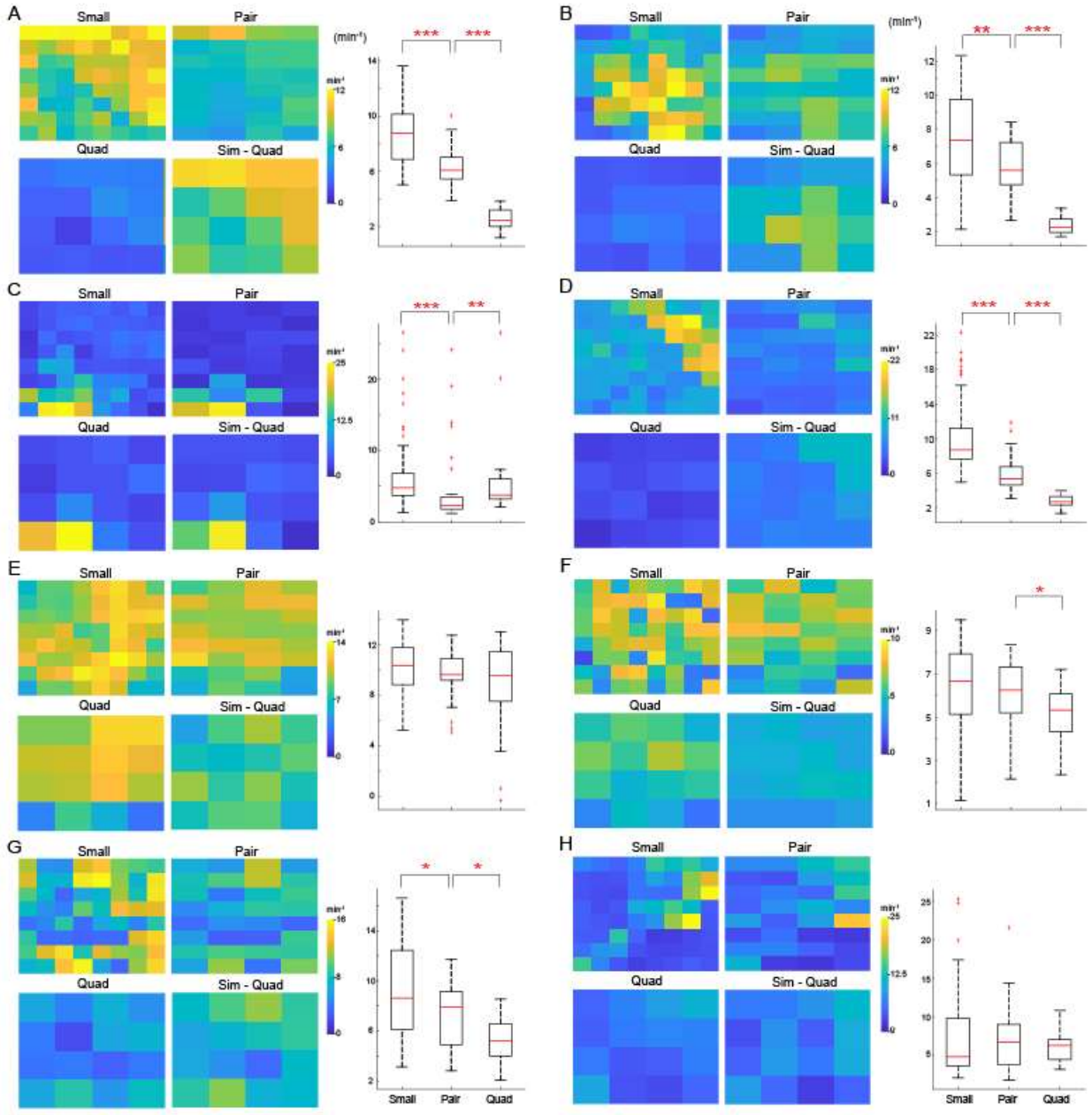

*Figure 4.2: Fast ripple rates across the HD subdural grid for Subject 1 (subfigure A) through Subject 8 (subfigure H). Heatmaps of fast ripple rates for small, pair, quad, and simulated quad electrodes, are shown on the left of each subfigure. The right side of each subfigure shows boxplots comparing fast ripple rates across all electrodes for the three electrode sizes. * indicates p<0.05, ** indicates p<0.01 and ** indicates p<0.001*

4.3.2 Global rate per area decreased with increase in electrode size

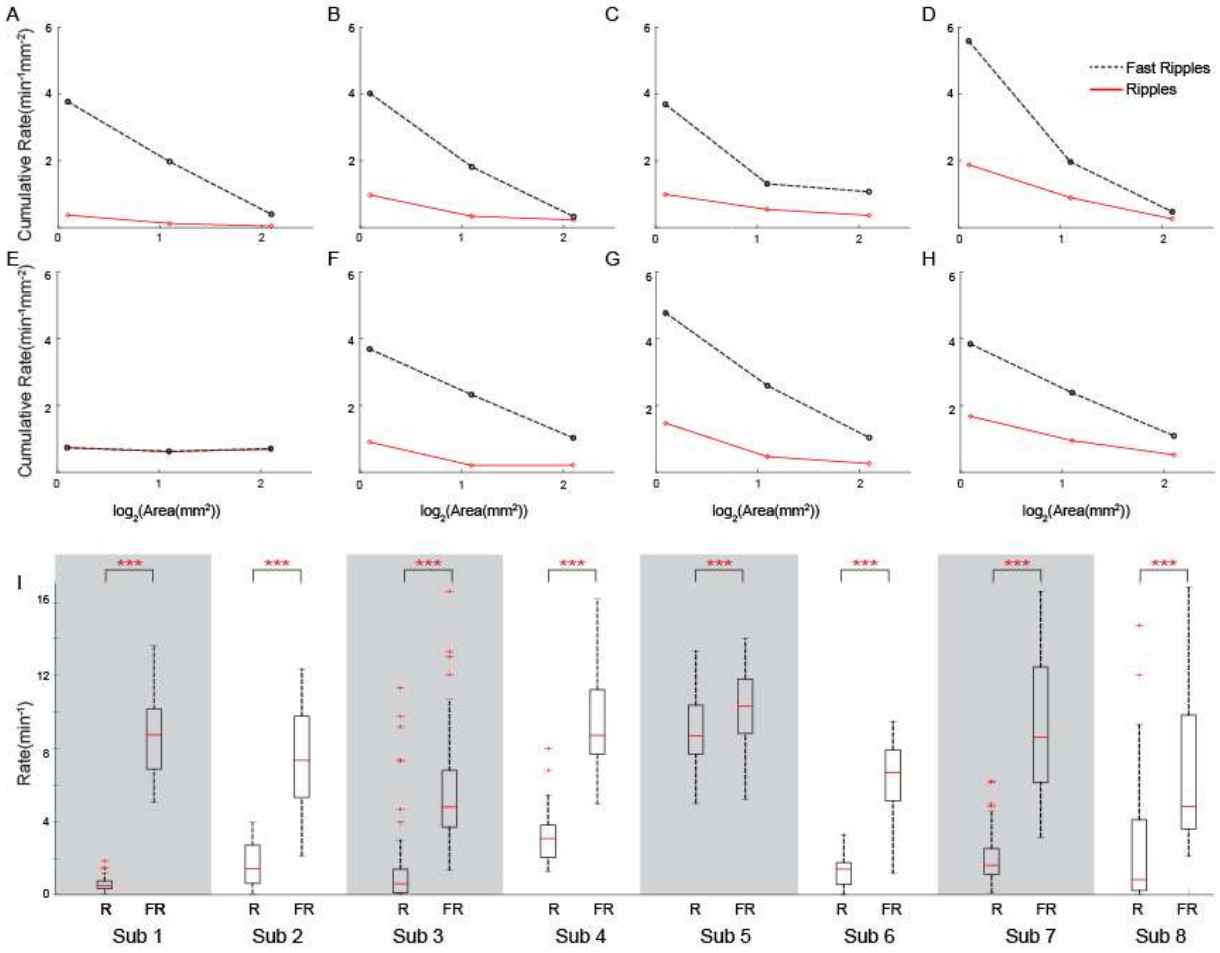

*Figure 4.3: (A-H) Global HFO rate per area of electrode for Subject 1 (subfigure A) through Subject 8 (subfigure H). The dots represent the data points obtained from small, pair, and quad electrodes, summed across the entire HD grid and normalized by total area. (I) Boxplots showing the channel-wise HFO rates for small electrodes within each subject for ripples (R) and fast ripples (FR). * indicates p<0.05, ** indicates p<0.01 and ** indicates p<0.001*

When normalized by the total area of the electrodes in the HD grid, the average rate of HFOs decreased with electrode size in both frequency bands (Figure 3A-H).

Further, the small electrodes recorded more fast ripples than ripples for all subjects ($p<0.001$), which is contrary to results that have been reported for standard clinical electrodes. While this trend was observed for pair electrodes too, the difference between ripple and fast ripple rates was significant only in six subjects. In quad electrodes, no significant difference was observed between the rates of ripples and fast ripples in any subject.

4.3.3 HFO amplitude decreased with increase in electrode size

The amplitude of ripples consistently decreased with electrode size, with small electrodes exhibiting significantly higher values than pair electrodes in all subjects ($p<0.001$) and pair electrodes exhibiting significantly higher values than quad electrodes in seven of the eight subjects ($p<0.001$). A similar relationship was observed in fast ripples, with small electrodes exhibiting significantly higher values than pair electrodes in seven subjects ($p<0.001$) and pair electrodes exhibiting significantly higher values than quad electrodes in all eight subjects ($p<0.001$) (Figure 4A-C). HFO duration and peak frequency did not show any such consistent trends across electrode sizes (Figure 4D-I).

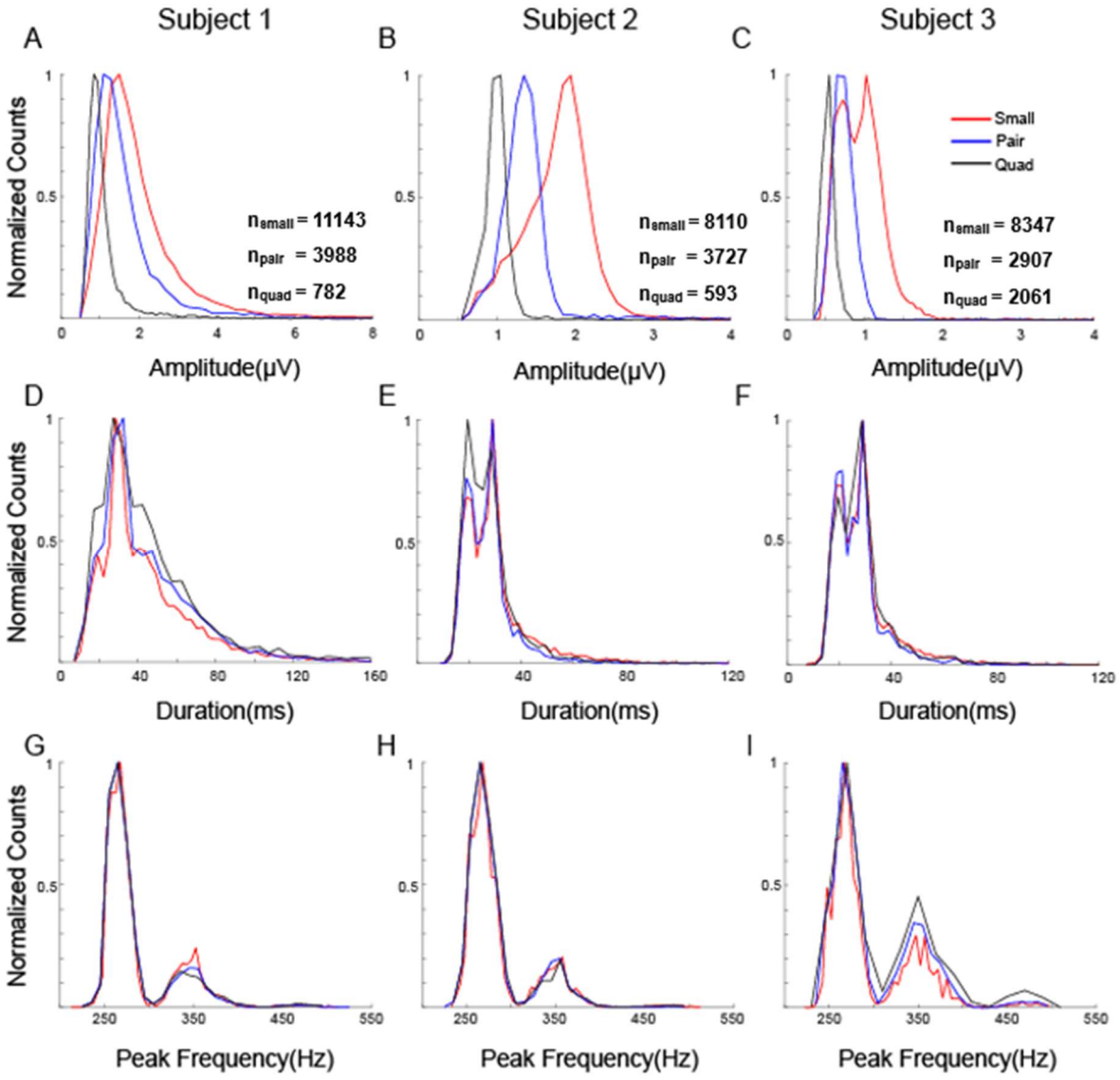

Figure 4.4: Histograms of amplitude (A-C), duration (D-F), and peak frequency (G-I) for small, pair, and quad electrodes in three representative subjects. The normalized counts in the histograms were obtained by dividing each count value by the highest value for each property.

4.3.4 Most HFOs occurred in a single electrode for all electrode sizes

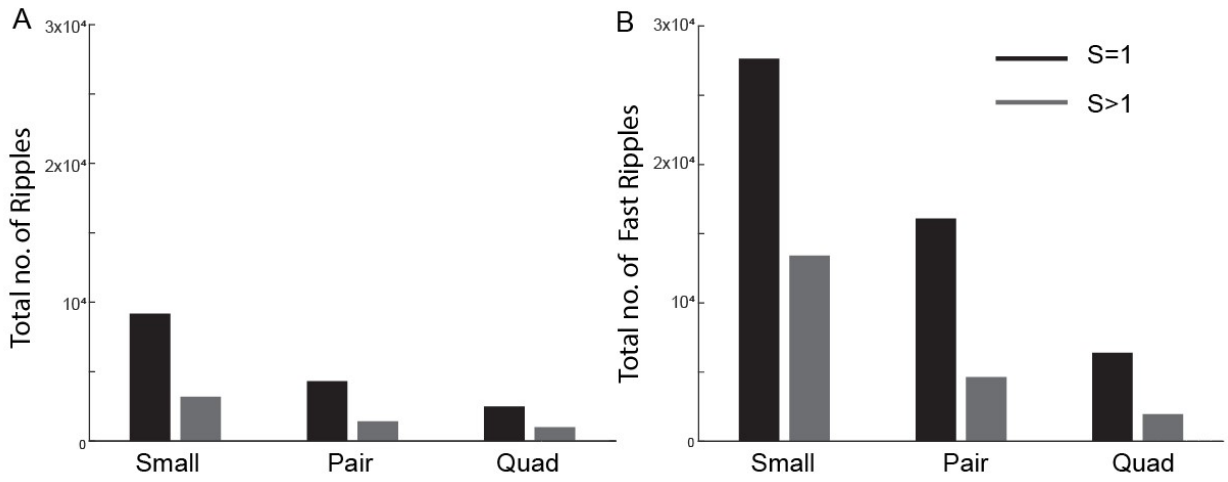

Figure 4.5: Distribution of events with spread = 1 and spread >1 across electrode sizes for (A) ripples and (B) fast ripples summed across all subjects

71% of all recorded HFOs had S=1, implying that HFOs that are localized to smaller regions of tissue occur more frequently than larger HFOs (Figure 5). We would expect that all events with S>1 at one electrode size (e.g., small electrodes) would be measurable using the next largest electrode size (e.g., pair electrodes). In addition, some high-amplitude HFOs with small spatial extent (S=1) will survive the spatial averaging and still be measurable using the next largest electrode size. Consistent with this idea, we found that the pair electrodes recorded approximately twice as many HFOs as the number of HFOs detected by small electrodes with S > 1. A similar relationship was found between pair and quad electrodes, for both ripples and fast ripples.

4.4 Discussion and Conclusions

This is the first study to record HFOs in iEEG using electrodes of different sizes, where all electrodes were placed over the same section of neural tissue. This enabled us to directly compare the rates and morphology of HFOs between electrode sizes, thus eliminating a major confounding factor associated with such comparisons in previous studies, namely the variation of HFO characteristics due to the placement of electrodes in different brain regions.

We found that the rate and amplitude of HFOs significantly decrease as electrode size decreases. HFOs are believed to have small neural generators compared to the size of standard iEEG electrodes (179). Recording using a larger surface area may average HFOs with the low amplitude background, thus making the amplitude of the event smaller. This would result in fewer HFOs standing out from the background, thereby reducing the rate. To confirm that this difference in rate was not due to cases in which a single event co-occurred in multiple electrodes in the smaller electrode configuration, we calculated the rate per area over the entire electrode grid, which also decreased as electrode size increased. This is the only study to be able to reliably calculate this metric over electrode sizes, as the electrodes were all in the same location.

Studies using standard clinical depth and subdural electrodes have reported higher rates of ripples than fast ripples (36, 43, 61, 103). In the small electrode configuration, our results contrast with this as they recorded significantly higher rates of fast ripples than ripples (Figure 3I). However, as the size of the electrode increased, the fast ripple rate fell more quickly than the ripple rate, and their rates in the quad electrode configuration were comparable (Figure 3A-H). This result suggests that measurement of fast ripples may be facilitated by the use of electrodes with smaller surface area.

Accurate localization of the so called "epileptogenic zone," the minimum tissue to be resected to achieve post-surgical seizure freedom, has been a subject of epilepsy research for decades. Identifying regions of high HFO rates has been shown to aid in this (28). We find that in some subjects (Figures 2C and 2E) delineating regions of high HFO rate was possible using any of the three electrode sizes used, while in others (Figures 2D), it was clear only using the smaller electrodes. This suggests that electrode size may impact the efficacy of HFOs as prognostic biomarkers in some patients, and further research in this direction is needed to accurately model this effect.

Subjects with epilepsy are often implanted with multiple types of electrodes. The results of this study indicate that, when determining regions of high HFO rate in such subjects, should be exercised because a higher HFO rate could arise from measurement with a smaller electrode size and may not be indicative of epileptogenicity. Moreover,

HFOs are being increasingly detected using automatic detectors, most of which use some form of amplitude thresholding (1). Because amplitude can also be affected by electrode size, it may call for threshold optimization for each type of electrode separately.

The methods used in this study have similar limitations to those discussed in the original description of the electrode-shorting method (2). Briefly, the shorted electrodes are spaced 3mm apart, and therefore, the ensemble electrode is not contiguous as it would be in the case of a larger electrode placed at the same location. However, we previously compared measurements from the electrically-shorted pair electrodes to measurements from a larger single electrode with an equivalent surface area, and we found no statistically significant differences between the two (CITE methods paper). We were unable to use a grid with a smaller inter-electrode distance as we were limited to FDA-approved electrodes. Further, the recordings from the three configurations were taken sequentially and not simultaneously. This could introduce differences between the recordings owing to the non-stationarity of iEEG signals. We used approximately 20 minutes of data per recording configuration and detected HFOs in 1-minute windows to minimize this effect. The rates of HFOs were observed to be fairly consistent over time, indicating that effects due to sequential recording were minimal.

Overall, these results suggest that HFO rate and amplitude are a function of electrode size, implying that these characteristics cannot be directly compared between

HFOs recorded with electrodes of different sizes. This could represent a significant confounding factor in studies of HFOs as a predictive biomarker of surgical outcome. Further study is required to quantify and model this relationship and understand its clinical relevance for surgical planning.

CHAPTER 5

PHYSIOLOGICAL RIPPLES DURING SLEEP IN SCALP ELECTROENCEPHALOGRAM OF HEALTHY INFANTS

5.1 Introduction

During sleep, physiological high frequency oscillations (HFOs) occur broadly throughout the human brain (64, 129) and are thought to be significant markers of cognition in humans and animals (52). HFOs are empirically defined as events consisting of four or more oscillations in the 80-500Hz frequency range that clearly stand out from background activity in the EEG (28). Ripples are a subset of HFOs whose peak frequency lies between 80 Hz and 250 Hz. Intracranial EEG studies have suggested several possible functions for ripple oscillations. Hippocampal ripples are significantly phase-locked with neocortical slow-wave oscillations during sleep (101), and replay of encoding activity is triggered by ripples during non-rapid eye movement (NREM) sleep, suggesting a role in memory reconsolidation (180, 181). In adults, ripple densities (measured as the number of ripples per minute) are generally higher during sleep than wakefulness, with the highest densities occurring during NREM sleep; however, densities during REM sleep gradually increase as sleep is accumulated (182). During wakefulness, they have been associated

with visual processing (183) and motor function (184-186), as well as language processing and reading tasks (175).

While most studies of physiological ripples have relied on intracranial EEG recordings from patients with epilepsy (101, 129, 180, 181, 183, 187), there is recent evidence that they can be measured noninvasively using scalp EEG. Mooij et al. (2017) was the first study to report spontaneously occurring physiological ripples in scalp EEG. The same group later reported that 74% of scalp ripples co-occurred with sleep transients, primarily vertex waves, and they were most frequently found in the midline channels (Cz, Pz, and Fz) (32). In that study, the ripple densities in N3 sleep were significantly lower than densities in both N1 and N2 sleep. In a subsequent study, they found that physiological ripples occurring in scalp EEG had longer durations, lower amplitudes, and lower frequencies than pathological ripples, which are associated with seizures and epilepsy (188). Windhager et al. (2022) also reported scalp physiological ripples in a small group of healthy adult subjects (n=3). However, most of these prior studies included some subjects with epilepsy, which is a potential confounding factor for the measurement of ripples. Pathological ripples are known to have features that overlap with those of physiological ripples (39, 64, 129). Moreover, when ripples are measured during a routine daytime EEG, the subjects may have also undergone sleep deprivation. This can cause a significant increase in slow-wave activity in subsequent periods of sleep (189), and slow

waves are known to modulate ripple occurrence (190). Lastly, previous studies of scalp physiological ripples relied on visual marking of events in the EEG; this maximized the ability to reject false positive detections due to artifacts such as muscle noise or the filtering of sharp transients. However, it also limited the amount of data that could be analyzed, and such visual detection results are known to vary between readers (68). Therefore, our aim was to measure physiological ripples in a healthy population using long-term scalp EEG and automated detection methods to obtain robust estimates of ripple spatiotemporal characteristics.

To make the detection of ripples in scalp EEG feasible, a high signal-to-noise ratio (SNR) is required. Infants have thinner skulls than adults, which enables the recording of high-SNR scalp EEG data, particularly in the ripple frequency band, where the amplitude is expected to be low. Therefore, for this study we focused on an infant population. We analyzed overnight recordings of scalp EEG data from healthy infants (<12 months old) with no seizures or epilepsy diagnoses. We detected ripples in multiple hours of data from each subject and characterized their duration, peak frequency, root-mean-square (RMS) amplitude, spatial distribution, density (occurrence per minute), and density variability across sleep stages and over time. This work is significant because it represents the most comprehensive analysis of scalp physiological ripples to date. It contributes to our knowledge of high-frequency EEG activity associated with physiological processes in the

brain during sleep and provides baseline measurements that can aid studies of pathological ripples associated with epilepsy.

5.2 Methods

5.2.1 Subjects

This prospective study was approved by the Institutional Review Board of the Children's Hospital of Orange County (CHOC). Data were collected at CHOC between June 2017 and January 2019 as part of a study of a type of seizures called infantile spasms (IS). Subjects were between 0-3 years of age and were undergoing inpatient EEG monitoring for suspicion of IS. To study physiological ripples, we selected for analysis all subjects that did not exhibit IS during monitoring. Further inclusion criteria included a normal Vineland developmental score (Sparrow et al., 2016) and normal MRI. Subjects were excluded if any of the following were true: seizures were observed, subject was on medication at any point in the study, subject had other medical diagnoses, technical error occurred during research recording, or initial results were suspicious for spasms. These exclusion criteria were applied to ensure the cohort consisted only of healthy infants.

5.2.2 EEG Data Collection and preprocessing

Continuous overnight video EEG was recorded for each subject, with recordings starting after consent was obtained and stopping when it was confirmed that the subject

did not exhibit IS. EEG data were acquired with 19 electrodes placed according to the international 10-20 system. The sampling rate was 5 kHz, using a Neurofax EEG-1200 acquisition system with JE-120A amplifier fitted with a QI-124A dual data stream recording unit (Nihon Kohden, Tokyo, Japan). Recordings were visually sleep staged by a registered polysomnographic technologist in accordance with the American Academy of Sleep Medicine (AASM) guidelines. All segments of quiet and active sleep (in subjects younger than four months) and N1, N2, N3, and REM sleep (in subjects older than 4 months) were extracted and analyzed.

The extracted sleep EEG data were re-referenced using a longitudinal bipolar montage. The data were then band-pass filtered in the ripple band (80 - 250 Hz) using a finite impulse response filter.

5.2.3 Ripple Detection

5.2.3.1 Automatic detection

HFOs were automatically detected in the EEG ripple band using an algorithm previously validated in both intracranial (93) and scalp data (191, 192). Briefly, this algorithm estimates the optimum amplitude threshold for the identification of transient high amplitude events, based on a specified parameter α. An iterative approach is used to estimate the amplitude of the background activity in each channel, and this amplitude

is used as the threshold for ripple detection. Events in the ripple band that had three oscillations (six consecutive peaks in the rectified data) above the threshold were identified as candidate ripples. The parameter α is directly related to the significance level for the amplitude threshold, such that a lower value of α corresponds to a higher threshold.

For this study, the data were windowed in five-second segments for ripple detection. This short window length was chosen to ensure that the detection threshold would adapt to the rapidly changing baseline of the scalp EEG, thus minimizing the false detection of muscle noise as HFOs. To choose the α parameter, 10 minutes of sleep data were randomly selected for each subject, and ripples were detected using α values ranging from 0.0025 to 0.05 based on (93). Ripples were also visually marked in this data. The optimal α value for each subject was chosen as the one that resulted in automated detections most closely corresponding to the visual detections. Automatic ripple detection was then done on all sleep EEG data using the optimal α for each subject.

5.2.3.2 Automatic Rejection of Artifacts

Artifacts like muscle noise, DC shifts, and sharp events occur commonly in scalp EEG. These events can pass the threshold for automatic detection and be falsely detected as ripples. To reject these artifactual events, we placed limits on the duration, amplitude, maximum difference, line-length, and number of zero crossings in the detected event. These thresholds were determined based on previous studies or using a method similar to

the one used to determine the optimal detection parameter, α (Section 2.3.1). In all cqases, we chose a conservative threshold, erring on the side of keeping too many events rather than rejecting too many events, as we later visually validated each one (Section 2.3.2).

5.2.3.2.1 Maximum Duration

Ripples in scalp EEG typically have a duration of 40-100 ms (76, 193). Longer events tend to be associated with muscle noise. Therefore, events longer than 200ms in duration were rejected as artifacts.

5.2.3.2.2 Maximum Amplitude

Previous studies indicate that the RMS amplitude of scalp ripples lie in the range of 0.95-5.24 μV (31, 177, 194). Amplitudes that are much higher than this range were observed to be associated with events of non-neural origin, such as those created due to the filtering of sharp artifacts or spikes. Therefore, events with maximum amplitudes in the ripple band greater than 20 μV were rejected as artifacts.

5.2.3.2.3 Maximum Difference

When filtered in the ripple band, events like DC-shifts and fast transients appear similar to real ripples (73) and hence are often detected by automatic algorithms. Such events are characterized by large fluctuations in amplitude in the raw data. Thus,

candidate events with a maximum difference >50 µV between successive data points in the raw data were excluded.

5.2.3.2.4 Line Length

Muscle activity is a common source of scalp EEG artifacts (27). When filtered in the ripple band, these artifacts may look similar to a true ripple. However, they differ in that they often have a high amplitude in the raw data and a longer duration. To measure this, line length was calculated as the sum of distances between successive points in time for windows of EEG that included +/- 150 ms surrounding the candidate events. This accounts for the fact that false ripples due to muscle activity will likely be embedded in longer periods of high amplitude, high frequency activity. Candidate events occurring in windows with line length $> 2000\ \sqrt{\mu V^2 + s^2}$ in the raw data were excluded.

5.2.3.2.5 Number of Zero Crossings

Segments of raw data that excessively cross the zero line are considered artifactual and can be a source of false positive ripple detection; this is in contrast to a typical ripple, which rides on top of the lower frequency EEG activity, away from the zero line (110). Thus, candidate events with >20 zero crossings in the raw data were excluded. The number of zero crossings was calculated using the duration of the candidate event only.

5.2.4 Visual Validation

To further increase the specificity of detection, the remaining candidate events (which were not classified as artifacts by the automated algorithm) were independently visually validated by two reviewers. An event was classified as a true ripple only if both reviewers independently agreed that the event did not have an artifactual origin. To make this determination, each event was viewed using custom MATLAB software that showed the surrounding 5-second segment of broadband EEG (all 19 channels), the broadband EEG in the channel of interest, the filtered EEG in the channel of interest, and the rectified data in the ripple band.

5.2.5 Calculation of ripple properties

For the visually validated events in each channel, we calculated the ripple density (also referred to as "rate" in epilepsy literature), defined as the average number of events occurring in the channel per minute. We also calculated global ripple density, calculated by summing the densities of non-overlapping ripples across all 19 electrodes. For this calculation, ripples that overlapped in time in two or more EEG channels were counted as a single ripple. The channel and global densities were compared across sleep stages and subjects.

We also calculated the RMS amplitude, duration, and peak frequency for each individual ripple and then reported the median values for each sleep stage and subject.

5.2.6 Data Analysis and availability of code

We compared the spatial distribution of ripple densities (in the frontal, temporal, central, parietal, and occipital regions) using a paired Wilcoxon signed rank test for all subjects. We also compared the ripple densities between the left and right brain hemispheres. We repeated these comparisons for amplitude, duration, and peak frequency as well. The p-values obtained were corrected for multiple comparisons using the Bonferroni method.

To analyze how ripple characteristics change with sleep depth, we compared the global ripple properties across available sleep stages. We performed paired Wilcoxon signed rank tests for each channel to assess statistical significance. Because sleep depth is classified differently for infants under and over four months of age, the aforementioned analyses were done separately for these two age groups. We also tested whether these ripple properties were correlated with subject age.

All analyses were done using custom code on MATLAB 2020. Code to perform the initial HFO detection and artifact rejection steps is included as supplementary material.

5.3 Results

5.3.1 Subject Demographics

Based on our inclusion and exclusion criteria, 15 subjects were selected for this study (4 Males/12 Females; Median Age: 6.34 months, IQR: 2.86 – 8.35). For each subject, EEG was recorded continuously for a maximum of 36 hours, with a typical duration of approximately 24 hours. From these recordings, a total of 184.98 hours of sleep EEG (median:11.42 hours per subject, IQR: 9.68 – 13.41 hours) was extracted for analysis. This included 30.65 hours of quiet sleep, 38.78 hours of active sleep, 4.88 hours of N1 sleep, 39.64 hours of N2 sleep, 28.85 hours of N3 sleep, and 31.35 hours of REM sleep. Detailed information for each patient is given in Table 1.

Table 5.1: Subject demographics and EEG data characteristics. (QS – Quiet Sleep, AS – Active sleep)

Subject No.	Sex/Age (Months)	N1/QS Duration (Hrs)	N2 Duration (Hrs)	N3 Duration (Hrs)	REM/AS Duration (Hrs)	Detection Threshold (α)	N1/QS Global HFO Density (per minute)	N2 Global HFO Density (per minute)	N3 Global HFO Density (per minute)	REM/AS Global HFO Density (per minute)
1	F/1.97	5.81	N/A	N/A	9.71	0.0025	0.16	N/A	N/A	0.55
2	M/2.07	6.22	N/A	N/A	6.12	0.005	0.16	N/A	N/A	1.59

3	F/2.2	4.35	N/A	N/A	6.12	0.001	0.08	N/A	N/A	0.23
4	F/2.56	4.30	N/A	N/A	4.85	0.0025	0.15	N/A	N/A	0.43
5	F/3.78	5.39	N/A	N/A	7.26	0.0025	0.39	N/A	N/A	1.04
6	F/4.01	4.58	N/A	N/A	4.72	0.0025	0.21	N/A	N/A	1.78
7	M/5.98	0.60	4.54	3.76	5.06	0.0025	1.05	0.68	0.67	1.34
8	M/6.34	0.52	2.19	2.83	5.88	0.001	1.24	0.68	0.78	0.85
9	F/6.96	1.44	9.95	6.37	12.58	0.0025	0.79	0.75	0.68	1.11
10	F/7.42	0.56	4.09	3.41	3.84	0.005	0.74	0.42	0.29	1.40
11	M/7.72	0.14	3.28	1.35	1.37	0.001	1.18	0.51	0.75	2.64
12	F/8.57	0.42	5.00	2.44	3.82	0.001	0.59	0.35	0.6	2.00
13	F/9.33	0.59	4.65	3.25	5.06	0.005	1.02	0.75	0.74	2.40
14	F/11.14	0.31	3.27	2.73	1.80	0.0025	0.53	0.23	0.48	0.91
15	F/11.27	0.30	2.67	2.71	1.94	0.001	0.22	0.39	0.36	1.16

5.3.2 Ripple Detection

The parameter optimization process gave α values ranging from 0.001-0.005, as shown in Table 1. The automatic detection stage yielded 51000 ripples combined across all 15 subjects, of which 11718 (22.97%) were marked as true ripples through the two-reviewer visual validation process. Figure 1 shows examples of true ripples and ripples rejected by the automatic artifact rejection steps.

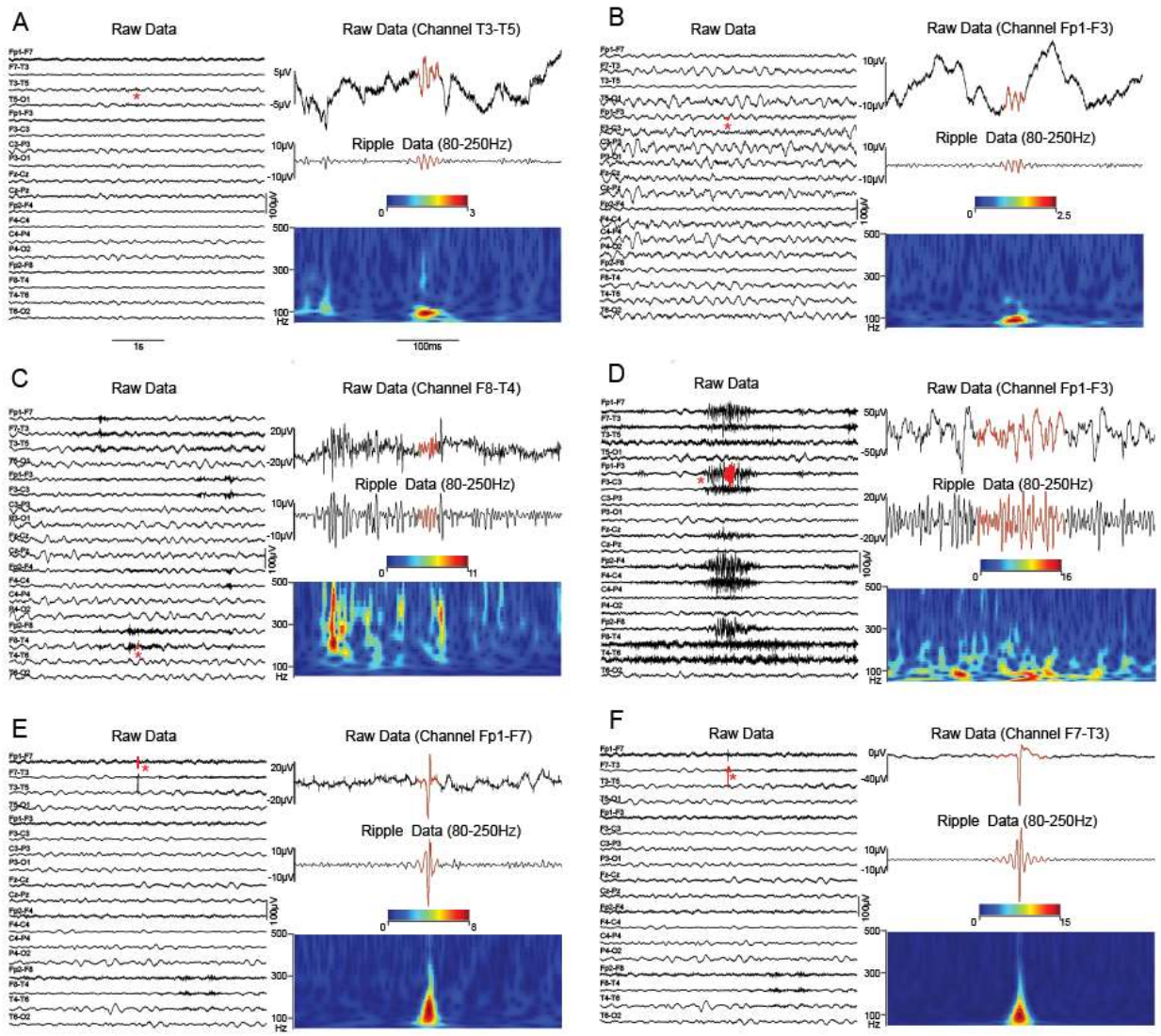

Figure 5.1: (A, B) Examples of ripples detected in the scalp EEG that passed visual validation. (C, D) Examples of muscle activity falsely detected as ripples and rejected by the artifact rejection algorithm. (E, F) Examples of sharp artifacts detected by the ripple detector and rejected by the artifact rejection algorithm. Each subfigure shows five seconds of broadband data centered around the event (in red, marked with a red asterisk) on the left. The right subfigures display signals from the channel in which the event occurred, corresponding to broadband data (top), data bandpass filtered in the 80-250Hz band (middle) and the time frequency decomposition of the broadband data (bottom).

5.3.3 Ripple characteristics

For subjects under four months old, the median RMS amplitude, duration, and peak frequency of all ripples was found to be 2.12μV (IQR: 1.76-2.61μV, Figure 2A), 32.2ms (IQR: 26.0-38.2ms, Figure 2B), and 99Hz (IQR: 92-115, Figure 2C) respectively. The values for subjects over four months of age were similar to the values for the younger group, with median RMS amplitude equal to 2.6μV (IQR: 2.12-3.22μV, Figure 2D), median duration equal to 33.0ms (IQR: 26.2-40.6ms, Figure 2E), and median peak frequency equal to 99Hz (IQR: 92-118, Figure 2F). When comparing ripple features in REM versus NREM sleep, we found that the amplitude was lower for REM sleep ($p<0.001$, Figure 3A), but the effect size was small (Cohen's $d=0.18$). We found no significant difference in duration or peak frequency between REM and NREM stages of sleep ($p>0.5$; Figure 3B,C).

The global ripple densities for each subject are given in Table 1. The highest density was 1.66 HFOs per minute summed across all 19 EEG channels; therefore, in any 1-minute of EEG data, most channels did not exhibit any ripples.

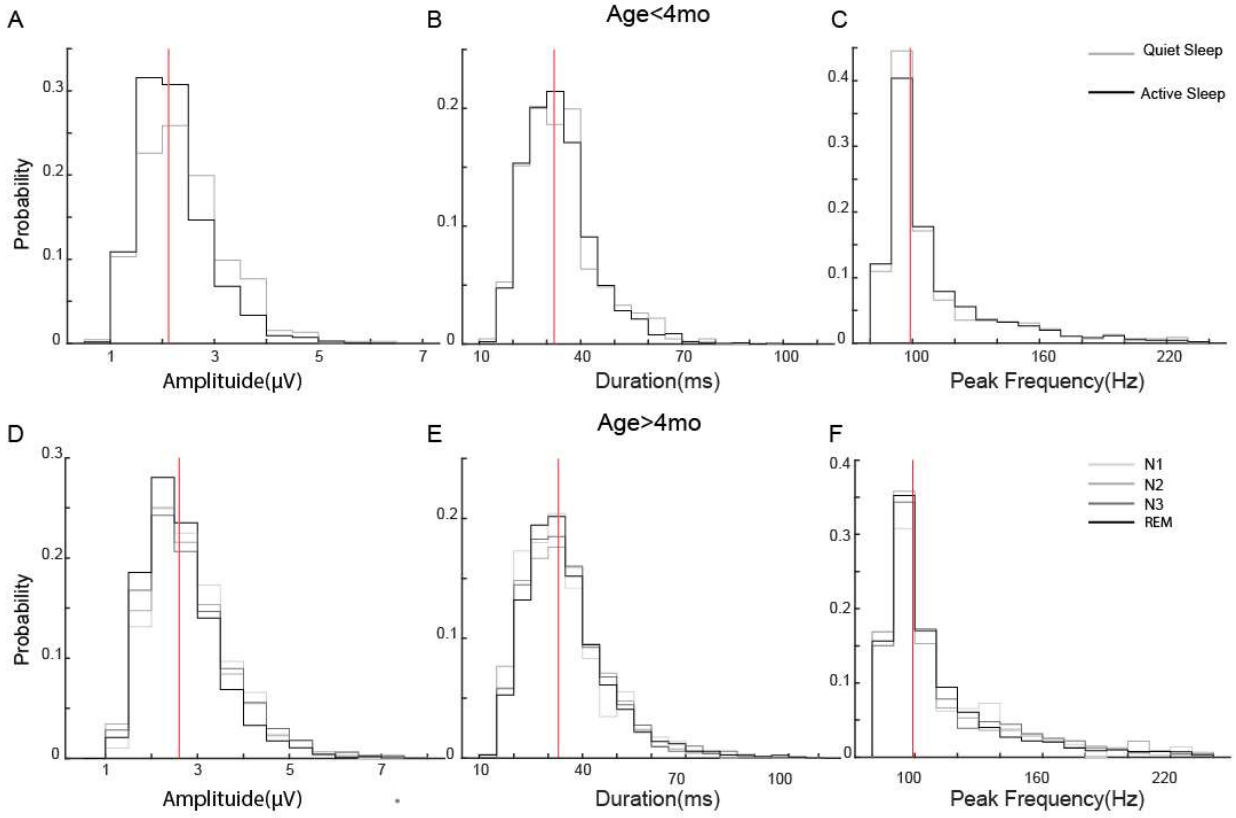

Figure 5.2: Histograms of ripple characteristics. The top row corresponds to subjects under four months of age and the bottom row corresponds to subjects over four months of age. (A, D) ripple amplitude, (B, E) ripple duration, and (C, F) ripple peak frequency for all sleep stages. Vertical red lines indicate the median across all sleep stages.

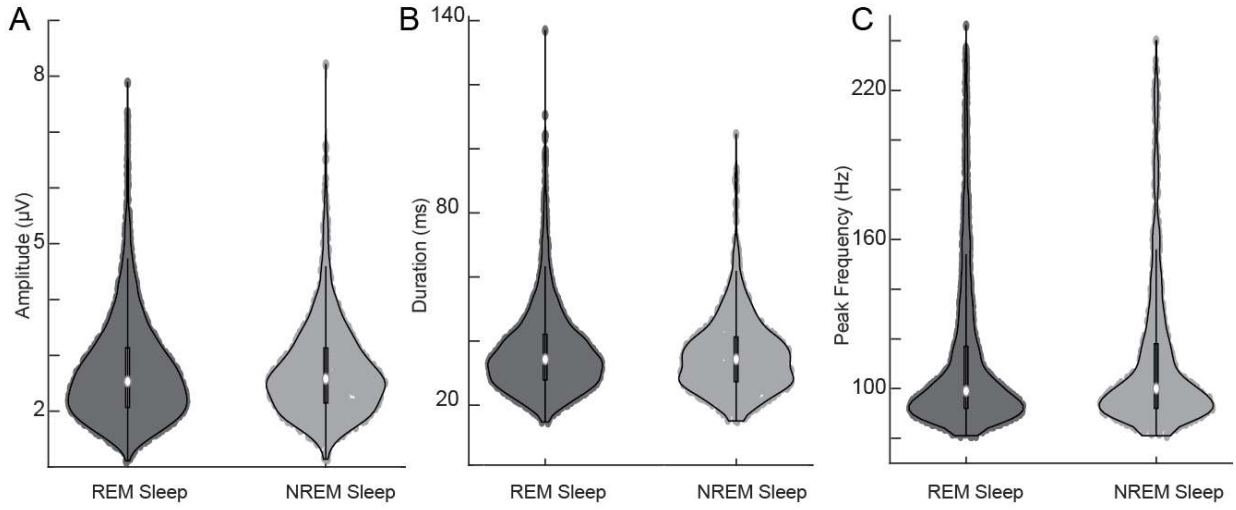

Figure 5.3: Comparison of ripple characteristics between REM and NREM sleep. (A) Amplitude (B) Duration (C) Peak frequency

5.3.4 Ripple densities are higher in frontal regions than posterior regions

The ripple density had a nonuniform spatial distribution that varied by sleep stage, for both subjects younger than four months (Figure 4A) and subjects older than four months (Figure 4B). For subjects younger than four months, median ripple densities were not significantly different between different between brain regions (Figures 4A and 4C, left). For subjects older than four months, the highest densities were seen in the frontal, temporal, and prefrontal regions across all sleep stages (Figures 4B and 4D, left). The lowest densities occurred in the parietal region in both age groups. For subjects older than four months, the ripple densities in the anterior regions of the brain were significantly higher than the densities in the posterior regions (Figure 4D, middle), while there was no significant difference between densities in these regions in subjects younger than four months (Figure 4C, middle). Densities in the left and right hemispheres were not significantly different for either age group (Figures 4C and 4D, right).

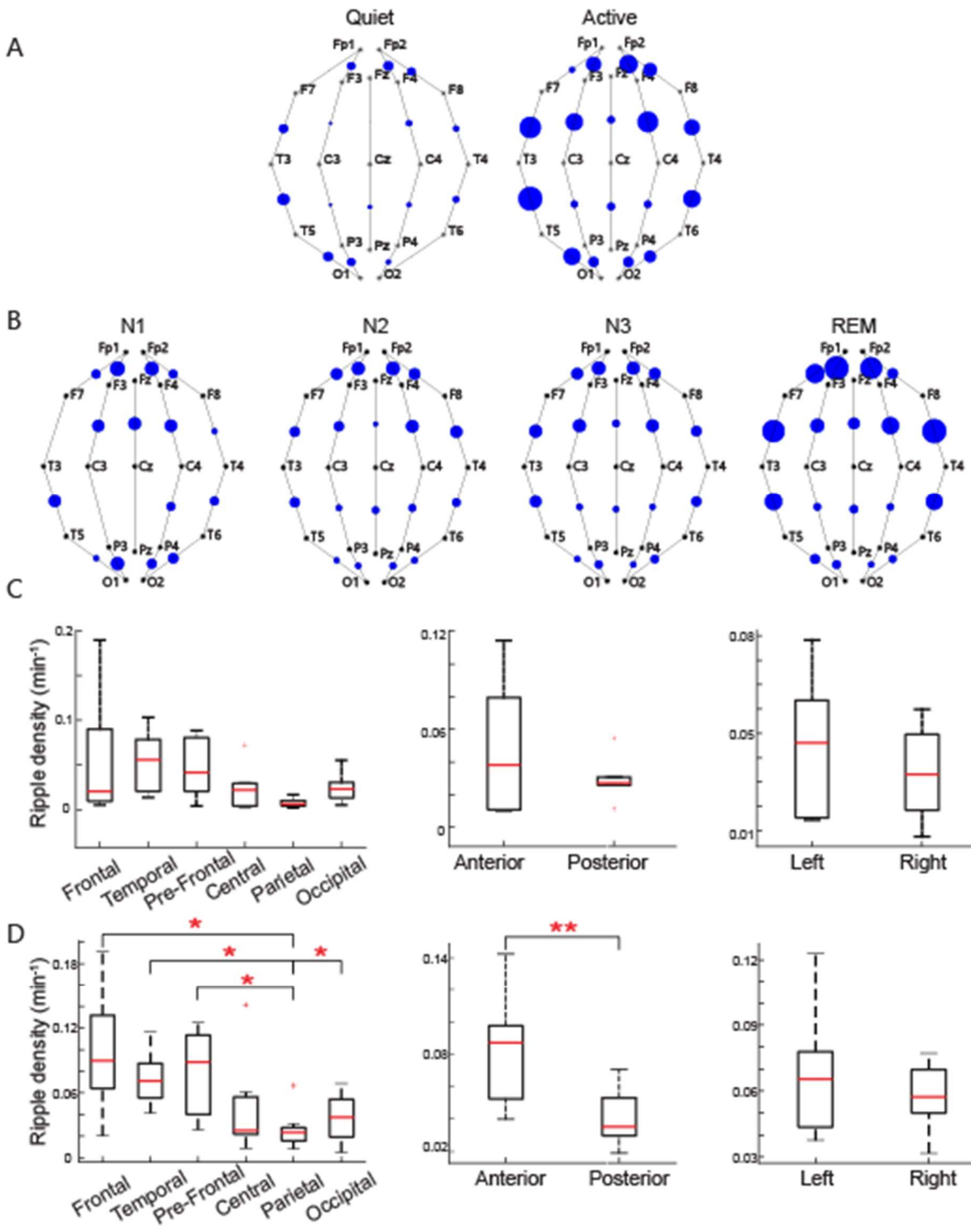

Figure 5.4: (A) Spatial distribution of ripple densities for subjects <4 months old and (B) subjects >4 months old. The area of each blue circle is proportional to the density for that bipolar channel pair. (C) Boxplots of mean (per subject) ripple densities for subjects <4 months old and (D) subjects >4 months old from different anatomical regions (left),

*anterior and posterior regions (middle), and left and right hemispheres (right). Regions are defined as frontal (Fp1-F3, Fp1-F7, Fp2-F4, Fp2-F8), temporal (F7-T3, T3-T5, F8-T4, T4-T6), prefrontal (F3-C3, F4-C4), central (Fz-Cz, Cz-Pz), parietal (C3-P3, C4-P4), and occipital (T3-O1, P3-O1, T4-O2, P4-O2). (* indicates p-value $<$ 0.05, ** indicates p-value $<$ 0.01; all p-values are corrected for multiple comparisons using the Bonferroni method)*

5.3.5 Global ripple densities are the highest in REM sleep

For subjects less than four months of age, the global ripple density in quiet sleep was significantly lower than in active sleep. This relationship was visible in each individual subject (Figure 5A) and when the data were grouped across subjects (Figure 5B). For subjects older than four months, individual results showed a pattern in which REM sleep generally exhibited the highest densities, followed by N1 sleep (Figure 5A). This was consistent with the group results, in which REM sleep had densities that were significantly higher than N2 and N3, and densities in N1 sleep were significantly higher than those in N2 sleep (Figure 5B).

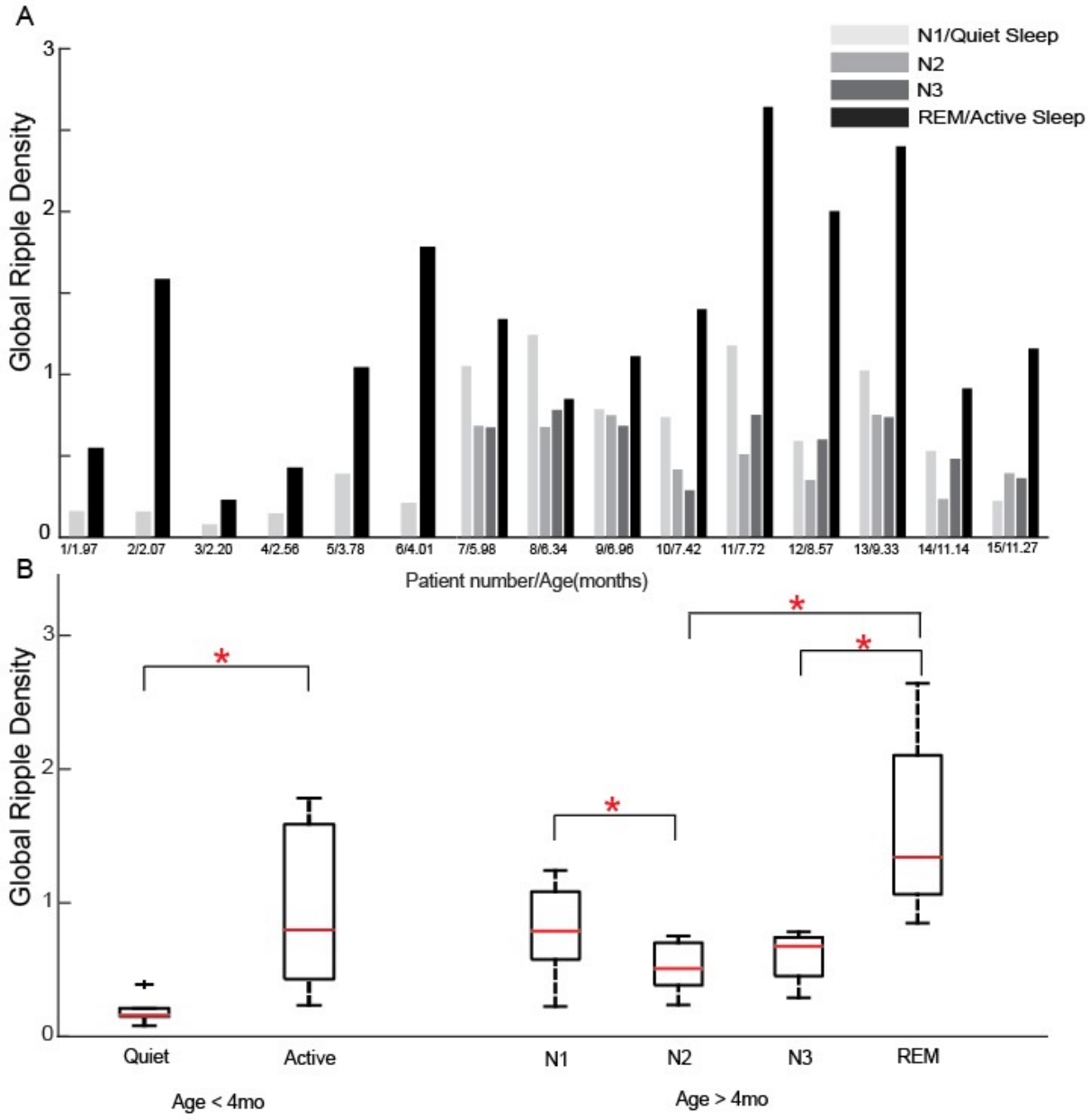

Figure 5.5: (A) Global ripple densities per sleep stage for each subject. Subjects are listed in order by increasing age. (B) Boxplots of global ripple densities across all subjects <4 months old (left) and >4 months old (right). The boxplots were generated using data points corresponding to the average value for each subject. (indicates p-value < 0.05, all p-values are corrected for multiple comparisons using the Bonferroni method)*

5.3.6 Ripple amplitude and duration are correlated with age

We found that ripple density and peak frequency were not correlated with age (correlation coefficient <0.5; p-value >0.5; Fi gures 6A and 6D). The amplitude of ripples was strongly correlated with the age of the subject (correlation coefficient = 0.73; p-value = 0.02; Figure 6B). Ripple duration was also found to be weakly correlated with age (correlation coefficient =0.53; p-value=0.04; Figure 6C). These relationships generally remained consistent when the data were broken down into different sleep stages (Figure S4).

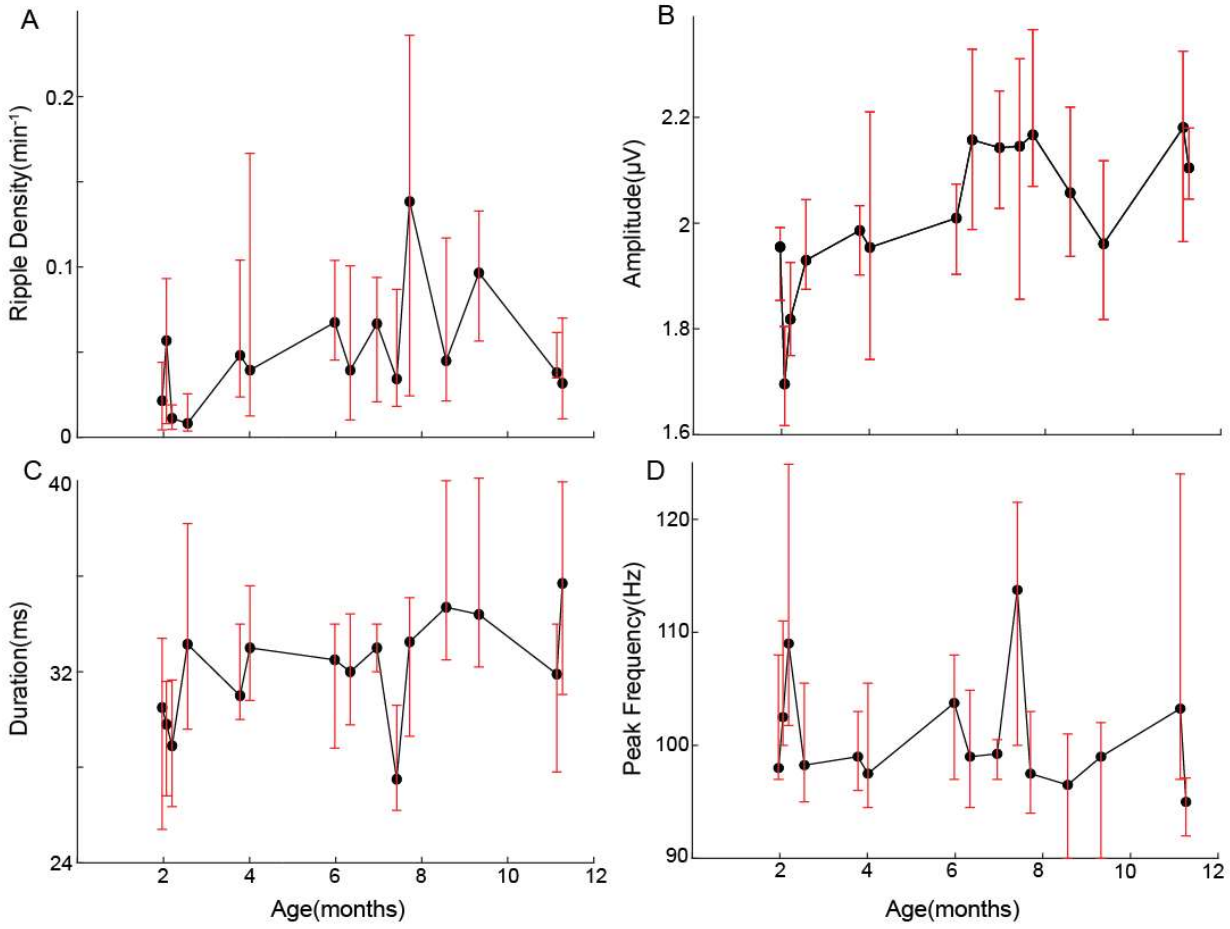

Figure 5.6: Ripple characteristics as a function of subject age: (A) Global ripple density, (B) ripple amplitude, (C) ripple duration, and (D) ripple peak frequency. In each subfigure, the median value across all channels is indicated by a filled black circle and the IQR is indicated by a red line.

5.4 Discussion

This is the most comprehensive study of scalp ripples in healthy human subjects to date. It is the first to identify and characterize scalp ripples in long-term EEG (hours of data, as opposed to minutes) and study an exclusively healthy population, and it is the only investigation of scalp ripples thus far to use an automated detection algorithm to reduce bias. It is also the first to study an infant population and include REM sleep in the analysis.

We found that ripple densities were significantly higher in the anterior regions of the brain than the posterior regions for subjects older than four months, but this difference was not significant in the subjects younger than four months. The frontal, temporal, and prefrontal regions had the highest ripple densities across all sleep stages and subjects. For subjects less than four months old, the global ripple density during active sleep was significantly higher than in quiet sleep. For subjects older than four months, REM sleep exhibited the highest densities, followed by N1 sleep. We found that subject age was highly correlated with ripple amplitude and weakly correlated with duration, but it was not correlated with global ripple density or peak frequency.

Ripple amplitude values reported in this study are comparable to those reported in Mooij et al., 2017 and von Ellenrieder et al., 2016, while lower than those reported in Alkawadri et al., 2014 and Cimbalnik et al., 2018 (31, 39, 64, 125). However, the latter studies used intracranial recordings, thus the difference in amplitude can be expected. Peak frequency values reported in this study are comparable to those reported in Mooij et al., 2017, von Ellenrieder et al., 2016, and Alkawadri et al., 2014, while lower than those reported in Cimbalnik et al., 2018. Cimbalnik et al., 2018 studied a wider frequency range (65-600 Hz) and analyzed intracranial EEG, which likely contributed to this difference. The durations reported in this study are lower than the 69-170ms durations previously observed in other studies of physiological ripples (31, 64, 125). The algorithm for automated detection may have contributed to this difference. The automated detector we used is designed to detect the central oscillations in each event that exceed a threshold, and no windowing is used to calculate the amplitude during the detection procedure. For example, if we had instead used the RMS amplitude for initial detection, the amplitude value would represent the integration of signal information within a window of time and would thus taper off more gradually at the edges of each event. Thus, our reported event duration will be slightly shorter than the event duration associated with other detectors like the one based on RMS amplitude (72).

Scalp EEG contains considerably more artifacts than intracranial EEG, in which ripples are more commonly recorded. Therefore, we used multiple steps to prevent the false classification of artifacts as ripples. We chose the time window for automatic detection to be five seconds, as we found that it was optimal to reject muscle noise. We also used a five-step automatic algorithm to reject false positive detections due to artifacts, including muscle noise, DC shifts, and sharp transients. A significant number of artifacts remained even after this step, which prompted visual validation, and this was done by two independent reviewers.

We found that ripple density was the highest in REM sleep, and it is possible that false positive detections associated with muscle activity are a confounding factor in this result. However, there are several reasons that this is unlikely. Although EEG during REM sleep and wakefulness have similar features, an important difference is the strong suppression of muscle activity during the former (195). Contamination of EEG by muscle noise has been reported to be marginally higher in REM compared to NREM sleep (196, 197), but this would not account for the incommensurate increase in ripple density that we see during REM sleep. Additionally, the spatial pattern of muscle noise, with high influence on the temporal and central channels in REM sleep (196), does not match the high densities seen in the frontal channels in this study. To further confirm that the high densities in REM sleep were not due to muscle artifacts, we compared the amplitude,

duration and peak frequency of ripples occurring during REM sleep with ripples in the other sleep stages and found no significant differences for duration and peak frequency (Figures 2, 3, S2 and S3). Amplitude was slightly lower in REM compared to NREM sleep, with a small effect size (Figures 2, 3, and S1). This is the opposite of what would be expected if the events detected during REM were false positives due to muscle artifacts, as muscle artifacts are expected to have higher amplitude and duration than real ripples. Note also that the values for amplitude and duration are well below the automated cutoff values for these features (20 μV and 200 ms), so the low values were not artificially created by the thresholding in the artifact rejection steps.

Another possible source of false positive detections specific to REM sleep is eye movement. However, studies have shown that eye movements during REM sleep lead to an increase in power predominantly in the delta band, with minimal effects on the higher frequency bands (196, 198). Therefore, the ripple band can be assumed to be relatively free of such ocular artifacts. Lastly, each event was visually confirmed by two independent reviewers, thus reducing the probability of falsely marking both muscle and ocular artifacts as ripples.

Previous studies done on pathological ripples in subjects with epilepsy (199-201) showed that the density of ripples was the lowest in REM sleep. This difference in results could be caused by different underlying mechanisms for the two types of events. It has

been shown that there is a suppression of epileptic activity in REM sleep (202), which could account for the low ripple densities observed in REM sleep in patients with epilepsy. Moreover, the densities of pathological ripples are typically much higher than those of physiological ripples, which further adds to this effect. A study done on iEEG data from depth macroelectrodes found that there was no significant difference in ripple densities in REM sleep when comparing the seizure onset zone (SOZ) and non-SOZ regions (199). This may be because ripples observed in REM sleep are more likely to be purely physiological, explaining their low densities compared to pathological ripples in other stages of sleep. A scalp EEG study on physiological ripples (32) during NREM sleep found that ripple densities decreased with depth of sleep, which aligns with the results seen in this study. It is also to be noted that the infants in this study (1-12 months old) are much younger than the subjects in the previous studies discussed here, and newborn sleep stages and EEG are known to be markedly different from those of adults.

Some existing literature on scalp EEG changes during sleep-wake states report results in various subsets of the gamma band (35-120Hz) that mirror our results. It has been shown that gamma activity increases as sleep progresses from NREM to REM, especially in the frontal cortex (203, 204). An intracranial EEG study done on channels with no epileptic activity from subjects with epilepsy showed that gamma band amplitude is higher in REM sleep than NREM sleep (205). This study also found that gamma

amplitude in periods of REM sleep with no eye movement was higher than that in NREM sleep which suggests that the increase in gamma oscillations in REM sleep is not solely due to eye movements. Yamada et al. showed in a scalp EEG study that high-frequency oscillations (called fast-frequency peaks in the study) in somatosensory evoked potentials (SEPs) decrease in amplitude from REM to NREM sleep, with the highest differences being seen in the frontal cortex (206).

In adults, physiological ripples during NREM have been associated with cognitive processes like memory consolidation. This activity happens primarily in the hippocampus, but correlates of this process have been found in the neocortex (207). In addition, neocortical ripples exhibit coupling with specific NREM features like slow waves and sleep spindles, which play a role in memory consolidation (32, 208-210). Therefore, it is noteworthy that, while ripples are predominantly associated with NREM sleep in adults, our results indicate a strong association between REM sleep and ripples in infants. However, because most studies of physiological ripples in adults are done in NREM sleep (while excluding REM sleep), it is unclear if this phenomenon is specific to infants (31, 32, 211).

Unlike physiological ripples, pathological ripples are associated with disease and are thought to be promising biomarkers of epileptogenic tissue in patients with epilepsy (59). It has been shown that accounting for physiological ripples in the iEEG analysis can

improve the accuracy of ripples for localization of the SOZ in patients with epilepsy (212). However, while these two types of ripples differ in their significance, their morphological features are similar, including frequency, duration, and amplitude (39, 53), as well as their relative occurrence in different stages of sleep (182). It is thought that ripples that co-occur with spikes and those generated during seizures are likely pathological (103). Ripples that occur on a flat EEG background are also considered pathological, while those observed on an oscillatory background are physiological (213). Even with these distinctions, it is still not possible to definitively classify individual events as pathological or physiological. Therefore, knowledge of region-specific baseline values of physiological ripple densities, which our results provide, is valuable.

This study is the first to use long-term scalp EEG of healthy infants to identify and characterize physiological ripples. These findings may deepen our understanding of the relationship between ripple occurrence and cognitive processes in various stages of sleep. The results of this study also serve as baseline measurements of physiological ripples to improve the identification of pathological ripples in pediatric patients with epilepsy.

BIBLOGRAPHY

1 Remakanthakurup Sindhu K, Staba R, Lopour BA. Trends in the use of automated algorithms for the detection of high-frequency oscillations associated with human epilepsy. Epilepsia. 2020 2020/08/01;**61**(8):1553-69.

2 Remakanthakurup Sindhu K, Ngo D, Ombao H, Olaya JE, Shrey DW, Lopour BA. A novel method for dynamically altering the surface area of intracranial EEG electrodes. Journal of neural engineering. 2023.

3 IOM (Institute of Medicine). Epilepsy Across the Spectrum: Promoting Health and Understanding Washington, D.C.: The National Academies Press; 2012.

4 Fisher RS, Boas WvE, Blume W, et al. Epileptic Seizures and Epilepsy: Definitions Proposed by the International League Against Epilepsy (ILAE) and the International Bureau for Epilepsy (IBE). Epilepsia. 2005 2005/04/01;**46**(4):470-2.

5 Shorvon S. The concept of symptomatic epilepsy and the complexities of assigning cause in epilepsy. Epilepsy & Behavior. 2014 2014/03/01/;**32**:1-8.

6 Sperling MR. The Consequences of Uncontrolled Epilepsy. CNS Spectrums. 2004;**9**(2):98-109.

7 Falco-Walter JJ, Scheffer IE, Fisher RS. The new definition and classification of seizures and epilepsy. Epilepsy research. 2018 2018/01/01/;**139**:73-9.

8 Goldenberg M. Overview of drugs used for epilepsy and seizures: etiology, diagnosis, and treatment. . P & T : a peer-reviewed journal for formulary management,. 2010;**35(7):392-415**.

9 Moshé SL, Perucca E, Ryvlin P, Tomson T. Epilepsy: new advances. The Lancet. 2015;**385**(9971):884-98.

10 Rogawski MA, Löscher W. The neurobiology of antiepileptic drugs. Nature Reviews Neuroscience. 2004 2004/07/01;**5**(7):553-64.

11 Consales A, Casciato S, Asioli S, et al. The surgical treatment of epilepsy. Neurological Sciences. 2021 2021/06/01;**42**(6):2249-60.

12 Engel J. Surgical Treatment for Epilepsy: Too Little, Too Late? JAMA. 2008;**300**(21):2548-50.

13 Englot DJ, Chang EF. Rates and predictors of seizure freedom in resective epilepsy surgery: an update. Neurosurgical Review. 2014 2014/07/01;**37**(3):389-405.

14 Pittau F, Grouiller F, Spinelli L, Seeck M, Michel C, Vulliemoz S. The Role of Functional Neuroimaging in Pre-Surgical Epilepsy Evaluation. Frontiers in neurology. 2014;**5**.

15 Shah AK, Mittal S. Invasive electroencephalography monitoring: Indications and presurgical planning. Annals of Indian Academy of Neurology. 2014;**17**(Suppl 1).

16 Lachaux JP, Rudrauf D, Kahane P. Intracranial EEG and human brain mapping. Journal of Physiology-Paris. 2003 2003/07/01/;**97**(4):613-28.
17 Sperling MR. Clinical Challenges in Invasive Monitoring in Epilepsy Surgery. Epilepsia. 1997 1997/04/01;**38**(s4):S6-S12.
18 Li Z, Fields M, Panov F, Ghatan S, Yener B, Marcuse L. Deep Learning of Simultaneous Intracranial and Scalp EEG for Prediction, Detection, and Lateralization of Mesial Temporal Lobe Seizures. Frontiers in neurology. 2021;**12**.
19 Wong CH, Birkett J, Byth K, et al. Risk factors for complications during intracranial electrode recording in presurgical evaluation of drug resistant partial epilepsy. Acta Neurochirurgica. 2009 2009/01/01;**151**(1):37-50.
20 Parvizi J, Kastner S. Promises and limitations of human intracranial electroencephalography. Nat Neurosci. 2018;**21**(4):474-83.
21 Rosenow F, Lüders H. Presurgical evaluation of epilepsy. Brain : a journal of neurology. 2001;**124**(9):1683-700.
22 Staley KJ, White A, Dudek FE. Interictal spikes: Harbingers or causes of epilepsy? Neuroscience Letters. 2011 2011/06/27/;**497**(3):247-50.
23 Staba RJ, Stead M, Worrell GA. Electrophysiological biomarkers of epilepsy. Neurotherapeutics : the journal of the American Society for Experimental NeuroTherapeutics. 2014 Apr;**11**(2):334-46.
24 Gallotto S, Seeck M. EEG biomarker candidates for the identification of epilepsy. Clinical Neurophysiology Practice. 2023 2023/01/01/;**8**:32-41.
25 Thomas J, Kahane P, Abdallah C, et al. A Subpopulation of Spikes Predicts Successful Epilepsy Surgery Outcome. Annals of neurology. 2023 2023/03/01;**93**(3):522-35.
26 Curtis Md, Jefferys JGR, Avoli M. Interictal Epileptiform Discharges in Partial Epilepsy: Complex Neurobiological Mechanisms Based on Experimental and Clinical Evidence. J L Noebels (Eds) et al, Jasper's Basic Mechanisms of the Epilepsies (4th ed) National Center for Biotechnology Information (US). 2012.
27 Zijlmans M, Jiruska P, Zelmann R, Leijten FS, Jefferys JG, Gotman J. High-frequency oscillations as a new biomarker in epilepsy. Annals of neurology. 2012 Feb;**71**(2):169-78.
28 Frauscher B, Bartolomei F, Kobayashi K, et al. High-frequency oscillations: The state of clinical research. Epilepsia. 2017 Aug;**58**(8):1316-29.
29 Usui N, Terada K, Baba K, et al. Very high frequency oscillations (over 1000Hz) in human epilepsy. Clinical Neurophysiology. 2010 2010/11/01/;**121**(11):1825-31.
30 Bragin A, Engel J, Jr., Wilson CL, Fried I, Mathern GW. Hippocampal and entorhinal cortex high-frequency oscillations (100--500 Hz) in human epileptic brain and in kainic acid--treated rats with chronic seizures. Epilepsia. 1999 Feb;**40**(2):127-37.

31 Mooij AH, Raijmann R, Jansen FE, Braun KPJ, Zijlmans M. Physiological Ripples (+/- 100 Hz) in Spike-Free Scalp EEGs of Children With and Without Epilepsy. Brain topography. 2017 Nov;**30**(6):739-46.
32 Mooij AH, Frauscher B, Goemans SAM, Huiskamp GJM, Braun KPJ, Zijlmans M. Ripples in scalp EEGs of children: co-occurrence with sleep-specific transients and occurrence across sleep stages. Sleep. 2018 Nov 1;**41**(11).
33 Windhager PF, Marcu AV, Trinka E, Bathke A, Höller Y. Are High Frequency Oscillations in Scalp EEG Related to Age? Frontiers in neurology. 2022;**12**.
34 Foffani G, Uzcategui YG, Gal B, Menendez de la Prida L. Reduced spike-timing reliability correlates with the emergence of fast ripples in the rat epileptic hippocampus. Neuron. 2007 Sep 20;**55**(6):930-41.
35 Shiri Z, Manseau F, Lévesque M, Williams S, Avoli M. Interneuron activity leads to initiation of low-voltage fast-onset seizures. Annals of neurology. 2015 2015/03/01;**77**(3):541-6.
36 Jacobs J, LeVan P, Chander R, Hall J, Dubeau F, Gotman J. Interictal high-frequency oscillations (80-500 Hz) are an indicator of seizure onset areas independent of spikes in the human epileptic brain. Epilepsia. 2008 Nov;**49**(11):1893-907.
37 Worrell GA, Gardner AB, Stead SM, et al. High-frequency oscillations in human temporal lobe: simultaneous microwire and clinical macroelectrode recordings. Brain : a journal of neurology. 2008 Apr;**131**(Pt 4):928-37.
38 Andrade-Valenca L, Mari F, Jacobs J, et al. Interictal high frequency oscillations (HFOs) in patients with focal epilepsy and normal MRI. Clinical neurophysiology : official journal of the International Federation of Clinical Neurophysiology. 2012 Jan;**123**(1):100-5.
39 Cimbalnik J, Brinkmann B, Kremen V, et al. Physiological and pathological high frequency oscillations in focal epilepsy. Annals of Clinical and Translational Neurology. 2018;**5**(9):1062-76.
40 Dumpelmann M, Jacobs J, Schulze-Bonhage A. Temporal and spatial characteristics of high frequency oscillations as a new biomarker in epilepsy. Epilepsia. 2014 Dec 30.
41 Guragain H, Cimbalnik J, Stead M, et al. Spatial variation in high-frequency oscillation rates and amplitudes in intracranial EEG. Neurology. 2018 Feb 20;**90**(8):e639-e46.
42 Liu S, Gurses C, Sha Z, et al. Stereotyped high-frequency oscillations discriminate seizure onset zones and critical functional cortex in focal epilepsy. Brain : a journal of neurology. 2018 Mar 1;**141**(3):713-30.
43 Akiyama T, McCoy B, Go CY, et al. Focal resection of fast ripples on extraoperative intracranial EEG improves seizure outcome in pediatric epilepsy. Epilepsia. 2011 Oct;**52**(10):1802-11.

44 Cho JR, Koo DL, Joo EY, et al. Resection of individually identified high-rate high-frequency oscillations region is associated with favorable outcome in neocortical epilepsy. Epilepsia. 2014 Nov;**55**(11):1872-83.
45 Jacobs J, Zijlmans M, Zelmann R, et al. High-frequency electroencephalographic oscillations correlate with outcome of epilepsy surgery. Annals of neurology. 2010 Feb;**67**(2):209-20.
46 Bragin A, Wilson CL, Almajano J, Mody I, Engel J, Jr. High-frequency oscillations after status epilepticus: epileptogenesis and seizure genesis. Epilepsia. 2004 Sep;**45**(9):1017-23.
47 Jacobs J, Wu JY, Perucca P, et al. Removing high-frequency oscillations: A prospective multicenter study on seizure outcome. Neurology. 2018 Sep 11;**91**(11):e1040-e52.
48 Zweiphenning W, Klooster MAvt, van Klink NEC, et al. Intraoperative electrocorticography using high-frequency oscillations or spikes to tailor epilepsy surgery in the Netherlands (the HFO trial): a randomised, single-blind, adaptive non-inferiority trial. The Lancet Neurology. 2022;**21**(11):982-93.
49 Kondylis ED, Wozny TA, Lipski WJ, et al. Detection of High-Frequency Oscillations by Hybrid Depth Electrodes in Standard Clinical Intracranial EEG Recordings. Frontiers in neurology. 2014;**5**:149.
50 Chatillon CE, Zelmann R, Hall JA, Olivier A, Dubeau F, Gotman J. Influence of contact size on the detection of HFOs in human intracerebral EEG recordings. Clinical neurophysiology : official journal of the International Federation of Clinical Neurophysiology. 2013 Aug;**124**(8):1541-6.
51 Chatillon CE, Zelmann R, Bortel A, Avoli M, Gotman J. Contact size does not affect high frequency oscillation detection in intracerebral EEG recordings in a rat epilepsy model. Clinical neurophysiology : official journal of the International Federation of Clinical Neurophysiology. 2011 Sep;**122**(9):1701-5.
52 Buzsaki G, Silva FL. High frequency oscillations in the intact brain. Progress in neurobiology. 2012 Sep;**98**(3):241-9.
53 Matsumoto A, Brinkmann BH, Matthew Stead S, et al. Pathological and physiological high-frequency oscillations in focal human epilepsy. J Neurophysiol. 2013 Oct;**110**(8):1958-64.
54 Kwan P, Brodie MJ. Early identification of refractory epilepsy. The New England journal of medicine. 2000 Feb 3;**342**(5):314-9.
55 Wiebe S, Blume WT, Girvin JP, Eliasziw M. A Randomized, Controlled Trial of Surgery for Temporal-Lobe Epilepsy. New England Journal of Medicine. 2001 2001/08/02;**345**(5):311-8.

56 Wieser HG, Blume WT, Fish D, et al. Proposal for a New Classification of Outcome with Respect to Epileptic Seizures Following EpilepsySurgery. Epilepsia. 2001 2001/02/08;**42**(2):282-6.
57 Kovac S, Vakharia VN, Scott C, Diehl B. Invasive epilepsy surgery evaluation. Seizure. 2017 Jan;**44**:125-36.
58 Ryvlin P, Cross JH, Rheims S. Epilepsy surgery in children and adults. The Lancet Neurology. 2014 2014/11/01/;**13**(11):1114-26.
59 Thomschewski A, Hincapie AS, Frauscher B. Localization of the Epileptogenic Zone Using High Frequency Oscillations. Frontiers in neurology. 2019;**10**:94.
60 Zijlmans M, Worrell GA, Dumpelmann M, et al. How to record high-frequency oscillations in epilepsy: A practical guideline. Epilepsia. 2017 Aug;**58**(8):1305-15.
61 van Klink NE, Van't Klooster MA, Zelmann R, et al. High frequency oscillations in intra-operative electrocorticography before and after epilepsy surgery. Clinical neurophysiology : official journal of the International Federation of Clinical Neurophysiology. 2014 Nov;**125**(11):2212-9.
62 Jefferys JG, Menendez de la Prida L, Wendling F, et al. Mechanisms of physiological and epileptic HFO generation. Progress in neurobiology. 2012 Sep;**98**(3):250-64.
63 Menendez de la Prida L, Staba RJ, Dian JA. Conundrums of high-frequency oscillations (80-800 Hz) in the epileptic brain. Journal of clinical neurophysiology : official publication of the American Electroencephalographic Society. 2015 Jun;**32**(3):207-19.
64 Alkawadri R, Gaspard N, Goncharova, II, et al. The spatial and signal characteristics of physiologic high frequency oscillations. Epilepsia. 2014 Dec;**55**(12):1986-95.
65 Pail M, Řehulka P, Cimbálník J, Doležalová I, Chrastina J, Brázdil M. Frequency-independent characteristics of high-frequency oscillations in epileptic and non-epileptic regions. Clinical Neurophysiology. 2017;**128**(1):106-14.
66 Bragin A, Engel J, Jr., Wilson CL, Fried I, Buzsaki G. High-frequency oscillations in human brain. Hippocampus. 1999;**9**:137-42.
67 Spring AM, Pittman DJ, Aghakhani Y, et al. Interrater reliability of visually evaluated high frequency oscillations. Clinical neurophysiology : official journal of the International Federation of Clinical Neurophysiology. 2017 Mar;**128**(3):433-41.
68 Spring AM, Pittman DJ, Aghakhani Y, et al. Generalizability of High Frequency Oscillation Evaluations in the Ripple Band. Frontiers in neurology. 2018;**9**:510.
69 Gardner AB, Worrell GA, Marsh E, Dlugos D, Litt B. Human and automated detection of high-frequency oscillations in clinical intracranial EEG recordings. Clinical neurophysiology : official journal of the International Federation of Clinical Neurophysiology. 2007 May;**118**(5):1134-43.

70 Worrell GA, Jerbi K, Kobayashi K, Lina JM, Zelmann R, Le Van Quyen M. Recording and analysis techniques for high-frequency oscillations. Progress in neurobiology. 2012 Sep;**98**(3):265-78.
71 Wu M, Wan T, Ding M, Wan X, Du Y, She J. A New Unsupervised Detector of High-Frequency Oscillations in Accurate Localization of Epileptic Seizure Onset Zones. IEEE transactions on neural systems and rehabilitation engineering : a publication of the IEEE Engineering in Medicine and Biology Society. 2018 Dec;**26**(12):2280-9.
72 Staba RJ, Wilson CL, Bragin A, Fried I, Engel J, Jr. Quantitative analysis of high-frequency oscillations (80-500 Hz) recorded in human epileptic hippocampus and entorhinal cortex. J Neurophysiol. 2002 Oct;**88**(4):1743-52.
73 Benar CG, Chauviere L, Bartolomei F, Wendling F. Pitfalls of high-pass filtering for detecting epileptic oscillations: a technical note on "false" ripples. Clinical neurophysiology : official journal of the International Federation of Clinical Neurophysiology. 2010 Mar;**121**(3):301-10.
74 Roehri N, Lina JM, Mosher JC, Bartolomei F, Benar CG. Time-Frequency Strategies for Increasing High-Frequency Oscillation Detectability in Intracerebral EEG. IEEE transactions on bio-medical engineering. 2016 Dec;**63**(12):2595-606.
75 Charupanit K, Sen-Gupta I, Lin JJ, Lopour BA. Detection of anomalous high-frequency events in human intracranial EEG. Epilepsia Open. 2020 2020/05/03;**5**(2):263-73.
76 von Ellenrieder N, Andrade-Valenca LP, Dubeau F, Gotman J. Automatic detection of fast oscillations (40-200 Hz) in scalp EEG recordings. Clinical neurophysiology : official journal of the International Federation of Clinical Neurophysiology. 2012 Apr;**123**(4):670-80.
77 Schevon CA, Trevelyan AJ, Schroeder CE, Goodman RR, McKhann G, Jr., Emerson RG. Spatial characterization of interictal high frequency oscillations in epileptic neocortex. Brain : a journal of neurology. 2009 Nov;**132**(Pt 11):3047-59.
78 Ren G-P, Yan J-Q, Yu Z-X, et al. Automated Detector of High Frequency Oscillations in Epilepsy Based on Maximum Distributed Peak Points. International journal of neural systems. 2018;**28**(01):1750029.
79 Gliske SV, Irwin ZT, Davis KA, Sahaya K, Chestek C, Stacey WC. Universal automated high frequency oscillation detector for real-time, long term EEG. Clinical neurophysiology : official journal of the International Federation of Clinical Neurophysiology. 2016 Feb;**127**(2):1057-66.
80 Gliske SV, Irwin ZT, Chestek C, et al. Variability in the location of high frequency oscillations during prolonged intracranial EEG recordings. Nature communications. 2018 Jun 1;**9**(1):2155.

81 Zijlmans M, Jacobs J, Kahn YU, Zelmann R, Dubeau F, Gotman J. Ictal and interictal high frequency oscillations in patients with focal epilepsy. Clinical Neurophysiology. 2011 2011/04/01/;**122**(4):664-71.
82 Zijlmans M, Jacobs J, Zelmann R, Dubeau F, Gotman J. High-frequency oscillations mirror disease activity in patients with epilepsy. Neurology. 2009 Mar 17;**72**(11):979-86.
83 Zelmann R, Mari F, Jacobs J, Zijlmans M, Chander R, Gotman J. Automatic detector of high frequency oscillations for human recordings with macroelectrodes. Conference proceedings : Annual International Conference of the IEEE Engineering in Medicine and Biology Society IEEE Engineering in Medicine and Biology Society Conference. 2010;**2010**:2329-33.
84 Cimbalnik J, Hewitt A, Worrell G, Stead M. The CS algorithm: A novel method for high frequency oscillation detection in EEG. Journal of neuroscience methods. 2018 Jan 1;**293**:6-16.
85 Murphy PM, von Paternos AJ, Santaniello S. A novel HFO-based method for unsupervised localization of the seizure onset zone in drug-resistant epilepsy. Conference proceedings : Annual International Conference of the IEEE Engineering in Medicine and Biology Society IEEE Engineering in Medicine and Biology Society Conference. 2017 Jul;**2017**:1054-7.
86 Chaibi S, Sakka Z, Lajnef T, Samet M, Kachouri A. Automated detection and classification of high frequency oscillations (HFOs) in human intracereberal EEG. Biomedical Signal Processing and Control. 2013;**8**(6):927-34.
87 Dumpelmann M, Jacobs J, Kerber K, Schulze-Bonhage A. Automatic 80-250Hz "ripple" high frequency oscillation detection in invasive subdural grid and strip recordings in epilepsy by a radial basis function neural network. Clinical neurophysiology : official journal of the International Federation of Clinical Neurophysiology. 2012 Sep;**123**(9):1721-31.
88 Birot G, Kachenoura A, Albera L, Benar C, Wendling F. Automatic detection of fast ripples. Journal of neuroscience methods. 2013 Mar 15;**213**(2):236-49.
89 Pail M, Halamek J, Daniel P, et al. Intracerebrally recorded high frequency oscillations: simple visual assessment versus automated detection. Clinical neurophysiology : official journal of the International Federation of Clinical Neurophysiology. 2013 Oct;**124**(10):1935-42.
90 Crepon B, Navarro V, Hasboun D, et al. Mapping interictal oscillations greater than 200 Hz recorded with intracranial macroelectrodes in human epilepsy. Brain : a journal of neurology. 2010 Jan;**133**(Pt 1):33-45.
91 Burnos S, Hilfiker P, Surucu O, et al. Human intracranial high frequency oscillations (HFOs) detected by automatic time-frequency analysis. PloS one. 2014;**9**(4):e94381.

92 Liu S, Ince NF, Sabanci A, et al. Detection of High Frequency Oscillations in Epilepsy with K-means Clustering Method. I Ieee Embs C Neur E. 2015:934-7.
93 Charupanit K, Lopour BA. A Simple Statistical Method for the Automatic Detection of High Frequency Oscillations in Human Intracranial EEG. Brain topography. 2017 Nov;**30**(6):724-38.
94 Chen-Wei C, Chien C, Shang-Yeong K, Shun-Chi W. Multi-channel algorithms for epileptic high-frequency oscillation detection. Conference proceedings : Annual International Conference of the IEEE Engineering in Medicine and Biology Society IEEE Engineering in Medicine and Biology Society Conference. 2016 Aug;**2016**:948-51.
95 Ren S, Gliske SV, Brang D, Stacey WC. Redaction of false high frequency oscillations due to muscle artifact improves specificity to epileptic tissue. Clinical neurophysiology : official journal of the International Federation of Clinical Neurophysiology. 2019 Jun;**130**(6):976-85.
96 Amiri M, Lina JM, Pizzo F, Gotman J. High Frequency Oscillations and spikes: Separating real HFOs from false oscillations. Clinical neurophysiology : official journal of the International Federation of Clinical Neurophysiology. 2016 Jan;**127**(1):187-96.
97 Burnos S, Frauscher B, Zelmann R, Haegelen C, Sarnthein J, Gotman J. The morphology of high frequency oscillations (HFO) does not improve delineating the epileptogenic zone. Clinical neurophysiology : official journal of the International Federation of Clinical Neurophysiology. 2016 Apr;**127**(4):2140-8.
98 Fedele T, van 't Klooster M, Burnos S, et al. Automatic detection of high frequency oscillations during epilepsy surgery predicts seizure outcome. Clinical neurophysiology : official journal of the International Federation of Clinical Neurophysiology. 2016 Sep;**127**(9):3066-74.
99 Alvarado-Rojas C, Huberfeld G, Baulac M, et al. Different mechanisms of ripple-like oscillations in the human epileptic subiculum. Annals of neurology. 2015;**77**(2):281-90.
100 Valderrama M, Crépon B, Botella-Soler V, et al. Human Gamma Oscillations during Slow Wave Sleep. PloS one. 2012;**7**(4):e33477.
101 Axmacher N, Elger CE, Fell J. Ripples in the medial temporal lobe are relevant for human memory consolidation. Brain : a journal of neurology. 2008;**131**(7):1806-17.
102 Le Van Quyen M, Staba R, Bragin A, et al. Large-Scale Microelectrode Recordings of High-Frequency Gamma Oscillations in Human Cortex during Sleep. The Journal of Neuroscience. 2010;**30**(23):7770.
103 Wang S, Wang IZ, Bulacio JC, et al. Ripple classification helps to localize the seizure-onset zone in neocortical epilepsy. Epilepsia. 2013 Feb;**54**(2):370-6.

104 Cho JR, Joo EY, Koo DL, Hong SC, Hong SB. Clinical Utility of Interictal High-Frequency Oscillations Recorded with Subdural Macroelectrodes in Partial Epilepsy. J Clin Neurol. 2012;**8**(1):22-34.
105 Waldman ZJ, Shimamoto S, Song I, et al. A method for the topographical identification and quantification of high frequency oscillations in intracranial electroencephalography recordings. Clinical neurophysiology : official journal of the International Federation of Clinical Neurophysiology. 2018 Jan;**129**(1):308-18.
106 Jiang C, Li X, Yan J, et al. Determining the Quantitative Threshold of High-Frequency Oscillation Distribution to Delineate the Epileptogenic Zone by Automated Detection. Frontiers in neurology. 2018;**9**:889.
107 Wu M, Wan T, Wan X, Du Y, She J. Fast, Accurate Localization of Epileptic Seizure Onset Zones Based on Detection of High-Frequency Oscillations Using Improved Wavelet Transform and Matching Pursuit Methods. Neural Computation. 2017;**29**(1):194-219.
108 Pearce A, Wulsin D, Blanco JA, Krieger A, Litt B, Stacey WC. Temporal changes of neocortical high-frequency oscillations in epilepsy. J Neurophysiol. 2013 Sep;**110**(5):1167-79.
109 Blanco JA, Stead M, Krieger A, et al. Data mining neocortical high-frequency oscillations in epilepsy and controls. Brain : a journal of neurology. 2011 Oct;**134**(Pt 10):2948-59.
110 Liu S, Sha Z, Sencer A, et al. Exploring the time-frequency content of high frequency oscillations for automated identification of seizure onset zone in epilepsy. Journal of neural engineering. 2016 Apr;**13**(2):026026.
111 Zelmann R, Mari F, Jacobs J, Zijlmans M, Dubeau F, Gotman J. A comparison between detectors of high frequency oscillations. Clinical neurophysiology : official journal of the International Federation of Clinical Neurophysiology. 2012 Jan;**123**(1):106-16.
112 Fujiwara H, Greiner HM, Lee KH, et al. Resection of ictal high-frequency oscillations leads to favorable surgical outcome in pediatric epilepsy. Epilepsia. 2012 Sep;**53**(9):1607-17.
113 van 't Klooster MA, van Klink NEC, Zweiphenning W, et al. Tailoring epilepsy surgery with fast ripples in the intraoperative electrocorticogram. Annals of neurology. 2017 May;**81**(5):664-76.
114 Fedele T, Burnos S, Boran E, et al. Resection of high frequency oscillations predicts seizure outcome in the individual patient. Scientific reports. 2017 Oct 23;**7**(1):13836.
115 Dian JA, Colic S, Chinvarun Y, Carlen PL, Bardakjian BL. Identification of brain regions of interest for epilepsy surgery planning using support vector machines. 2015 37th Annual International Conference of the IEEE Engineering in Medicine and Biology Society (EMBC); 2015 25-29 Aug. 2015; 2015. p. 6590-3.

116 Sumsky SL, Santaniello S. Decision Support System for Seizure Onset Zone Localization Based on Channel Ranking and High-Frequency EEG Activity. IEEE Journal of Biomedical and Health Informatics. 2019;**23**(4):1535-45.
117 Holler Y, Kutil R, Klaffenbock L, et al. High-frequency oscillations in epilepsy and surgical outcome. A meta-analysis. Frontiers in human neuroscience. 2015;**9**:574.
118 Fujiwara H, Leach JL, Greiner HM, et al. Resection of ictal high frequency oscillations is associated with favorable surgical outcome in pediatric drug resistant epilepsy secondary to tuberous sclerosis complex. Epilepsy research. 2016 Oct;**126**:90-7.
119 Sun Y-P, Wang Y-P, Wang Z-H, et al. High-frequency Oscillations and the Seizure Onset Zones in Neocortical Epilepsy. Chin Med J (Engl). 2015;**128**(13):1724-7.
120 Cuello-Oderiz C, von Ellenrieder N, Sankhe R, et al. Value of ictal and interictal epileptiform discharges and high frequency oscillations for delineating the epileptogenic zone in patients with focal cortical dysplasia. Clinical Neurophysiology. 2018 2018/06/01/;**129**(6):1311-9.
121 Roehri N, Pizzo F, Lagarde S, et al. High-frequency oscillations are not better biomarkers of epileptogenic tissues than spikes. Annals of neurology. 2018 Jan;**83**(1):84-97.
122 Zanow F, Knösche TR. ASA-Advanced Source Analysis of Continuous and Event-Related EEG/MEG Signals. Brain topography. 2004 2004/06/01;**16**(4):287-90.
123 Fedele T, Ramantani G, Burnos S, et al. Prediction of seizure outcome improved by fast ripples detected in low-noise intraoperative corticogram. Clinical Neurophysiology. 2017 2017/07/01/;**128**(7):1220-6.
124 Liu S, Quach MM, Curry DJ, Ummat M, Seto E, Ince NF. High-frequency oscillations detected in ECoG recordings correlate with cavernous malformation and seizure-free outcome in a child with focal epilepsy: A case report. Epilepsia Open. 2017;**2**(2):267-72.
125 von Ellenrieder N, Frauscher B, Dubeau F, Gotman J. Interaction with slow waves during sleep improves discrimination of physiologic and pathologic high-frequency oscillations (80-500 Hz). Epilepsia. 2016 Jun;**57**(6):869-78.
126 Youden W. Index for rating diagnostic tests. Cancer. 1950;**3**(1):32-5.
127 Fedele T, Ramantani G, Sarnthein J. High frequency oscillations as markers of epileptogenic tissue – End of the party? Clinical Neurophysiology. 2019;**130**(5):624-6.
128 Charupanit K, Sen-Gupta I, Lin JJ, Lopour BA. Detection of anomalous high frequency events in human intracranial EEG. bioRxiv. 2019;**782912**.
129 Frauscher B, von Ellenrieder N, Zelmann R, et al. High-Frequency Oscillations in the Normal Human Brain. Annals of neurology. 2018 Sep;**84**(3):374-85.
130 Mooij AH, Frauscher B, Gotman J, Huiskamp GJM. A skew-based method for identifying intracranial EEG channels with epileptic activity without detecting spikes,

ripples, or fast ripples. Clinical neurophysiology : official journal of the International Federation of Clinical Neurophysiology. 2020 Jan;**131**(1):183-92.
131 Motoi H, Jeong J-W, Juhász C, et al. Quantitative analysis of intracranial electrocorticography signals using the concept of statistical parametric mapping. Scientific reports. 2019 2019/11/22;**9**(1):17385.
132 Guirgis M, Chinvarun Y, Del Campo M, Carlen PL, Bardakjian BL. Defining regions of interest using cross-frequency coupling in extratemporal lobe epilepsy patients. Journal of neural engineering. 2015 Mar 13;**12**(2):026011.
133 Weiss SA, Banks GP, McKhann GM, Jr., et al. Ictal high frequency oscillations distinguish two types of seizure territories in humans. Brain : a journal of neurology. 2013 Dec;**136**(Pt 12):3796-808.
134 Ibrahim GM, Wong SM, Anderson RA, et al. Dynamic modulation of epileptic high frequency oscillations by the phase of slower cortical rhythms. Experimental neurology. 2014 Jan;**251**:30-8.
135 Zweiphenning WJEM, Keijzer HM, van Diessen E, et al. Increased gamma and decreased fast ripple connections of epileptic tissue: A high-frequency directed network approach. Epilepsia. 2019;**60**(9):1908-20.
136 Zweiphenning WJEM, van 't Klooster MA, van Diessen E, et al. High frequency oscillations and high frequency functional network characteristics in the intraoperative electrocorticogram in epilepsy. NeuroImage: Clinical. 2016 2016/02/01/;**12**:928-39.
137 González Otárula KA, von Ellenrieder N, Cuello-Oderiz C, Dubeau F, Gotman J. High-Frequency Oscillation Networks and Surgical Outcome in Adult Focal Epilepsy. Annals of neurology. 2019;**85**(4):485-94.
138 Malinowska U, Bergey GK, Harezlak J, Jouny CC. Identification of seizure onset zone and preictal state based on characteristics of high frequency oscillations. Clinical neurophysiology : official journal of the International Federation of Clinical Neurophysiology. 2015 Aug;**126**(8):1505-13.
139 Behrens E, Zentner J, van Roost D, Hufnagel A, Elger CE, Schramm J. Subdural and depth electrodes in the presurgical evaluation of epilepsy. Acta Neurochirurgica. 1994 1994/03/01;**128**(1):84-7.
140 Little S, Brown P. What brain signals are suitable for feedback control of deep brain stimulation in Parkinson's disease? Ann N Y Acad Sci. 2012 2012/08//;**1265**:9-24.
141 Schwartz AB. CORTICAL NEURAL PROSTHETICS. Annual Review of Neuroscience. 2004 2004/07/21;**27**(1):487-507.
142 Shih JJ, Krusienski DJ, Wolpaw JR. Brain-Computer Interfaces in Medicine. Mayo Clinic Proceedings. 2012 2012/03/01/;**87**(3):268-79.

143 Ollikainen JO, Vauhkonen M, Karjalainen PA, Kaipio JP. Effects of electrode properties on EEG measurements and a related inverse problem. Medical Engineering & Physics. 2000 2000/10/01/;**22**(8):535-45.
144 Nelson MJ, Pouget P. Do electrode properties create a problem in interpreting local field potential recordings? J Neurophysiol. 2010 May;**103**(5):2315-7.
145 Nunez PL, Srinivasan R. Electric Fields of the Brain: The Neurophysics of EEG: Oxford University Press; 2006.
146 Rose JD, Weishaar DJ. Tapered tungsten fine-wire microelectrode for chronic single unit recording. Brain Research Bulletin. 1979 1979/05/01/;**4**(3):435-7.
147 Chari A, Thornton RC, Tisdall MM, Scott RC. Microelectrode recordings in human epilepsy: a case for clinical translation. Brain communications. 2020;**2**(2):fcaa082.
148 Shokoueinejad M, Park D-W, Jung YH, et al. Progress in the Field of Micro-Electrocorticography. Micromachines (Basel). 2019;**10**(1):62.
149 Nelson MJ, Pouget P. Physical model of coherent potentials measured with different electrode recording site sizes. Journal of Neurophysiology. 2012;**107**(5):1291-300.
150 Moffitt MA, McIntyre CC. Model-based analysis of cortical recording with silicon microelectrodes. Clinical Neurophysiology. 2005 2005/09/01/;**116**(9):2240-50.
151 Suihko V, Eskola H, Malmivuo J. Effect of electrode size in electroencephalography and electrical transcranial stimulation. Proc 1st Int Conf Medical Physics and Biomedical Engineering; 1994; 1994. p. 306-10.
152 Lempka SF, Johnson MD, Moffitt MA, Otto KJ, Kipke DR, McIntyre CC. Theoretical analysis of intracortical microelectrode recordings. Journal of neural engineering. 2011 2011/07/20;**8**(4):045006.
153 Neto JP, Baião P, Lopes G, et al. Does Impedance Matter When Recording Spikes With Polytrodes? Frontiers in Neuroscience. 2018 2018-October-08;**12**(715).
154 Andersen RA, Hwang EJ, Mulliken GH. Cognitive Neural Prosthetics. Annual Review of Psychology. 2009 2010/01/01;**61**(1):169-90.
155 Ward MP, Rajdev P, Ellison C, Irazoqui PP. Toward a comparison of microelectrodes for acute and chronic recordings. Brain Research. 2009;**1282**:183-200.
156 Viswam V, Obien MEJ, Franke F, Frey U, Hierlemann A. Optimal Electrode Size for Multi-Scale Extracellular-Potential Recording From Neuronal Assemblies. Frontiers in Neuroscience. 2019 2019-April-26;**13**(385).
157 Wang W, Degenhart AD, Collinger JL, et al. Human motor cortical activity recorded with Micro-ECoG electrodes, during individual finger movements. 2009 Annual International Conference of the IEEE Engineering in Medicine and Biology Society; 2009 3-6 Sept. 2009; 2009. p. 586-9.

158 Kellis S, Sorensen L, Darvas F, et al. Multi-scale analysis of neural activity in humans: Implications for micro-scale electrocorticography. Clinical Neurophysiology. 2016 2016/01/01/;**127**(1):591-601.
159 Hermiz J, Rogers N, Kaestner E, et al. Sub-millimeter ECoG pitch in human enables higher fidelity cognitive neural state estimation. NeuroImage. 2018 2018/08/01/;**176**:454-64.
160 Wang PT, King CE, McCrimmon CM, et al. Comparison of decoding resolution of standard and high-density electrocorticogram electrodes. Journal of neural engineering. 2016;**13**(2):026016-.
161 Boran E, Ramantani G, Krayenbuhl N, et al. High-density ECoG improves the detection of high frequency oscillations that predict seizure outcome. Clinical neurophysiology : official journal of the International Federation of Clinical Neurophysiology. 2019 Oct;**130**(10):1882-8.
162 Schevon CA, Ng SK, Cappell J, et al. Microphysiology of Epileptiform Activity in Human Neocortex. Journal of Clinical Neurophysiology. 2008;**25**(6).
163 Schevon CA, Goodman RR, McKhann G, Jr., Emerson RG. Propagation of Epileptiform Activity on a Submillimeter Scale. Journal of Clinical Neurophysiology. 2010;**27**(6).
164 Robinson DA. The electrical properties of metal microelectrodes. Proceedings of the IEEE. 1968;**56**(6).
165 Nelson MJ, Pouget P, Nilsen EA, Patten CD, Schall JD. Review of signal distortion through metal microelectrode recording circuits and filters. Journal of neuroscience methods. 2008 Mar 30;**169**(1):141-57.
166 Pomfret R, Miranpuri G, Sillay K. The substitute brain and the potential of the gel model. Annals of neurosciences. 2013;**20**(3):118.
167 Latikka J, Kuurne T, Eskola H. Conductivity of living intracranial tissues. Physics in Medicine and Biology. 2001 2001/05/02;**46**(6):1611-6.
168 Ombao HC, Raz JA, Strawderman RL, von Sachs R. A Simple Generalised Crossvalidation Method of Span Selection for Periodogram Smoothing. Biometrika. 2001;**88**(4):1186-92.
169 Ngo D, Ombao H, Sun Y, et al. An exploratory data analysis of electroencephalograms using the functional boxplots approach. Frontiers in Neuroscience. 2015;**9**:282.
170 López-Pintado S, Romo J. On the Concept of Depth for Functional Data. Journal of the American Statistical Association. 2009 2009/06/01;**104**(486):718-34.
171 Joffre Olaya MD, Maija-Riikka Steenari, M.D., William Loudon, M.D., Ph.D., Michael Muhonen, M.D., Daniel Shrey, M.D. Abstract of "Use of High-Density Subdural Grid to Increase Precision of Functional Mapping and Seizure Onset Zone Localization",

43rd Annual Meeting of the The American Society of Pediatric Neurosurgeons. Journal of Neurosurgery: Pediatrics. 2020 01 Mar. 2020;**25**(3):1-60.
172 Castagnola E, Maiolo L, Maggiolini E, et al. PEDOT-CNT-Coated Low-Impedance, Ultra-Flexible, and Brain-Conformable Micro-ECoG Arrays. IEEE Transactions on Neural Systems and Rehabilitation Engineering. 2015;**23**(3):342-50.
173 Shen I, Walkosz M, Besio W. Tripolar concentric ring electrode electroencephalography using Signa gel for impedance matching. 2014 40th Annual Northeast Bioengineering Conference (NEBEC); 2014 25-27 April 2014; 2014. p. 1-2.
174 Vorwerk J, Engwer C, Pursiainen S, Wolters CH. A Mixed Finite Element Method to Solve the EEG Forward Problem. IEEE Transactions on Medical Imaging. 2017;**36**(4):930-41.
175 Lachaux JP, Axmacher N, Mormann F, Halgren E, Crone NE. High-frequency neural activity and human cognition: past, present and possible future of intracranial EEG research. Progress in neurobiology. 2012 Sep;**98**(3):279-301.
176 Jirsch JD, Urrestarazu E, LeVan P, Olivier A, Dubeau F, Gotman J. High-frequency oscillations during human focal seizures. Brain : a journal of neurology. 2006;**129**(6):1593-608.
177 Zelmann R, Lina JM, Schulze-Bonhage A, Gotman J, Jacobs J. Scalp EEG is not a blur: it can see high frequency oscillations although their generators are small. Brain topography. 2014 Sep;**27**(5):683-704.
178 Modur PN, Zhang S, Vitaz TW. Ictal high-frequency oscillations in neocortical epilepsy: implications for seizure localization and surgical resection. Epilepsia. 2011 Oct;**52**(10):1792-801.
179 Bragin A, Mody I, Wilson CL, Engel J, Jr. Local generation of fast ripples in epileptic brain. The Journal of neuroscience : the official journal of the Society for Neuroscience. 2002 Mar 1;**22**(5):2012-21.
180 Kucewicz MT, Cimbalnik J, Matsumoto JY, et al. High frequency oscillations are associated with cognitive processing in human recognition memory. Brain : a journal of neurology. 2014 Aug;**137**(Pt 8):2231-44.
181 Zhang H, Fell J, Axmacher N. Electrophysiological mechanisms of human memory consolidation. Nature communications. 2018 2018/10/05;**9**(1):4103.
182 von Ellenrieder N, Dubeau F, Gotman J, Frauscher B. Physiological and pathological high-frequency oscillations have distinct sleep-homeostatic properties. NeuroImage Clinical. 2017;**14**:566-73.
183 Nagasawa T, Juhasz C, Rothermel R, Hoechstetter K, Sood S, Asano E. Spontaneous and visually driven high-frequency oscillations in the occipital cortex: intracranial recording in epileptic patients. Human brain mapping. 2012 Mar;**33**(3):569-83.

184 Wang S, So NK, Jin B, et al. Interictal ripples nested in epileptiform discharge help to identify the epileptogenic zone in neocortical epilepsy. Clinical neurophysiology : official journal of the International Federation of Clinical Neurophysiology. 2017 Jun;**128**(6):945-51.
185 Smith MM, Weaver KE, Grabowski TJ, Rao RPN, Darvas F. Non-invasive detection of high gamma band activity during motor imagery. Frontiers in human neuroscience. 2014;**8**.
186 McCrimmon CM, Wang PT, Heydari P, et al. Electrocorticographic Encoding of Human Gait in the Leg Primary Motor Cortex. Cerebral Cortex. 2018;**28**(8):2752-62.
187 Bruder JC, Dumpelmann M, Piza DL, Mader M, Schulze-Bonhage A, Jacobs-Le Van J. Physiological Ripples Associated with Sleep Spindles Differ in Waveform Morphology from Epileptic Ripples. International journal of neural systems. 2017 Nov;**27**(7):1750011.
188 Mooij AH, Huiskamp GJM, Aarts E, Ferrier CH, Braun KPJ, Zijlmans M. Accurate differentiation between physiological and pathological ripples recorded with scalp-EEG. Clinical Neurophysiology. 2022 2022/08/30/.
189 Plante DT, Goldstein MR, Cook JD, et al. Effects of partial sleep deprivation on slow waves during non-rapid eye movement sleep: A high density EEG investigation. Clinical Neurophysiology. 2016 2016/02/01/;**127**(2):1436-44.
190 Bernardo D, Nariai H, Hussain SA, Sankar R, Wu JY. Interictal scalp fast ripple occurrence and high frequency oscillation slow wave coupling in epileptic spasms. Clinical neurophysiology : official journal of the International Federation of Clinical Neurophysiology. 2020 Jul;**131**(7):1433-43.
191 McCrimmon CM, Riba A, Garner C, Maser AL, Shrey DW, Lopour BA. Automated detection of ripple oscillations in long-term scalp EEG from patients with infantile spasms. BioRxiv. 2020(doi.org/10.1101/2020.06.03.132183).
192 Charupanit K, Nunez MD, Bernardo D, et al. Automated Detection of High Frequency Oscillations in Human Scalp Electroencephalogram. Conference proceedings : Annual International Conference of the IEEE Engineering in Medicine and Biology Society IEEE Engineering in Medicine and Biology Society Conference; 2018; 2018. p. 3116-9.
193 Noorlag L, van Klink NEC, Kobayashi K, Gotman J, Braun KPJ, Zijlmans M. High-frequency oscillations in scalp EEG: A systematic review of methodological choices and clinical findings. Clinical Neurophysiology. 2022 2022/05/01/;**137**:46-58.
194 Andrade-Valenca L, Dubeau F, Mari F, Zelmann R, Gotman J. Interictal scalp fast oscillations as a marker of the seizure onset zone. Neurology. 2011;**77**:524-31.
195 Scammell TE, Arrigoni E, Lipton JO. Neural Circuitry of Wakefulness and Sleep. Neuron. 2017 2017/02/22/;**93**(4):747-65.

196 Liu J, Ramakrishnan S, Laxminarayan S, et al. Effects of signal artefacts on electroencephalography spectral power during sleep: quantifying the effectiveness of automated artefact-rejection algorithms. Journal of Sleep Research. 2018 2018/02/01;**27**(1):98-102.
197 Brunner D, Vasko R, Detka C, Monahan J, Reynolds Iii C, Kupfer D. Muscle artifacts in the sleep EEG: Automated detection and effect on all-night EEG power spectra. Journal of Sleep Research. 1996 1996/09/01;**5**(3):155-64.
198 Tan X, Campbell IG, Feinberg I. A simple method for computer quantification of stage REM eye movement potentials. Psychophysiology. 2001 2001/05/01;**38**(3):512-6.
199 Bagshaw AP, Jacobs J, LeVan P, Dubeau F, Gotman J. Effect of sleep stage on interictal high-frequency oscillations recorded from depth macroelectrodes in patients with focal epilepsy. Epilepsia. 2009;**50**(4):617-28.
200 Sakuraba R, Iwasaki M, Okumura E, et al. High frequency oscillations are less frequent but more specific to epileptogenicity during rapid eye movement sleep. Clinical neurophysiology : official journal of the International Federation of Clinical Neurophysiology. 2016 Jan;**127**(1):179-86.
201 Staba RJ, Wilson CL, Bragin A, Jhung D, Fried I, Engel Jr J. High-frequency oscillations recorded in human medial temporal lobe during sleep. Annals of neurology. 2004 2004/07/01;**56**(1):108-15.
202 Frauscher B, von Ellenrieder N, Dubeau F, Gotman J. EEG desynchronization during phasic REM sleep suppresses interictal epileptic activity in humans. Epilepsia. 2016;**57**(6):879-88.
203 McKenna JT, Zielinski MR, McCarley RW. Neurobiology of REM Sleep, NREM Sleep Homeostasis, and Gamma Band Oscillations. In: Chokroverty S, editor. Sleep Disorders Medicine: Basic Science, Technical Considerations and Clinical Aspects. New York, NY: Springer New York; 2017. p. 55-77.
204 Abe T, Matsuoka T, Ogawa K, Nittono H, Hori T. Gamma band EEG activity is enhanced after the occurrence of rapid eye movement during human REM sleep. Sleep and Biological Rhythms. 2008 2008/01/01;**6**(1):26-33.
205 Gross DW, Gotman J. Correlation of high-frequency oscillations with the sleep–wake cycle and cognitive activity in humans. Neuroscience. 1999 1999/11/01/;**94**(4):1005-18.
206 Yamada T, Kameyama S, Fuchigami Y, Nakazumi Y, Dickins QS, Kimura J. Changes of short latency somatosensory evoked potential in sleep. Electroencephalography and clinical neurophysiology. 1988 1988/08/01/;**70**(2):126-36.
207 Maingret N, Girardeau G, Todorova R, Goutierre M, Zugaro M. Hippocampo-cortical coupling mediates memory consolidation during sleep. Nat Neurosci. 2016 2016/07/01;**19**(7):959-64.

208 Mednick SC, McDevitt EA, Walsh JK, et al. The Critical Role of Sleep Spindles in Hippocampal-Dependent Memory: A Pharmacology Study. The Journal of Neuroscience. 2013;**33**(10):4494.
209 Jiang X, Gonzalez-Martinez J, Halgren E. Posterior Hippocampal Spindle Ripples Co-occur with Neocortical Theta Bursts and Downstates-Upstates, and Phase-Lock with Parietal Spindles during NREM Sleep in Humans. The Journal of Neuroscience. 2019;**39**(45):8949.
210 Latchoumane C-FV, Ngo H-VV, Born J, Shin H-S. Thalamic Spindles Promote Memory Formation during Sleep through Triple Phase-Locking of Cortical, Thalamic, and Hippocampal Rhythms. Neuron. 2017 2017/07/19/;**95**(2):424-35.e6.
211 Dickey CW, Verzhbinsky IA, Jiang X, et al. Cortical Ripples during NREM Sleep and Waking in Humans. The Journal of Neuroscience. 2022;**42**(42):7931-46.
212 Zweiphenning WJEM, von Ellenrieder N, Dubeau F, et al. Correcting for physiological ripples improves epileptic focus identification and outcome prediction. Epilepsia. 2022 2022/02/01;**63**(2):483-96.
213 Kerber K, Dumpelmann M, Schelter B, et al. Differentiation of specific ripple patterns helps to identify epileptogenic areas for surgical procedures. Clinical neurophysiology : official journal of the International Federation of Clinical Neurophysiology. 2014 Jul;**125**(7):1339-45.